UC Berkeley
UC Berkeley Electronic Theses and Dissertations

Title

Electrochemistry of $FeSO_4$-$Na_2S_2O_3$ and $CuSO_4$-$Na_2S_2O_3$ Systems for Template-Assisted Nanowire Synthesis

Permalink

https://escholarship.org/uc/item/808386sn

Author

Brogan, Lee Jeffery

Publication Date

2011

Peer reviewed|Thesis/dissertation

Electrochemistry of $FeSO_4$–$Na_2S_2O_3$ and $CuSO_4$–$Na_2S_2O_3$ Systems for Template-Assisted Nanowire Synthesis

by

Lee Jeffery Brogan

A dissertation submitted in partial satisfaction of the

requirements for the degree of

Doctor of Philosophy

in

Chemistry

in the

GRADUATE DIVISION

of the

UNIVERSITY OF CALIFORNIA, BERKELEY

Committee in charge:
Professor Angelica Stacy, Chair
Professor Marcin Majda
Professor Fiona Doyle

Fall 2011

Electrochemistry of $FeSO_4$–$Na_2S_2O_3$ and $CuSO_4$–$Na_2S_2O_3$ Systems for Template-Assisted Nanowire Synthesis

Copyright 2011

by

Lee Jeffery Brogan

Abstract

Electrochemistry of $FeSO_4$–$Na_2S_2O_3$ and $CuSO_4$–$Na_2S_2O_3$ Systems for Template-Assisted Nanowire Synthesis

by

Lee Jeffery Brogan

Doctor of Philosophy in Chemistry

University of California, Berkeley

Professor Angelica Stacy, Chair

Two related series of investigations are presented in this dissertation. First, two candidate systems for electrochemical deposition of metal sulfides for photovoltaic applications have been characterized. Secondly, a general electrochemical synthesis method allowing countable numbers of wires embedded in porous anodic alumina arrays to be measured using macroscopic contacts was developed.

Electrochemical studies of the $FeSO_4$–$Na_2S_2O_3$ system and the $CuSO_4$–$Na_2S_2O_3$ system were undertaken to evaluate their suitability as electrodeposition baths for FeS_2 and Cu_xS, respectively. Each solution system was studied extensively using cyclic voltammetry to characterize electrochemical processes at various concentrations. The iron sulfide / thiosulfate system was found to be unsuitable for the synthesis of FeS_2 due to the preferential formation of FeS. The copper sulfide / thiosulfate system was found to be suitable for the synthesis of Cu_2S, with thiosulfate concentration being the most important parameter due to the high complexation of Cu(I) by thiosulfate.

Investigations into the electrochemical synthesis of metal wires in porous anodic alumina templates revealed an interesting synthesis mechanism wherein sparse, isolated wires are created in a very small fraction of the available pores. These wires are nucleated through the reduction of metal from the deposition bath by aluminum at the base of the alumina pores. This reduction causes a localized increase in acidity, accelerating the dissolution of the alumina barrier layer and allowing more typical wire deposition to occur. The sparse nucleation is exaggerated by the increasing rate of wire deposition as the wires lengthen and the swift rate of overgrowth formation at the surface of the template, resulting in domes of overgrowth attached to countable numbers of nanowires. This geometry has been exploited

to obtain *in situ* measurements of known numbers of nanowires.

For Kestrel.

Contents

List of Figures

List of Tables

Acknowledgments

Chapter 1

Introduction

The course of civilization has been carved with metal. We have named the ages of our cultures after the metals and alloys which defined them. Civilizations have formed or fallen based on their ability to draw metal from the earth and work it into useful tools. The great buildings of our modern world are quite literally built upon admixtures of iron. Electricity, the lifeblood of modern society, flows through veins of aluminum and is pumped by a copper-coiled heart. It is no wonder that generations of people have sought to further humanity's knowledge of metal extraction, working, and manipulation, for as humans we are defined by the tools we use.

Iron and copper have historically been two of the most economically and technologically important metals. It is no accident that the Bronze and Iron Ages were defined as such. While most iron and copper extraction occurs through smelting of high-grade ores [7], extraction from lower grade sulfide ores through heap leaching and bioleaching and recovery of usable material from mine run-off are becoming increasingly more important as more easily processed ores are depleted [9, 10]. This is an especially important process for copper as its terrestrial abundance is three orders of magnitude lower than that of iron [11] and copper sulfides have a greater economic importance [7]. Additionally, copper and iron sulfides are often found in association with one another, forming multi-metal compounds such as the most important copper ore, chalcopyrite ($CuFeS_2$). Thus, understanding the fundamental electrochemistry involved in the leaching of these materials is an important endeavor.

In addition to providing an understanding of leaching processes, the electrochemistry of copper sulfide and iron sulfide systems is interesting for the reverse reaction, that of electrochemical synthesis. Pyrite (FeS_2) is a semiconductor with a bandgap of 0.95 eV [12]. It has historically been used as a receiver for crystal radios [13] and has more recently received attention as a potential battery cathode [14] and for inexpensive and environmentally friendly photovoltaic modules [15, 16]. Of particular note is the high absorption coefficient of pyrite, allowing much thinner cells. Cu_2S was investigated extensively in the 1980's as a photovoltaic material coupled with CdS, and thin film solar cells with efficiencies approaching 10% were created [17]. Cu_2S is recently receiving renewed interest for this purpose [18], for it too is a

low-cost material with good theoretical photovoltaic potential. The primary purpose of this work is to subject systems of iron-thiosulfate and copper-thiosulfate to an electrochemical analysis to evaluate their suitability as baths for the electrodeposition of semiconductors of interest in photovoltaic energy conversion.

Electrodeposition offers a low-cost synthetic route toward a number of device structures which would increase the efficiency of devices created from materials of lower quality and substantially lower cost than those currently used. A basic understanding of the physics and economics behind the current production of photovoltaics is needed to follow the motivation for these device structures.

1.1   A Brief History of Photovoltaics

Since the earliest days of mankind, the sun has been revered as the bringer of warmth, the dispeller of darkness, and the giver of life. The ancient Greeks had their Apollo, the Egyptians their Amon-Ra, the Aztecs their Tonatiuh, all anthropomorphizations of the generative solar body. It is fitting, after millennia of humanity wresting our energy with flame from biomass and the thick black blood of the earth, that we are once more turning to the sun to warm our bodies, light our homes, and breathe life into the electrons which move our modern world.

The photovoltaic effect was first described by Alexandre-Edmond Becquerel in 1839, who observed light-influenced reactions on thin sheets of platinum, brass, and silver immersed in electrolytic fluids [19]. The first large area solar cell is credited to Charles Fritts who in 1883 described a cell he fabricated from a sheet of selenium with thin gold contacts [20]. The modern solar cell, which separates charges across a p-n junction, was patented in 1946 by Russell Ohl [21].

Photovoltaics (PV) were originally confined to niche applications due to their high cost relative to more traditional fossil fuel sources of energy. The first place photovoltaics achieved truly widespread application was space, where cost is not considered a limiting factor, regular fuel transfers are not practical, and the notion of grid connection for power is patently ridiculous. As costs went down and efficiency increased, more niche uses for photovoltaics opened up. They became used regularly to provide power in locations where remoteness precluded grid connection and constant fuel transfers for traditional fossil fuel generators were deemed too expensive or unreliable. They were also used in certain low-draw applications in lieu of batteries; the now-ubiquitous solar-powered four-function calculator comes readily to mind [22].

More recently, the significant political, economic, strategic, and environmental pressures toward the production of electricity without dependence on fossil fuels has spurred rapid developments in the field of photovoltaics. Optimization of silicon-based junction cells through texturing, anti-reflective coating, and clever construction have allowed them to reach effi-

ciencies of above 20% in laboratory tests [23], and commercial installations now often see efficiencies of above 15% [24]. Multi-junction cells, engineered to more efficiently harvest a broader range of the solar spectrum, have been created with efficiencies of around 40% [24].

Starting around the first World Oil Embargo in 1973, photovoltaics began to touch the popular consciousness with dreams of a world powered by free energy sleeting down like manna from the heavens. As awareness of PV has grown, so too has its popularity, aided by significant government investments in the field for reasons of conservation and natural security. Thanks to these factors, the amount of power generated by PV installations worldwide was increasing at rates of around 40% per year according to data collected in 2007 [25]. As of 2008, the global installed PV generation capacity was 13.9 GW, 1.1 GW of which was in the United States [24]. This accounted for around a tenth of a percent of the electricity produced in 2008 [26].

1.2 Photovoltaic Cost Factors

While grid balancing problems and land usage are concerns for the future [27], it is the high cost of photovoltaics that is currently the major factor preventing their widespread adoption. Energy costs are usually expressed as money per kWh produced over the lifetime of the device in order to normalize for the fact that some energy sources (such as photovoltaics) have high initial investments but low operating costs. The cost of the photovoltaic module itself represents between 20% and 45% of the total lifetime material costs of a photovoltaic installation, with the remainder paying for an inverter, the required electronics and mounting equipment, and batteries, which are needed for stand-alone installations but not necessary for grid-connected or hybrid units [22]. The practical and manufacturing expertise needed to produce the inverters, electronics and armature for PV has been practiced in industry for decades, and the prime cost reducer in these cases is likely to be economies of scale once PV becomes more widely adopted. The creation of lower-cost modules, however, will require further fundamental research.

There are a number of factors influencing the cost per watt generated by the photovoltaic modules themselves. These include the rarity of the starting materials, their cost of extraction, their further cost of refinement, the difficulty and complexity of module construction, the efficiency of the completed module, and the resilience or lifetime of the module. This means that while increasing efficiency is of course a very important factor in the reduction of PV energy costs, it is necessary to consider the materials used and their ease of manufacture as well in order to produce an economically viable photovoltaic system.

Silicon based solar cells are the most commonly used modules on the market today. Si is the second most common element in the Earth's crust; natural abundance will not be a limiting factor for Si solar cells. However, the vast majority of the Si in the Earth's mantle is in form of silicates such as $(Mg,Fe)_2SiO_4$ [7]. Processing and purifying Si metal to the extent necessary for PV modules is an extremely energy intensive process. Additionally, due to the

relatively low absorption coefficient of Si, these modules require comparatively thicker areas of active material relative to alternative cell types [22]. The result is that even in very large systems in which parasitic losses can be greatly reduced, Si based solar cells require 1.5 to 3 years of operation before recouping the energy used in their manufacture [28]. This poses significant short- to medium-term energy use, CO_2 emission, and fossil fuel consumption problems should the production of solar modules be greatly accelerated.

Thin film cells are the major competitors of silicon-based PV. The market share of non-silicon cells is small (less than 6% of worldwide PV in 2007), but is growing quickly, especially in the United States [29]. The thin film cells currently on the market are based on CdTe junctions or Copper-Indium-Gallium-Selenide (CIGS) architectures. They require less processing and less involved mounting systems than silicon based cells, which makes them the lowest cost option per watt despite their somewhat lower efficiencies. The primary disadvantage to such thin-film cells is their reliance on toxic elements such as cadmium and elements with a low crustal abundance such as tellurium and indium. While current costs of production are low, increased demand may exceed the economically recoverable reserves of these elements.

An insightful analysis on the rarity and extraction cost of many PV candidate materials was recently performed by Wadia *et al.* [16]. This study calculated the theoretical minimum cost per watt of electricity generated by examining hypothetical cells exhibiting the theoretical maximum power conversion efficiency for the appropriate band gap and using a thickness of the material in question sufficient to absorb 85% of incident solar radiation. The costs of mining each of the constituent elements were then used to estimate the final costs per watt. In this analysis, the clear winners are amorphous Si, copper oxides, Zn_3P_2, and semiconducting sulfides of metals abundant in Earth's crust, including FeS_2, Cu_2S, NiS, and PbS. NiS and PbS are noted for having low maximum theoretical efficiencies, which will likely make them non-viable due to increasing balance-of-system costs.

This analysis pleads for realization. The key linker between the theoretical calculations and the production of practical photovoltaic modules is the synthesis of high quality modules that approach the theoretical limits in a cost-effective manner. Oftentimes these two features are extremely at odds – synthetic methods resulting in pure, crystalline substances typically require high energy inputs in the form of annealing steps, vacuum chambers, and high-purity precursors. One way to partially compensate for low-quality materials in a device is by tailoring the device structure to the materials involved. This tailoring requires an understanding of the device physics.

1.3 Overview of Practical Photovoltaic Physics

This section is by no means a comprehensive study of the working of PV devices. It is hoped that it is an introduction sufficient for a reader familiar with chemistry to understand the motivations behind the proposed PV device structures and materials choices. Readers interested in a more detailed treatment are referred to the references, especially the *Handbook*
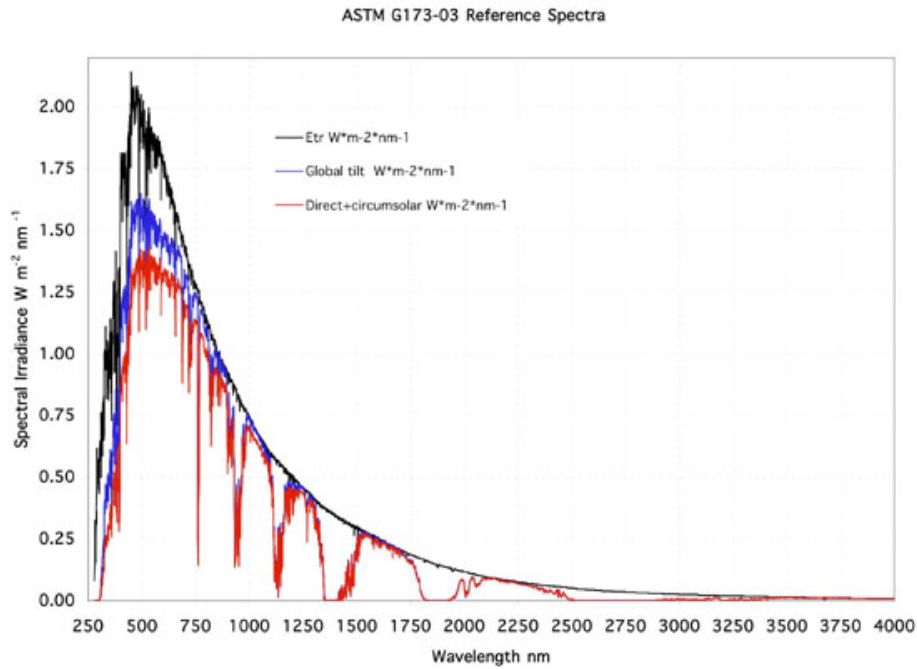
Figure 1.1: The standard solar spectral irradiance as a function of wavelength. Red indicates incident irradiance at the surface at Air Mass 1.5, accounting for atmospheric absorption [1].

of Photovoltaic Science and Engineering [22].

There are two key processes at work in photovoltaic devices. The first is the absorption of photon energy by an electron, promoting the electron to a higher energy state within the semiconductor, leaving an empty energy state or hole behind. The second process is the separation of the electron and hole so that the driving force behind the relaxation can be used to power a load rather than simply being dissipated as heat. This description of these processes is deceptively simple, and their optimization requires the manipulation of many, often coupled, variables.

1.3.1 Photon Absorption

When considering the absorption of photons for photovoltaic applications, it is of course necessary to reference the solar spectrum. Figure 1.1 displays the standard reference spectrum obtained by the American Society for Testing and Materials and published by the National Renewable Energy Laboratory [1]. The highest irradiance can be observed in the visible region, between about 390 nm and 750 nm – it is indeed for this reason that most terrestrial organisms evolved to be most sensitive to these wavelengths of light.

The massive variety of opaque materials extant demonstrates how readily matter interacts

with the energy in visible light. However, most interaction mechanisms do not take in this energy in a manner which allows it to be harnessed directly. While visible light has enough energy to induce electronic transitions, many opaque substances simply reflect light, a process in which the electromagnetic field of incident light drives the valence electrons of a material, resulting in a pattern of wave interference which also creates the phenomenon of refraction in media of different refractive indexes. Even if the light is actually absorbed to promote an electron to a new energy level, unless there is some mechanism in place to stop it the promoted electron can quickly relax to its ground state, either re-emitting the energy in a radiative transition or transferring it to vibrational energy (essentially, heat) in a non-radiative transition.

If incident photon energy is to be absorbed, there must be an available state into which the electron absorbing the energy can be promoted. If the energy of the photon is greater than the energy of the transition, the first law of thermodynamics requires that the excess energy be dissipated through some mechanism. If the energy of the photon is less than the energy of the transition, the only way to attain the transition is through the coupling of another source of energy, such as thermal lattice vibrations. For the purposes of generating photovoltaic potential, an ideal absorption event uses all of the incident photon energy to promote the absorbing electron so that all of the incident energy is available for recovery.

1.3.2 Charge Separation

In a typical photovoltaic cell, a p-n junction is used to separate the electron from its hole. Figure 1.2 displays a diagram depicting the process of energy absorption and charge separation at a p-n junction. The diagram depicts a spatial position orthogonal to the p-n junction on the x axis and the energy of an electron in the field generated by the atomic components of the semiconductors on the y axis. In a solid, the discrete electronic states of single atoms begin to give way to continuums of allowed states. These continuums are known as bands. As long as a particular band is not completely filled, it is possible for a lower-energy electron to be promoted or a higher-energy electron to fall into the empty state. At absolute zero, every state below a certain energy is full and the remainder are empty. This energy is known as the Fermi energy, and can be calculated if the composition of the system is exactly known. At higher temperatures, this energy is called the Fermi level, and an electronic state at this level has exactly a 50% chance of being occupied. As the temperature increases, more higher level states are occupied and fewer lower level states are occupied.

At room temperature, the interesting electronic activity in a solid occurs at the states closest to the Fermi level. The highest energy band below the Fermi level is called the valence band, and the lowest energy band above the Fermi level is called the conduction band (analogous to the HOMO and LUMO in single molecules). The reason for this nomenclature is that in order for a solid to conduct electricity, its electrons must be free from the potential well produced by any individual nucleus and able to transverse the atomic lattice – that is, these electrons must be in a conduction band. Semiconductors are defined as substances in
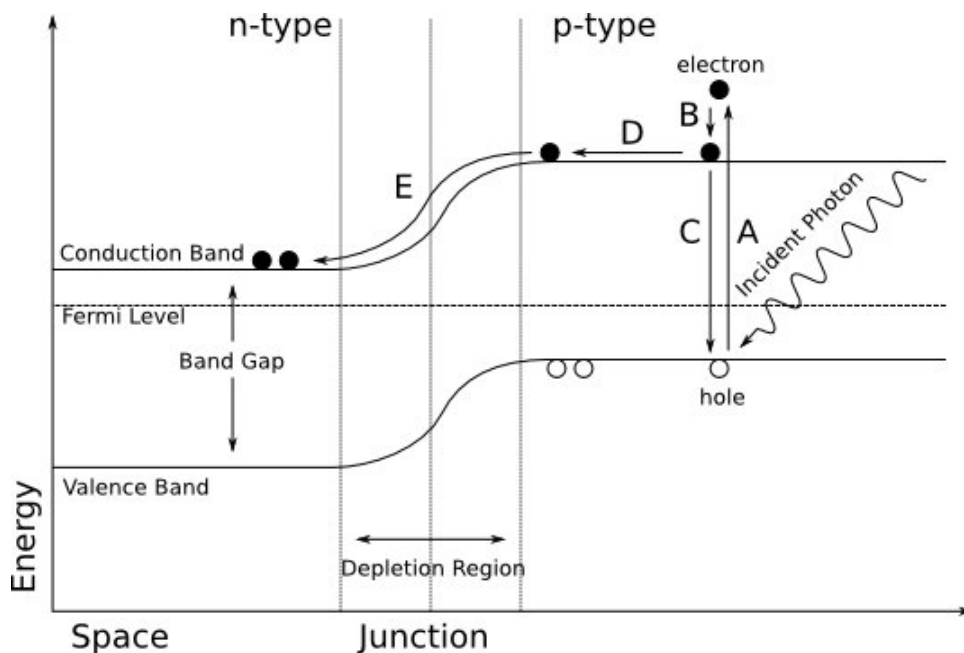
Figure 1.2: A band diagram of a p-n junction showing the process of photovoltaic energy absorption and charge separation. A) photon absorption; B) thermalization; C) recombination, competes with D) charge migration; E) separation across p-n junction.

which the Fermi level is between two bands with a relatively small energy difference. This means that at absolute zero, they conduct no electricity, and at higher temperatures they become progressively better conductors. The difference in energy between the bottom of the conduction band and the top of the valence band is called the band gap, illustrated in Figure 1.2. By comparison, an insulator is a substance with a band gap so large as to all but prohibit electronic conduction and a metal is still an excellent conductor at low temperatures because its Fermi level lies inside the conduction band.

The Fermi level of semiconductors can be affected by doping. Doping is the practice of adding very small numbers of atoms which do not fit in the ideal stoichiometric structure of the semiconductor. Dopants are chosen as donors (n-type), which are more likely to ionize than the atom which they replace in the structure, or acceptors (p-type), which are less likely to ionize, thus making it more likely that the semiconductor's atoms do so instead. This causes n-type semiconductors to have a comparative abundance of electrons in the conduction band, and causes p-type semiconductors to have comparatively fewer electrons in the valence band. Dopants add impurity levels to the band structure of a semiconductor near the valence or conduction band, effectively skewing the band structure so that the Fermi level is closer to the conduction band (n-type) or the valence band (p-type).

Electron vacancies in the valence band, present more predominantly in p-type semiconductors, are often called holes. These can be thought of similarly to bubbles in a liquid. Holes seek the highest possible energy available, which is to say that the electrons whose absence define the hole all seek lower energy states. An electron from the conduction band can decay

into a hole in the valence band in a process called recombination. This releases a photon or thermal energy equal to the band gap. Electrons in the conduction band and holes in the valence band are called charge carriers, for they have the accessible equivalent energy states available to them to allow them to move, conducting electricity.

With these processes in mind, we can now imagine the energy landscape of a p-n junction, depicted in Figure 1.2. Two semiconductors, one p-type and one n-type, are placed together. In this particular case the band gaps of the two materials are equal, but this is not always the case. Any two systems in thermal equilibrium will have a consistent Fermi level. This means that at the junction the valence and conduction bands of the two semiconductors will be discontinuous. Additionally, there will be an abundance of holes on the p-type side and electrons on the n-type side. The charge carriers at the interface will begin to recombine, forming the depletion region, an area in which there are few charge carriers of either type. The valence and conduction bands in the depletion region will develop the slope shown in Figure 1.2 due to this annihilation of charge carriers. Essentially, the electronic structure of each semiconductor becomes progressively more similar to that of the other further into the depletion region.

The steps of absorption and charge separation in a photovoltaic device are shown in Figure 1.2. In A, an incident photon with an energy equal to or greater than the band gap of the material is absorbed, promoting an electron into a vacant space in the conduction band and leaving behind a hole in the valence band where the electron used to be. If the incident photon is lower in energy than the band gap, it will not be absorbed in this process. If the incident photon is more energetic than the band gap, it will be absorbed into a point in the valence band above the band edge. In B, the excess energy is lost as heat through a process known as thermalization. Once the electron-hole pair is created, two competing processes can occur. As in C, the electron can decay back down into the hole state it just vacated, losing the energy it just acquired. This is not desirable. Alternatively, as in D, the electron (or hole, in the case of a p-type absorber) can migrate close enough to the p-n junction to be affected by the attractive electric field of the other side, depicted in Figure 1.2 by the curvature of the band edges. Electrodes for PV are chosen such that an electrical bias slopes the band edges so that migration in this direction is favorable. Once at the junction, the migrating charge carrier will quickly be pulled across the junction as in E. The hole (or electron) it was paired with has the opposite charge and will find progress across the junction very energetically unfavorable. Once the charges are separated, it will be more energetically favorable for the charges to recombine by traveling along an external circuit, powering whatever load is provided.

1.4 Electrodeposition of Metal Sulfides for PV

Many device and materials features have a bearing on the ultimate efficiency of a photovoltaic device. Each of the processes shown in Figure 1.2 must be optimized, and we are ever constrained by the materials with which we can work and the synthetic methods used to

create them. Both iron pyrite and chalcocite have attractive materials qualities for use in photovoltaic structures, and electrodeposition could provide an inexpensive synthetic route towards device structures which can help counter their disadvantages.

1.4.1   Metal Sulfide Semiconductors for PV

Pyrite (FeS$_2$) has gained attention as a material of interest for PV applications [15]. The most attractive quality of iron pyrite for PV is its high absorptivity. The absorption of light by pyrite begins to saturate at a thickness of about 1 μm. To provide comparison, its absorption coefficient (weighted to account for band gap) is two orders of magnitude higher than that of silicon [30]. Additionally, FeS$_2$ has a band gap of 0.95 eV [12], corresponding to a wavelength of 1305 nm. Referring again to Figure 1.1 it is evident that this band gap is sufficiently small to absorb energy from the majority of terrestrial solar radiation. Coupled with the high absorptivity, this means that optimization of process A from Figure 1.2 can occur with much smaller masses of material, decreasing both the material cost and the cost of the balance of system structural components in a finished panel. Synergistically, iron pyrite is also composed of Earth-abundant and easily isolated elements.

Cu$_x$S has a longer and more colorful history in PV research than pyrite. Cu$_x$S was first observed as a PV material in 1954 during testing of cadmium sulfide with various metal contacts, including Cu [31]. It was more than a decade later that the observed PV was fully understood to originate through absorption of light by Cu$_x$S formed by exchange with Cd in the CdS lattice [32]. While the system was promising, with cells approaching 10% efficiency with simple manufacturing techniques [17], eventually it was discarded due to high Cu ion mobility leading to degradation of the Cu$_x$S layer and undesirable doping of the CdS [33, 34]. More recently, interest in Cu$_x$S for PV energy conversion has revived with the discovery of new synthesis techniques [18].

As the nonstoichiometric formula would suggest, Cu$_x$S is a more complex substance than pyrite. Chaclocite (Cu$_2$S) is a p-type semiconductor doped by Cu vacancies [33]. In Cu$_x$S, x $\leq$ 2, indicating progressively increased p-type doping as x decreases. Additionally, Cu$_x$S is stable in many phases at room temperature. Chalcocite (Cu$_2$S to $\sim$ Cu$_{1.993}$S) is orthorhombic, djurleite ($\sim$ Cu$_{1.96}$S) is also orthorhombic, and digenite ($\sim$ Cu$_{1.765}$S to Cu$_{1.840}$S) is pseudo-cubic. All are stable at temperatures below 76º C [35]. It has been found that light absorption decreases with decreasing x [36], and it has been empirically shown that for the CdS-Cu$_x$S cell in particular, the most efficient cells are those of primarily chalcocite phase with x closely approaching 2 [37]. However, heavily doped semiconductors have a place in PV, for example in providing selective contacts at the source and drain electrodes. This implies that despite the otherwise less desirable characteristics of Cu-deficient phases, it is still desirable to find methods for the synthesis of all copper sulfides.

Empirical evidence shows that Cu$_2$S has a direct band gap of 2.48 eV [38, 39], which corresponds to a wavelength of 500 nm. Cu$_2$S also has an indirect band gap (requiring phonon coupling to allow light absorption) at about 1.2 eV [36]. While the indirect gap has much

lower absorbance, reference to Figure 1.1 indicates that the absorption occurs over a much larger portion of the solar spectrum than that captured by the direct gap transition. The absorbance of the indirect gap falls precipitously and shifts to higher energies as the stoichiometry of the compound becomes copper deficient, accounting for the lower efficiency of CdS-Cu$_x$S cells with x < 2. Thus, Cu$_x$S is a comparatively poor absorbing material.

Many of the disadvantages of these low-cost but non-ideal materials can be overcome and their advantages highlighted using proper device structuring – as discussed in Section 1.3, most processes can be optimized using both structure and materials choices. For example, pyrite has been calculated to be most competitive with established PV technologies when incorporated into devices with diffusion / drift length scales between 100 nm and 1 μm. In this regime, the advantages of pyrite's high absorption offset the losses in process B of Figure 1.2 due to its narrow band gap [30]. As examples of ameliorating suboptimal material characteristics with device structuring, bulk heterojunction cells compensate for poor carrier diffusion lengths in polymer solar cells [40] and the proposed radial p-n junction structure solves a similar problem for inorganic cells of low quality materials [41]. The problem with such methods, of course, is that complex device structures are typically very difficult to synthesize in practice, and often the cost of synthesis would outweigh the savings which are the driving force behind using lower quality materials.

1.4.2 Electrodeposition as a Synthesis Method

Electrodeposition was first developed in the early 1800's shortly after the invention of the first battery. It is now an important industrial process – the aluminum industry alone consumes 1.2% of the electricity produced annually in the United States to electrowin pure aluminum metal from a molten salt melt containing aluminum oxide prepared from raw ore [42]. The long history of its optimization and the ability to use mild aqueous solutions under air for synthesis allow for the possibility for this to be very inexpensive synthesis method.

Electrodeposition is a mature synthesis route, and can be used to directly deposit conductive metals [43] as well as binary [44], ternary [45], and even quaternary compounds [46] if the correct deposition bath and conditions are developed. Since electrodeposition occurs wherever the electrode presents high enough current density to the deposition solution, complex device structures can be fabricated through the use of clever templating and solution manipulation techniques [47, 48]. Due to the complexity of multi-component electrodeposition solutions, the technique is still an area of very active research.

The low cost of electrodeposition makes it an attractive synthesis method to complement the inexpensive metal sulfide semiconductors. Its flexibility allows for the creation of the complex device structures necessary to optimize the efficiency of these materials. The main hurdle to clear is obtaining an understanding of the complex solution chemistry of the electrodeposition baths.

1.5   Previous Work

Pyrite has been synthesized through pseudo-electrochemical processes [49, 50, 51, 52, 53, 54, 55, 56]. In each case, FeS or Fe is formed electrochemically, and FeS_2 is created in an annealing step in the presence of excess sulfur. The electrodeposition conditions include simple Fe wire electrodeposition [51], acidified aqueous $(NH_4)_2Fe(SO_4)_2$ and $Na_2S_2O_3$ at elevated temperature on Ti [53, 52], aqueous $FeSO_4$ and $Na_2S_2O_3$ onto Ti [54], S_8 and $FeCl_2$ in diethyleneglycol onto Pt [55], and aqueous $FeSO_4$ onto a sulfur-modified Ag electrode [56]. Tacconi *et al.* are the only group to propose a route toward direct FeS_2 synthesis $Tacconi_{1994}$, but their method does not scale well and they do not present evidence for the formation of FeS_2 as opposed to the more commonly generated FeS. The most common and inexpensive solution system employed is the $FeSO_4$–$Na_2S_2O_3$ system, which has a very complex set of electrochemical reactions. A deeper understanding of this system will help rationalize further attempts to synthesize Fe_2S using electrochemical methods.

A large number of groups have attempted the electrochemical synthesis of copper sulfides, and have undoubtedly succeeded. However, the complexity of the copper-sulfur solid system is greater than that of the iron-sulfur system due to the wide stoichiometric variation in Cu_xS species, and a full understanding of the system requires even more careful study. Anuar *et al.* deposited Cu_xS from solutions of $CuSO_4$, $Na_2S_2O_3$, and EDTA onto titanium, but did not undertake more than a perfunctory examination of either solution electrochemistry or the stoichiometry of their deposited samples [57]. Lai *et al.* used a synthesis method similar to those employed to produce pyrite, first electrodepositing Cu nanowires and subsequently exposing them to H_2S gas to produce Cu_2S [58]. Ghahremaninezhad *et al.* have made mixed phases of covelite (CuS) and djurleite ($Cu_1 \cdot 94\,S$) using pulsed electrodeposition out of baths of $CuSO_4$ and thiourea [59]. Yukawa *et al.* claim the formation of chalcocite and djurleite out of aqueous solutions of $CuSO_4$, $Na_2S_2O_3$, and a tartaric acid buffer onto titanium electrodes, but they do not perform an extensive analysis of the deposition process and they reported poor reproducibility [60]. Grozdanov *et al.* have studied an electroless thin film synthesis of Cu_xS from solutions containing $CuSO_4$ and $Na_2S_2O_3$ through the application of elevated temperatures [61]. A thorough analysis of this system will aid in the future development of reliable synthesis methods for particular phases of this complex system.

1.6   Conclusion

The goal of this thesis is to throughly examine the electrochemistry of the $FeSO_4$–$Na_2S_2O_3$ and $CuSO_4$–$Na_2S_2O_3$ aqueous systems. This is undertaken with the goal of producing reliable and inexpensive synthesis methods for metal sulfide semiconductors of interest for photovoltaic energy conversion. These methods could then be applied to produce nanostructured semiconductor devices. One method of producing nanostructured semiconductor devices, that of template assisted electrodeposition into porous alumina, will also be investigated further.

Chapter 2

Electrochemical Methods

Electrodeposition is a flexible but complex method of synthesis. A detailed understanding of the electrochemical processes taking place in each deposition bath is necessary for the rational design of such syntheses. To that end, a brief overview of the electrochemical principles and methods used in this work is presented in this chapter.

2.1 Overview of Electrochemistry

Very early chemistry research established that electron transfer occurs between chemical moieties as a function of what is now termed the redox potential difference between the two species. Electrochemistry is the art of probing and manipulating these electron transfer reactions through the use of an external potential source, the solution-accessible portion of which is called an electrode. The electrode essentially replaces one half of a redox pair, and can ideally be tuned to any potential, accepting or donating electrons to solution species depending on the need of the researcher.

At least two electrodes are required in order to perform an electrochemical experiment. The first is the working electrode, at which the reactions of interest occur. The second is termed an auxiliary or counter electrode, and is used to complete a circuit across the solution. A third electrode, called a reference electrode, is often used to provide a stable reference point against which the potential of the working electrode can be measured.

In a great deal of electrochemical work, the nature of the working electrode itself is not the focus of the experiment. In such cases an ideal working electrode is very polarizable that is, it can accept a wide range of electrical potentials at its surface and is capable of changing quickly between them. Additionally, an ideal working electrode does not react chemically with any species in solution. Platinum and gold, both unreactive and highly conducting metals, are commonly used as working electrodes. For reproducible, quantitative
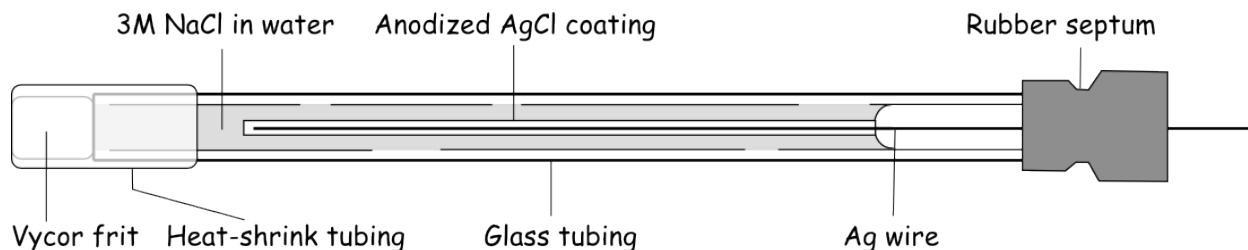
Figure 2.1: This figure displays the component parts of a Ag/AgCl reference electrode.

experiments, a working electrode must have a well-controlled surface area in order for current to be accurately converted into current density.

An ideal auxiliary electrode is polarizable and does not react chemically with the solution, just like an ideal working electrode. An auxiliary electrode usually also has a large surface area in order to prevent anomalous current effects due to insufficient suface area. Platinum or gold gauze are common auxiliary electrodes.

2.1.1 Silver / Silver Chloride Reference Electrodes

Reference electrodes are used when more quantitative and reproducible work is required. They are more complex than auxiliary and working electrodes due to the need to maintain a constant and steady potential. A typical reference electrode contains species contributing to a half-cell reaction, the potential of which is controlled by keeping the activities of the reacting species constant in some manner.

The reference electrodes used in this work employ the Ag/AgCl redox couple in 3 M NaCl. It has a potential of +209 mV against the normal hydrogen electrode (NHE) in aqueous solutions. The Ag/AgCl electrode relies upon the fact that AgCl is sparingly soluble in water. As long as both solid silver and solid AgCl are present in the system, the amount of Ag^+ in solution can be tuned via Le Châtelier's principle by holding the Cl^- activity constant using chlorides of innocuous cations, typically KCl or NaCl. This fixes the activities of every species in the reaction

$$AgCl_{(s)} + e^- \rightleftharpoons Ag_{(s)} + Cl^-_{(aq)} \tag{2.1}$$
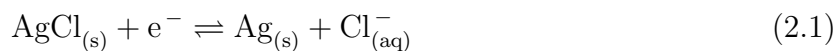
as long as the amount of current passed through the system is not enough to deplete the supply of either solid reagent. A reference electrode can be constructed with a porous glass frit that slows ionic diffusion enough to prevent substantial contamination of either the reference solution or the solution of interest.

Figure 2.1 displays a diagram of a homemade silver / silver chloride electrode. These electrodes are constructed from a body of 4 mm glass tubing 6-8 cm in length. The tubing is

capped with a Vycor® porous glass frit one one end, held in place with Teflon® heat-shrink tubing that is trimmed to fit with a razor blade. The body of the electrode is filled with 3 M NaCl solution. A rubber septum is fitted on the tube end opposite the frit. This septum is pierced with a needle to admit a thin silver wire 6-7 cm in length, such that it is both immersed in the liquid inside the electrode body and protrudes slightly from the septum. The electrode is then connected to an electrochemical cell with the silver wire serving as the working electrode, a piece of platinum gauze serving as both the counter and auxiliary electrodes, and using 3 M NaCl as the electrolyte. A galvanostatic current of 0.04 mA is applied to the electrode for 3 hours. This coats the silver wire with an even layer of AgCl. The electrode is stored in 3 M NaCl solution in a light-proof container to prevent photooxidation of the silver.

2.1.2   Salt Bridges

A salt bridge is a conduit between two solutions which facilitates charge transfer but prevents the exchange of species between the two solutions. In addition to being used to explore chemistry between two separate solutions, they are also employed when a solution under investigation is incompatible with one or more of the electrodes used to investigate it. It is in the latter capacity that salt bridges are most often employed in this work.

Salt bridges contain an immobile mixture containing mobile cations and anions. The cation and anion chosen for this mixture are selected to have mobilities which are both high and of a similar magnitude to minimize the potential formed across the junction between the bridge and the solution. These ions will conduct current from one side of the salt bridge to the other. Ions from one solution in which the salt bridge is immersed will diffuse a short way into the salt bridge. To balance this charge buildup, correspondingly charged ions from the other end of the salt bridge which originate from the salt bridge fill mixture will diffuse into the second solution. If innocuous ions are chosen for the salt bridge solution, the electrochemical reactions on either end of the experiment will be unaffected. Naturally, as the ends of the salt bridge get contaminated it must be replaced.

The salt bridges employed in this work use gelled agar as the supporting medium and $NaNO_3$ as the charge transfer facilitating species. A solution of 2.5 g $NaNO_3$, 0.75 g agar, and 25 mL water is alternately heated and cooled until the room temperature liquid flows freely but not quickly. It is then poured into a bent piece of half-inch glass tubing and allowed to set. Once set, the salt bridge is cleaned and excess filling is trimmed away before the structure is ready for use. The salt bridge armature is reused should the salt bridge need to be regenerated.
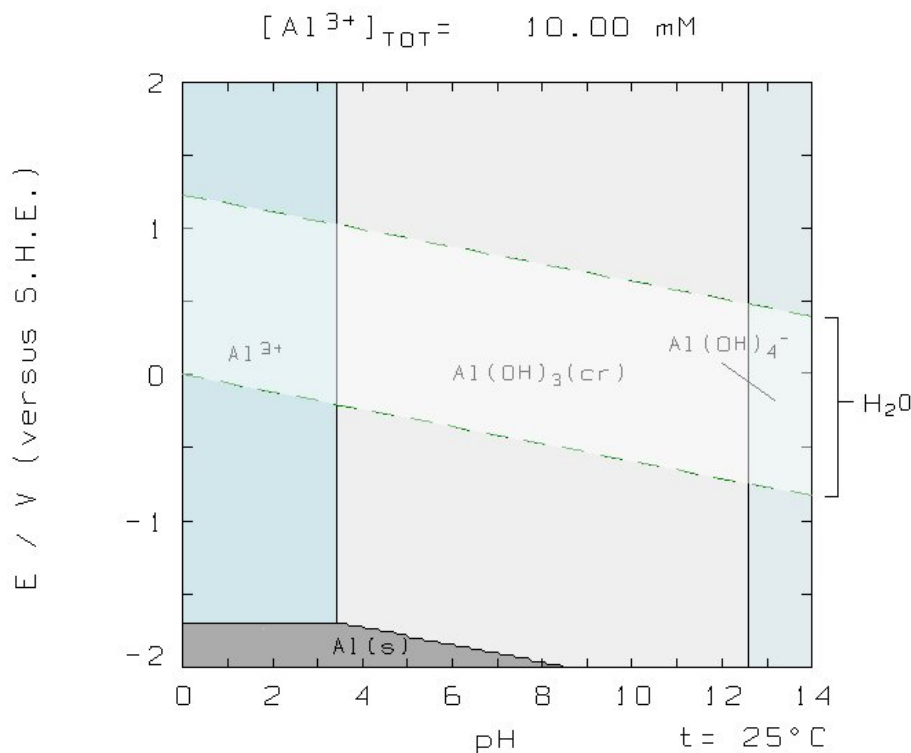
Figure 2.2: Pourbaix diagram for a system with 10 mM in aqueous Al species at 25° C, generated using Medusa [2].

2.2 Pourbaix and Fractionation Diagrams

The Pourbaix diagram is a useful and intuitive visualization of thermodynamic data developed by Marcel Pourbaix during his doctoral work [62]. These figures are also known as potential-pH diagrams, E-pH diagrams or, most generally, predominance diagrams. A typical figure is a two-dimensional plot showing solution space in an aqueous solution — essentially a phase diagram for aqueous solutions. The x axis is pH, while the y axis is the electrochemical potential of the solution relative to the standard hydrogen electrode (SHE). The solution space is divided into regions showing the predominant species in solution at each pH and potential. Each line on the diagram is calculated from tabulated values for the free energy of formation of the species involved. Since Pourbaix diagrams have been used extensively in this work, the information that they convey is summarized below.

Figure 2.2 displays a Pourbaix diagram in which the activity of soluable Al^{3+} species has been held at 10 mM. Each region of the graph has been color-coded for easy identification. Most Pourbaix diagrams include two parallel diagonal lines (seen in Figure 2.2 crossing the Y axis at 0 V and 1.23 V); these denote the region of thermodynamic stability of water at the temperature being investigated. This region has been lightened in Figure 2.2. This is the region with which an aqueous chemist is primarily concerned. In an area above the upper line, the applied potential will cause water to oxidize to O_2, releasing H^+, while below the

lower line water will reduce to H_2, releasing OH^-.

The calculation of the region of water stability will serve as a simple and useful example of the process behind calculating each line on the diagram. The goal is to get a mathematical relationship between the potential (E) at which the reaction will be in equilibrium and pH ($-\log\{H^+\}$). To this end, we start with the two chemical equations we wish to model and calculate the Gibbs free energy of the reaction using tabulated values [63].

$$O_2 + 4\,H^+ + 4\,e^- \rightleftharpoons 2\,H_2O; \qquad \Delta G^o_{rxn} = -474.2 \quad kJ/mol \tag{2.2}$$

$$2\,H_2O + 2\,e^- \rightleftharpoons H_2 + 2\,OH^-; \qquad \Delta G^o_{rxn} = 159.4 \quad kJ/mol \tag{2.3}$$
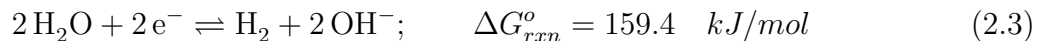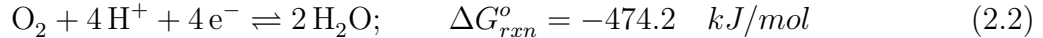
Since electrical potential is of interest rather than ΔG, it is useful to turn to the standard relationship

$$\Delta G^o = -nFE^o \tag{2.4}$$

wherein n is the number of electrons in the reaction as written, F is the Faraday constant of 96485 C/mol, and E^o is the standard reaction potential. The E^o for Reactions 2.2 and 2.3 are 1.23 V and -0.826 V, respectively. A second conversion is needed to account for the fact that the reactions being considered are not carried out under standard conditions (STP plus 1 M concentrations of all analytes). The Nernst equation is used to calculate E from E^o if the conditions are known.

$$E = E^o - \frac{RT}{zF}\ln Q \tag{2.5}$$

Here, R is the universal gas constant of 8.314 J/K mol, T is the temperature in Kelvin, z is the number of moles of electrons transferred in the reaction, and F is the Faraday constant. Q is the reaction quotient, which is defined as

$$Q = \frac{\{C\}^c\{D\}^d}{\{A\}^a\{B\}^b} \tag{2.6}$$

for a chemical equation of the general form aA + bB $\rightarrow$ cC + dD. One final relationship of use converts between natural log and log base 10:

$$\ln x = 2.3026 \log x \tag{2.7}$$

A generic relationship between E and the activities of species in solution is obtained by combining Equations 2.5, 2.6, and 2.7 and plugging in values for the constants, taking T as room temperature at 298 K.

$$E = E^o - \frac{0.059}{z}(c\log\{C\} + d\log\{D\} - a\log\{A\} - b\log\{B\}) \tag{2.8}$$

The activities of all gaseous species, pure solid species and the pure aqueous solvent are set by convention to 1. Since $\log(1) = 0$, such species will not affect the resulting line. Finally, since pH = -log[H$^+$], it will be easy to use this equation to find the relationship between E and pH, which is what we were after all along. This can be applied to the water oxidation reaction in Equation 2.2 as an example.

$$E = 1.23 - \frac{0.059}{4} * (2\log 1 - \log 1 - 4\log\{H^+\}) = 1.23 - 0.059pH \tag{2.9}$$

This is the equation of the upper boundary line of the water stability region in Figure 2.2.

The reduction equation isn't quite so simple due to the fact that it involves OH$^-$, which is in constant equilibrium with H$^+$, and for that reason affects the pH. This problem is easily overcome, however, using the relation pH + pOH = 14 at STP. Thus, for this reduction reaction the result is

$$E = -0.826 - \frac{0.059}{2} * (\log 1 + 2\log\{OH^-\} - 2\log 1) = -0.826 + 0.059(14 - pH) = 0 - 0.59pH \tag{2.10}$$

This gives the lower water stability line in Figure 2.2. This same procedure can be followed even for very complex systems, so long as the free energies of formation of all the compounds and complexes involved are known.

Even in the simple Al system displayed in Figure 2.2, the Pourbaix diagram gives us very useful insights. First, we note that alumina is amphoteric. At near neutral pH's, the neutral $Al(OH)_3$ will form in solution, eventually precipitating. At very basic pH's the $Al(OH)_4^-$ anion is predominant, and at very acidic pH's the Al^{3+} cation predominates. As charged species, these will both be easily solvated by the highly polar solvent, dissolving alumina introduced to such solutions.

Another feature to notice is that aluminum metal is not thermodynamically stable in water. The fact that its region of stability is so far below that of water indicates that aluminum metal exposed to water will oxidize as the solvent is reduced to H_2. The observation that aluminum ladders do not in fact dissolve if left out in the rain is explained by the well known passivating layer of water-stable alumina that forms on the surface of aluminum metal upon exposure to water.
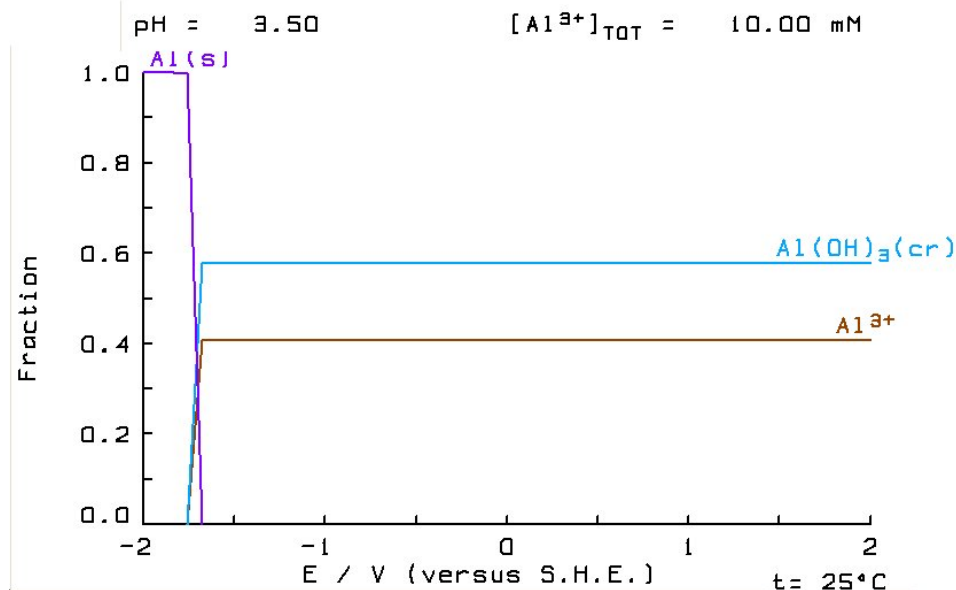
Figure 2.3: Thermodynamically calculated species fractionation of 10 mM Al as a function of potential at pH 3.5, generated using Medusa [2]

The passivating layer of aluminum is an example of the major limitation of Pourbaix diagrams. These diagrams do not provide any indication of metastable states or kinetic factors, such as the extremely slow kinetics of alumina separation from aluminum in pH neutral solutions. In our particular investigation, it is worth remembering that local conditions at the electrode can be significantly different from those which would eventually be most thermodynamically stable.

Another limitation of Pourbaix diagrams is that they only indicate the major solution species at any given point. Entropically, all possible species are present in a solution, even if most of them are at extremely low concentrations. Sometimes, especially in regions close to one or more boundaries on the diagram, the presence of multiple other species means that the indicated species might not even constitute a majority of the solution species at that area in solution space, only the single most abundant of multiple competing species.

A way of deconvoluting this information can be obtained using the same basic thermodynamic calculations that produce the E-pH diagram to instead take a 'slice' out of the diagram, allowing the elucidation of species fraction in the y axis. An example of such a plot from the system in Figure 2.2 is displayed in Figure 2.3. Here, despite the fact that the Pourbaix diagram indicates that $Al(OH)_3$ predominates over most of the solution space, we can see that there is still a significant amount of Al^{3+} in solution as well.
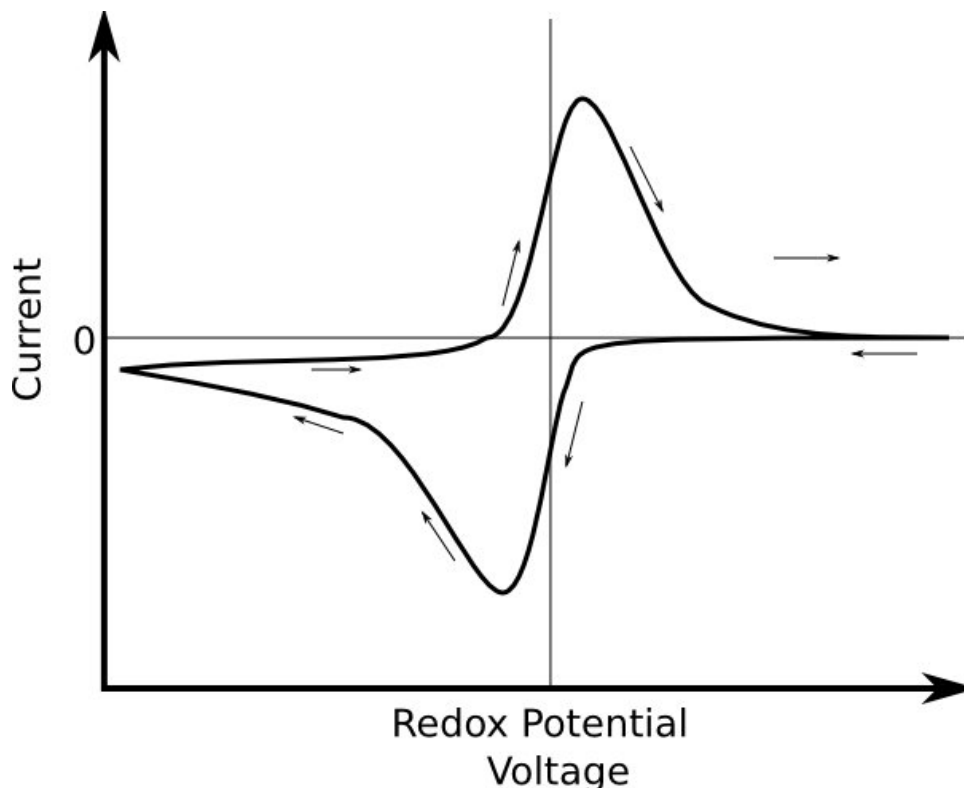
Figure 2.4: Cartoon showing an idealized cyclic voltammogram over the potential of a redox couple between two solution species. Arrows indicate the direction of the scan.

2.3   Cyclic Voltammetry

Cyclic voltammetry is a well known analytical method that was used extensively to probe the properties of solutions in this work. As with most electrochemical techniques, it involves the perturbation of a system with an electrical potential and monitoring the current response. Cyclic voltammetry is characterized by the application of a cyclic, saw-toothed waveform. When using cyclic voltammetry to probe a solution, one gains a wealth of information about the electrochemically active species present in such a solution. As it is such an important part of the analysis in this work, A brief introduction to the technique is presented below.

Figure 2.4 displays an idealized cyclic voltammogram scanning over a single solution redox couple. The direction of the scan is indicated by the arrows. At the beginning of this scan, A^{2+}, a hypothetical solution species, is present in solution. In this example, the A^+ species is also stable in solution. The scan is started at a potential more positive (anodic) than the reduction potential of A^{2+} to A^+. As the potential is decreased (made more cathodic and less anodic), the only current observed will be that due to the charging of the electrode. As the potential approaches the redox potential, the current begins to become more negative, or cathodic. This indicates that the reaction $A^{2+} \rightarrow A^+$ is beginning to occur. At this point, current is being produed only when an electron gains enough energy to drive a single reaction through a combination of the potential supplied by the electrode and the ambient

thermal energy in the system. The magnitude of this current is increased due to the higher energy of the supplied electrons as the applied potential becomes more negative.

The increase in potential is correlated with an increase in current due to the greater likelihood of electrons at the electrode surface of having enough energy to react until another factor limits the reaction rate. Each time the reaction occurs, an A^{2+} ion at the electrode surface is consumed. After a short time, all of the A^{2+} ions near the electrode have been converted to A^+, and in order for the reaction to continue, more ions must diffuse from further away. This limiting factor is what causes the magnitude of the current to pass through a peak and then decrease (with a time dependence equal to $1/sqrtt$) despite the increasingly cathodic potential as the scan progresses. It is important to realize that during this entire period the reduction reaction is still occurring; it simply is not progressing as quickly as it did at the reductive peak due to the depletion of the reactant.

After the potential scan switches direction, the reductive reaction continues to occur, still slowed by the need for reactants to diffuse from farther and farther away. As the potential nears the redox potential from the cathodic side, the reverse reaction begins to occur. The rate is increased initially by the fact that all of the A^+ in solution has been created immediately adjacent to the electrode surface and has not had time to diffuse to equilibrium across the bulk solution. The anodic current will level off and begin to drop once the A^+ at the surface has been consumed and the reaction rate is again limited by the diffusion of more distant ions.

Knowing these basic ideas, a great amount of information can be extracted from solution analysis with cyclic voltammetry. The particulars of such information will be discussed at greater length in the subsequent chapters as they come up. For a much more detailed accounting of cyclic voltammetry and electrochemistry in general, readers are referred to the excellent book *Electrochemical Methods* by Bard and Faulkner [64].

2.4   Templated Assisted Electrodeposition

Template assisted electrodeposition is a technique first explored in the group of Charles Martin [48]. The technique is straightforward in concept. A conducting electrode is modified by a nanoporous masking layer, or template. The masked electrode is then placed into an electrolyte bath containing appropriate precursor solution species. A voltage is applied to the electrode and wires are electroplated up from the electrode into the unmasked space of the porous membrane.

There are a number of readily apparent advantages to this technique over other methods of nanomaterials synthesis. This technique produces large numbers of nanowires at a time, unlike such methods as bombardment etching [65]. Template assisted electrodeposition also produces wires that are oriented in parallel in a robust structure, the geometry which is most favorable to the majority of nanowire applications. This is in contrast with many other

synthetic methods such as vapor-liquid-solid (VLS) and solution phase processes, which produce a disordered array of wires unless carefully controlled [66]. By the nature of the technique, all wires in the template must be electrically continuous, a property not shared by the pressure injection method [67], another common form of template-directed nanomaterials synthesis. Finally, the technique is less expensive both in terms of equipment and precursors than analogous atomic layer deposition (ALD) methods.

Naturally, not all is rosy in the world of templated deposition. There are reasons that templated deposition is not the sole route towards nanomaterials synthesis. Most obviously (and usually, least problematically), only electrically conductive species can be synthesized using this route. Secondly, electrochemical systems can be extraordinarily complex, relying on the correct combination of applied voltage, electrode materials, precursor species, supporting electrolytes, and complexing moieties to produce the desired compound, compounded by a relatively complex time dependence arising from depletion and diffusion of solution species. This is an advantage in that it provides a large number of variables which may be explored in order to deposit exactly the materials desired. However, it requires that a large number of variables be explored in order to deposit exactly the materials desired. Finally, and most distressingly, electrodeposition is a synthetic route which does not necessarily grow materials through crystallization. One of the attractive qualities of many methods of nano-scale synthesis is the ability to create perfect, single-crystal structures by virtue of the synthesis mechanism itself; it is much more difficult to achieve similar results with templated electrodeposition. However, many of these drawbacks can be overcome through the application of fundamental research, and extending the boundaries of our knowledge of this field is a primary goal of this research.

2.4.1 Porous Anodic Alumina

In our experiments, wires are prepared using a membrane of porous anodic alumina (PAA). PAA is a well-studied material [68, 69], although new discoveries are constantly being made on the system. It has been known for more than a century that aluminum forms a barrier layer of oxide when exposed to air or water, passivating it to dissolution by reducing H_2O to H_2. The thickness of this layer can be increased though the application of an oxidizing voltage, and this became a common surface treatment to increase the resilience of aluminum items [68]. In 1932 the morphology of the oxide films formed in certain electrolytes was examined, and the structures were discovered to be extremely porous [68]. Through years of experimentation, the properties and mechanisms of formation of these pores became better understood, and experimental methods were established allowing fine control over pore geometry. The most noted feature of these pores is their spontaneous organization into extremely high aspect ratio nano-scale arrays.

The mechanism behind the formation of organized PAA is still an area of active research, and a number of mechanisms have been proposed [70, 71, 72, 73]. For our purposes, however, the debate over the exact mechanism is less important than the empirical results. A
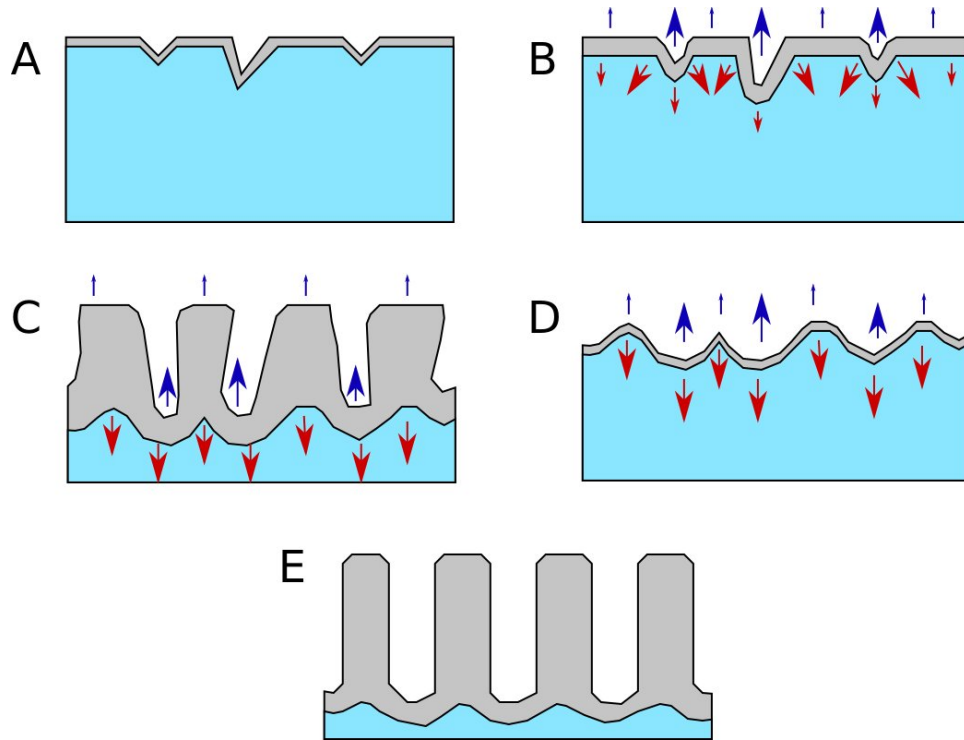
Figure 2.5: Cartoon displaying the formation of porous alumina. Gray indicates alumina and light blue is aluminum. Blue arrows indicate relative rates of alumina dissolution by the electrolyte bath and red arrows indicate relative rates of alumina formation by the applied potential. Note that the vertical and horizontal axes of this cartoon are massively out of scale.

prescribed set of experimental conditions is required to make PAA in the organized fashion most useful for nanomaterials synthesis [70]. The method our lab uses to prepare standard PAA templates involves a double anodization [74] in order to obtain highly ordered pores without a separate templating step.

Figure 2.5 shows the processes occurring during each step of the anodization as cartoons. We use an aqueous solution of 0.2 M oxalic acid for both anodization steps. Thin aluminum foil is mechanically polished to a mirror finish. This starting step is seen in cartoon A. There are still nano-scale imperfections in the surface, and a thin layer of passivating oxide forms upon contact with the air. The foil is epoxied to a glass microscope slide so only one face is exposed, and then it is immersed in the anodization bath at room temperature and anodized at 40 V for 3-5 hours. During this time, the processes shown in cartoons B and C occur. In cartoon B, two competing factors are seen. Blue arrows indicate the dissolution of alumina by the weakly acidic electrolyte solution. Red arrows indicate the oxidation of aluminum to alumina by the applied voltage. Both the rate of formation and the rate of dissolution of the alumina are accelerated at the bottom of pits. This is explained by Su *et al.* [72] as due to the increased charge density present at negative inflection points in the electrode and the increased exposure to O^{2-} diffusing into the alumina later at positive inflection points in
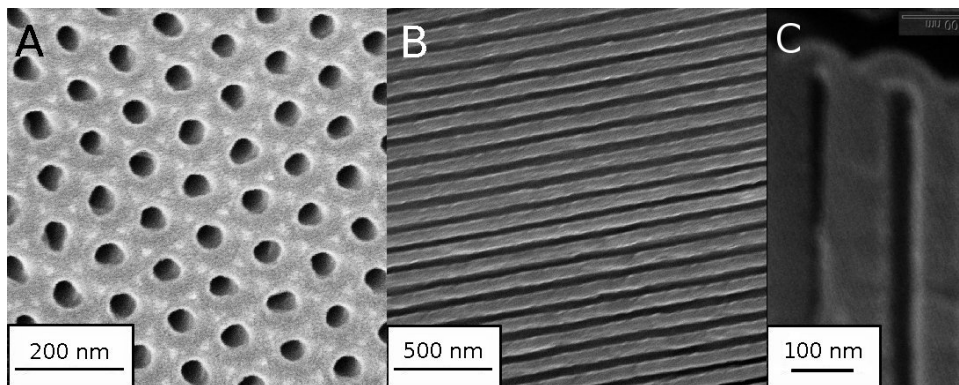
Figure 2.6: Scanning electron micrographs of porous anodic alumina created using a double anodization scheme in 0.2 M oxalic acid at 40 V. SEM A displays an image looking down onto the top surface of the film. SEM B displays an image of a cross-sectional area of the template, displaying the highly parallel pores. SEM C shows a close-up of a cross-sectional image of the barrier layer present at the anode side of each pore.

the aluminum. After a period of anodization, the self-organization of the pores caused by charge density effects [72], the mechanical expansion of aluminum as it forms alumina [70], competition between oxidation and dissolution rates [71], and/or stress resulting from the flow of O^{2-} into the film [73] causes the bases of the pores to be much more organized than the tops. The final result of a well-tuned anodization is a set of monodisperse parallel pores which are open to solution at one end and capped with a barrier layer of alumina before terminating at the aluminum anode, as depicted in cartoon E.

The double anodization method uses the more highly ordered nature of the divots present in the aluminum at the base of the pores formed by an initial anodization step to start the pores of a second anodization in a more ordered fashion, as seen in cartoon D. The alumina layer on the anode is stripped off using a warm solution of chromic and phosphoric acid. After washing and re-insulating the aluminum, we then perform our second anodization in a $0\,^{\circ}$ C ice bath in order to improve the ordering of the pores by slowing their growth. At this temperature in 0.2 M oxalic acid, one hour of anodization will result in roughly two microns of well-organized pores, up to a maximum length of about 120 microns.

SEM images of PAA templates formed using the above process can are shown in Figure 2.6. The pores are between 35 and 40 nanometers in diameter and remain parallel and very monodisperse across the entirety of the template. Pore branching does occur but with exceeding rarity, with the majority of pores being parallel for their entire length. The hexagonal ordering of the template occurs in domains of many microns. The thickness of a barrier layer visible in SEM C is about half the inter-pore distance.

There are a few methods of preparing these templates for electrodeposition. The first is to simply use AC current to deposit nanowires, treating the thin barrier layer as a rectifier [75]. This unfortunately leaves the nanowires with an insulating junction at one end, which is unsuitable for a number of applications. Another method is to thin the barrier layer using an

acidic or basic solution and then deposit using the aluminum beneath the barrier layer as the cathode. Since aluminum is not an ideal electrode for all solutions, an alternate method is to sputter another metal, typically platinum, on the porous surface. The aluminum anode and the barrier layer are then etched away to allow solution access to the sputtered electrode. This process, using a thin Ti wetting layer for a Pt sputtered layer, is the source of the electrodes used in this work unless stated otherwise.

2.5   Experimental Methods

Electrochemistry of a complex solution allows the manipulation of a large number of variables, and as the other side of that coin, necessitates the control of these same variables in order to obtain reproducible results. The experimental method detailed below was designed to control and allow for the manipulation of as many variables as possible.

The most obvious control parameter is the concentration of electroactive species in solution — namely, Cu in various compounds, S in an even wider variety of species, and H^+. The copper source was $CuSO_4$, obtained as 99% pure $CuSO_4 \cdot 5\,H_2O$ from EDS. The iron source was $FeSO_4 \cdot 7\,H_2O$ from Fischer. The additional sulfur source was $Na_2S_2O_3$, obtained as 99.5% pure $Na_2S_2O_3 \cdot 5\,H_2O$ from EDS. The adjustment of sample pH was achieved by using sulfuric acid, obtained concentrated at 95-97% from EDS. Water used was filtered from house deionized water using a Millipore Milli-Q integral water filtration system.

Stock solutions of 1 M $CuSO_4$ and 1 M $Na_2S_2O_3$ were prepared and used to make the solutions of interest in the appropriate concentration. Each solution was diluted to close to its final volume, then titrated to the desired pH using a 1:100 ratio of H_2SO_4 to water. The solution was then diluted fully and the final pH measured. Initial measurements were taken immediately after the creation of the solution in order to ensure that the kinetically slow thiosulfate decomposition reaction did not adversely affect results. Temperature was monitored generally but not specifically - that is, experiments were not undertaken if the laboratory temperature fluctuated above 25° C or below 20° C, but the exact temperatures were not recorded within this range.

Cyclic voltammograms were obtained using homemade potentiostats run through a homemade LabView interface, detailed in the Appendix A.1. Unless otherwise stated, cyclic voltammograms were run at a rate of 50 mV / sec. For most cyclic voltammograms, 10 cycles were undertaken in a series to explore the effects of electrode modification during the experiment, if any. Finally, each solution was run twice in order to control for the effects of solution age. One solution was run immediately after creation and the second some time later.

Chapter 3

Electrochemistry of Aqueous Na$_2$S$_2$O$_3$

The aqueous electrochemistry of sulfur is very complex. It is stable in a variety of oxidation states and often forms multiple stable compounds with a single other element. Understanding the behavior of sulfur in a specific aqueous system requires a firm grounding in the literature. The purpose of this chapter is to explore what is known about the aqueous electrochemistry of thiosulfate and its daughter compounds and to apply that information to understanding our system of interest.

3.1   Behavior of Aqueous Sulfur Compounds

Sulfur is a rock-forming element comprising close to 3% of Earth's mass [76]. It is essential to terrestrial life and a component of two amino acids. Its primary acid, H$_2$SO$_4$, is so vital to modern manufacturing, production, and large-scale agricultural practices that its volume of production is used as a primary indicator of a nation's industrial strength [7]. Sulfur compounds are used in agriculture, metallurgy, artificial textiles, paper, rubber, pigments, and many other applications [7].

With the broad application of the element, it is no wonder that aqueous sulfur chemistry has been studied by a large number of researchers. They have their work cut out for them, as sulfur also exhibits extremely complex aqueous chemistry. Like other elements in the Chalcogenide Group (group 16), sulfur has 6 valence electrons. Unlike oxygen, however, sulfur is capable of accomodating more than eight electrons when forming compounds. The textbook explanation of this phenomenon is through (*e.g.*) d^2sp^3 hybridization. Molecular orbital calculations indicate that the sulfur bonds are more accurately modeled as having significant ionic character with very little contribution from the d orbitals [77]. This flexible valence capacity means that sulfur atoms in molecules and extended solids can be found in formal oxidation states of every integer between -2 and +6 with varying stability and with coordination numbers up to six [78]. Analysis of aqueous sulfur solutions is complicated by

the vast array of oxide compounds made possible by varying oxidation states, coordination numbers, and oligomerization. Many of these solution species are in a state of dynamic equilibrium with one another. Because sulfur equilibria are so complex and the element is ubiquitous in modern chemical processes, sulfur chemistry is still an area of active research after decades of work.

Thiosulfate, $S_2O_3^{2-}$, is a particularly interesting sulfur compound. It contains a sulfur-sulfur bond between two atoms with two different oxidation states (variously set at VI and -II [79], V and -I [80], or IV and 0 [7]). While an oxidation distribution of V/-I is indicated by analysis of the charge density around the sulfur atoms in thiosulfate molecules using X-ray absorption near edge structure (XANES) spectroscopy [80], the VI/-II assignment allows a more intuitive grasp of the structure by analogy with the familiar SO_4^{2-}. The existence of these two widely different oxidation states makes thiosulfate an attractive sulfur source for electrodeposition, since other sulfur species are either too reactive (S^{2-}) or too stable (SO_4^{2-}) for electrochemical tuning.

Of course, in order to use species in a rationally designed electrochemical synthesis, it is important to know their behavior both in solution and when exposed to the universal reactant that is the electrode. Figure 3.1 is a simplified but reasonably complete diagram of the behavior of aqueous sulfur species. The diagram is biased towards thiosulfate, and shows a more complete set of reactions involving this species. The diagram is organized from bottom to top in order of increasing average formal charge on the sulfur atoms of the species. Acidified forms of the species listed are omitted for the sake of clarity, but would be universally present in aqueous solutions. The stoichiometry of reactions, including the acidic stabilization of leaving groups, is not indicated in the diagram. To use a phrase that has become the bane of chemistry students for generations, the evaluation of these stoichiometries is left as an exercise for the reader. Reactions with labeled arrows are electrode reactions, which are hypothesized to proceed by mechanisms detailed below. Reaction A is an electro-oxidation reaction with the sequential transfer of electrons and one oxygen atom. Reaction B is the corresponding reduction reaction involving the loss of one oxygen and the transfer of electrons. Reaction C is similar to reaction B, but involves the loss of a S^{2-} ion rather than oxygen.

We should start with a look at spontaneous thiosulfate reactions in aqueous solutions. Specifically, since we're interested in doing depositions from solutions that are acidified in order to prevent metal oxide formation, we should examine the behavior of thiosulfate in such solutions. It is well known that when thiosulfate is immersed in an acidic solution it produces a mixture of SO_2, colloidal sulfur (S_8 and S_6), H_2S, and polythionic acids ($S_{2+x}O_6$, x > 0) [5]. This reaction is depicted along the right-hand side of Figure 3.1.

The mechanism of the formation of these diverse species has been the subject of some debate [4, 5], with kinetic arguments being complicated by the variety of species produced. The most commonly accepted mechanism for the formation of the colloidal sulfur visible as an immediate clouding in acidified thiosulfate solutions is shown in Figure 3.2. The first step is an encounter between an acidified thiosulfate and a nucleophilic S^-, resulting in a
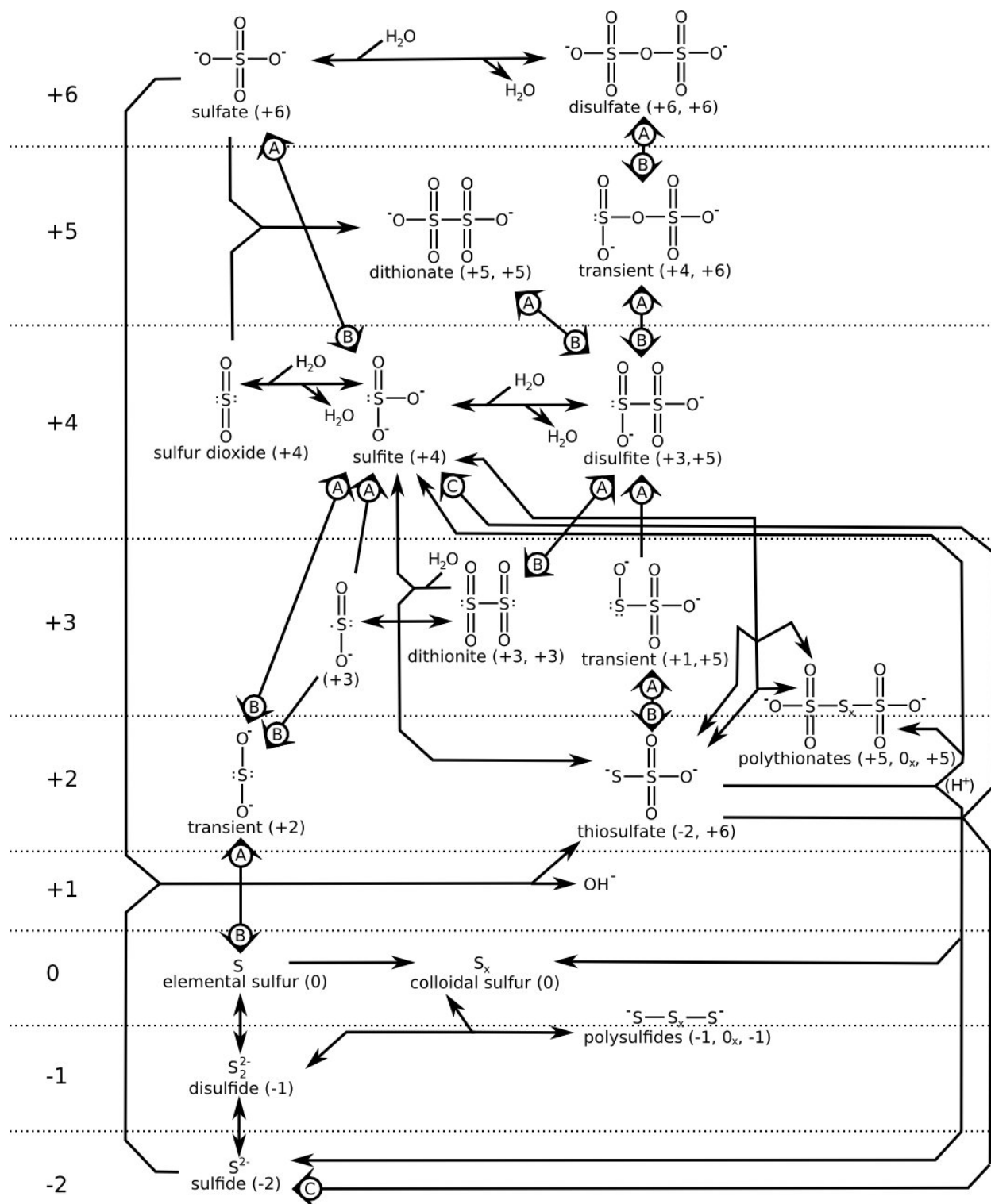
Figure 3.1: Simplified depiction of sulfur speciation in solution in the presence of an electrode. Reactions compiled from references [3, 4, 5, 6, 7, 8]. The species are organized in decreasing order of average sulfur oxidation state, as noted to the left of the diagram. The formal oxidation state of each sulfur in the species is listed with its name. Labeled reactions require the input of an electrode potential; those proceeding by the mechanism detailed in Figure 3.4 are labeled A, those proceeding by the mechanism in Figure 3.5 are labeled B, and those using the mechanism in Figure 3.6 are labeled C.
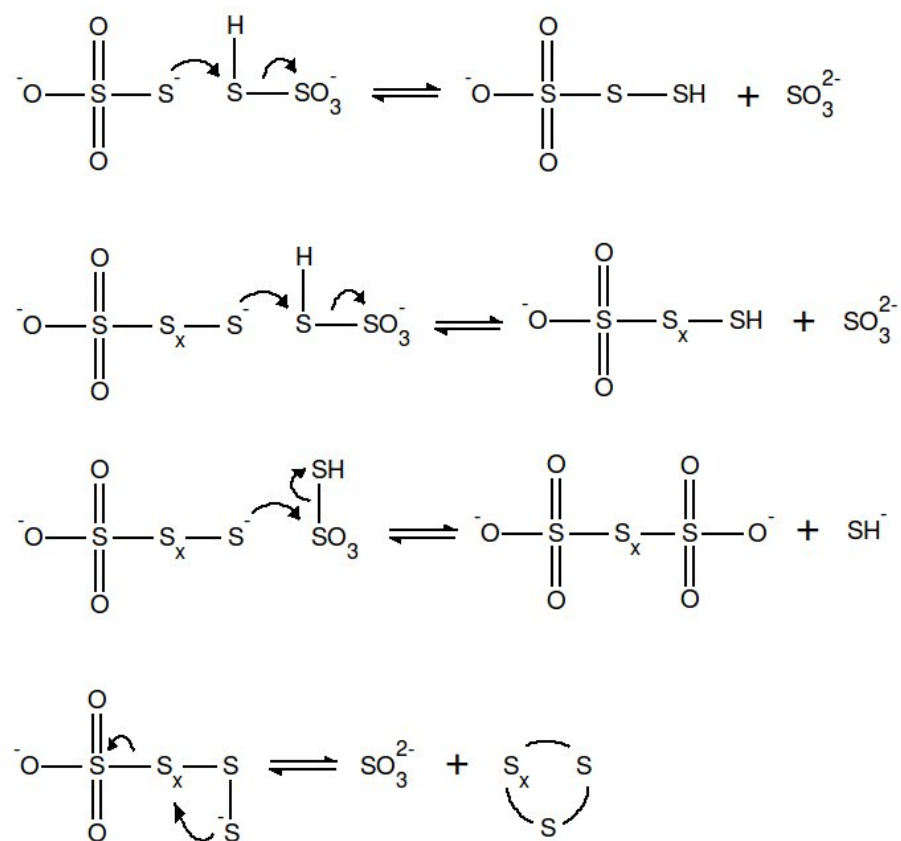
Figure 3.2: Accepted mechanism for the acid-enabled decomposition of thiosulfate to sulfite and S_8 with side products of sulfide and polythionic acids [4, 5].
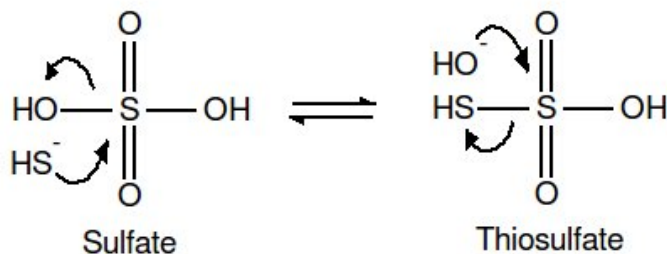
Figure 3.3: This figure shows the accepted mechanism for the interconversion between sulfate and thiosulfate. This reaction only proceeds towards the disproportionation of thiosulfate at elevated temperatures [4].

nucleophilic displacement reaction, producing sulfite, one of the observed reaction products. This reaction is repeated, increasing the length of the sulfur chain at the end of the base thionic acid and producing further sulfite. The growth of the chain is terminated in one of the two following mechanisms. In the first possibility, the more oxidized central sulfur of the activated thiosulfate experiences a nucleophilic attack from the sulfur chain terminus. This displaces the lower oxidation state sulfur as SH^- and produces a polythionic acid, accounting for these two observed reaction products. The other chain termination possibility involves the nucleophilic attack by the end of the long sulfur chain on the chain's own oxidized end, producing a cyclic colloidal sulfur species and another sulfite.

Thiosulfate can also spontaneously disproportionate into sulfate and sulfide [4]. The most likely mechanism for this reaction is depicted in Figure 3.3. While the forward reaction (producing thiosulfate by mixing sulfide and sulfate) proceeds fairly quickly, the reverse decomposition only occurs at elevated temperatures (between 250 and 300 ^{o}C). Thus, thiosulfate is unlikely to undergo this decomposition, but it is worth noting that the formation of sulfide at the electrode in a sulfate solution will produce thiosulfate as the reaction product diffuses into and reacts with the bulk. This reaction is shown proceeding only in the HSO_4^- + HS^- → $HS_2O_3^-$ + OH^- direction to the right of Figure 3.1.

Once oxidation and reduction at the electrode become involved, the system naturally becomes more complex. Sulfur can access a variety of oxidation states in solution, but how exactly it attains the oxide configuration observed in each case is important. Johnson and colleagues have extensively studied the interaction of electrodes and electroactive analytes with an eye toward optimizing particular reaction schemes by altering the composition of the electrode itself [81]. Brevett and Johnson explored the oxidation of $S_2O_3^{2-}$ [6], attempting to optimize the quantitative oxidation of thiosulfate to sulfate for the purposes of waste management. The underlying principle of their approach is that oxidation of sulfur at the electrode occurs through the mediation of an adsorbed OH^- at the surface of the electrode, and the efficiency of a particular electrode at oxidizing the sulfur is reliant on how well it forms these adsorbed, 'activated' hydroxide intermediates.
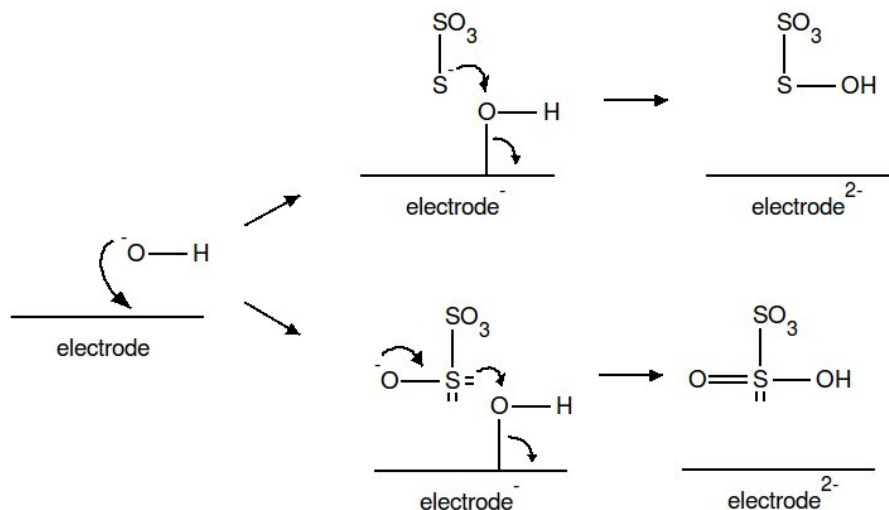
Figure 3.4: Proposed mechanism for the hydroxide-mediated electro-oxidation of thiosulfate, a mechanistic representation of the idea proposed by Johnson *et al.* [6].

Brevett and Johnson performed a series of amperometric and coulombometric studies to probe the kinetics of their electrode reactions, and combined these data with a wet chemical analysis of the resulting solutions once they had been oxidized to completion. They were able to elucidate a reasonable series of reactions that are included among those in Figure 3.1. Their experiments were carried out in $NaHCO_3/Na_2CO_3$ buffer at pH 10.

Figure 3.4 displays a reasonable mechanism for the hydroxide-mediated oxidation described by Brevett and Johnson. While they describe the adsorbed hydroxide as a radical, it is instructive to picture it as a normal hydroxide molecule bonded to the electrode surface; the 'bond' depicted is the binding interaction between the dangling radical and the electrode. The first step of the reaction is the anodic adsorption of a hydroxide ion. It is of course possible for this to occur with a H_2O molecule instead, ejecting H^+, and the abundance of water in an aqueous solution makes this a likely route. Once in this configuration, the oxygen of this 'activated hydroxide' is adjacent to the anodic electrode, the supreme electron withdrawing group. This means that even the very electronegative oxygen becomes deshielded, opening it up to nucleophilic attack. The next step is a simple nucleophilic substitution with the electrode serving as the leaving group.

This mechanism is attractive because it provides an explanation for the addition of oxygen to the oxidized species even in acidic conditions since the creation of the OH^- group involved is propelled by the electrode as the most powerful motivator in the system. It also involves the sequential as opposed to simultaneous transfer of electrons.

The reduction of highly oxidized species cannot be explained by the reverse of this same mechanism. A negatively charge electrode would repel negatively charged sulfur complexes,
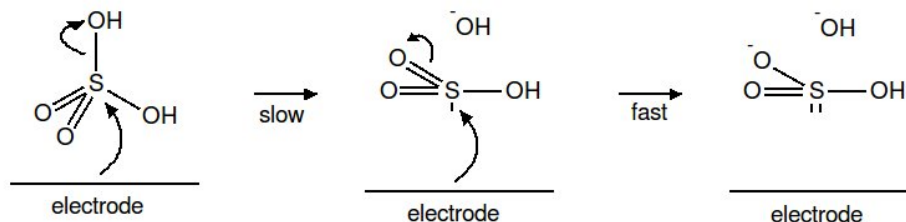
Figure 3.5: The proposed mechanism for the reduction of sulfate, which is analogous to the mechanism for the reduction of lower sulfoxides.

and would be extremely unlikely to donate electrons to the nucleophilic OH groups. Thus, it is necessary to look for a different reductive process.

Sulfate is reduced in nature by the aptly-named sulfur reducing bacteria, which use enzymatic processes to reduce the S(VI) first to S(IV) and then (by a debated mechanism) to S(-II), using sulfur as a terminal electron acceptor much the way aerobic organisms use oxygen [82]. Sulfate can also be reduced radiolytically, as is suspected to occur by agency of energetic electrons in the slow sulfur cycle on the icy surface of Jupiter's moon Europa [83]. Hot, concentrated sulfuric acid is also known to act as an oxidizing agent in the dissolution of metals in reactions such as

$$Cu + H_2SO_4 \rightarrow Cu^{2+} + SO_2 + 2\,OH^- \tag{3.1}$$
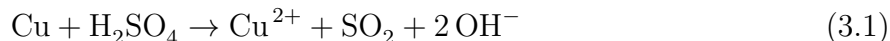
though less acidified sulfates will not perform this oxidation. Finally, some specialized clusters catalyze sulfate reduction by an unknown mechanism [84]. In short, despite its high oxidation state, sulfate in water will only be reduced by fairly extreme conditions. Along with other good supporting electrolytes such as NO_3^-, SO_4^{2-} is generally considered a non-electroactive species with regard to electrode reduction [85]. While direct sulfate determination with polarography is possible [86], the low rate of reaction of the sulfate makes this a poor method of analysis. Most other sulfur-containing oxide anions (or sulfur-containing acids), on the other hand, are very reactive and unstable [87], undergoing complex dissociation, disproportionation, and redox reactions with the same species, water, and other species in solution.

What this implies in our search for a reaction mechanism is that while it will be possible to reduce SO_4^{2-} at an electrode, the mechanism should involve an unlikely intermediate, implying a high activation energy of the reaction. This will slow the kinetics of the reaction enough that the current observed from the reduction will be undetectable on the background of the solvent reduction during most experiments, making the species essentially non-electroactive. The mechanism should, however, be applicable to the reduction of sulfur species at lower oxidation states, allowing them to be reduced more quickly.

A suggested mechanism of sulfate reduction at the electrode is shown in Figure 3.5. This
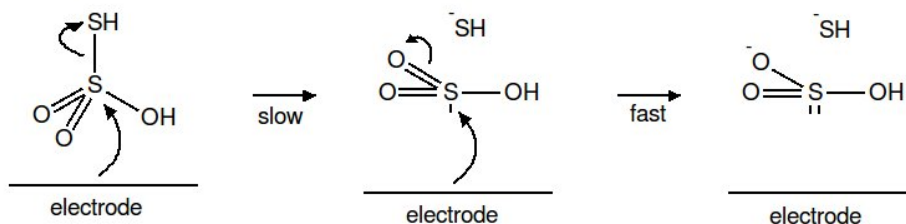
Figure 3.6: The proposed mechanism for the reduction of thiosulfate at the electrode surface.

mechanism has the features we require. The first step would be very slow to occur, first necessitating the formation of the neutral H_2SO_4 molecule in order to approach the very negatively charged electrode closely, and then overcome the steric hindrance imposed by the tetrahedrally positioned oxygen molecules preventing the close approach of the S atom. This explains the extremely low rate of reaction for sulfate itself. Lower oxyacids of sulfur have a lower acidity compared to H_2SO_4, allowing them to approach the electrode more readily. Additionally, the more reduced sulfur oxyacids will experience a great deal less steric hindrance when approaching the surface of the electrode thanks to the bending caused by the presence of a lone pair on the central sulfur atom. This explains the higher rates of reduction in the lower oxyacids.

This mechanism has interesting ramifications for the reduction of $S_2O_3^{2-}$ at the electrode. The most likely pathway for such a reduction is shown in Figure 3.6. The SH^- is a better leaving group than OH^- (the pK_a for the first hydrogen in H_2S is 6.88 [88]; the pK_a of water is 15.7) so we would expect it to be the species freed during the reaction. This means that the reduction of thiosulfate will result in the formation of one SO_3^{2-} molecule and one HS^- molecule. The presence of a free S(-II) species at the surface of the electrode following such a reduction has implications in the synthesis of the hydrogen sulfides, below.

Directly testing the validity of these proposed mechanisms is beyond the scope of this work. The analysis of Tafel slope plots could confirm the presence of sequential one-electron transfer events or the existence of a multi-electron transfer. The validity of the hypothesis that low pKa leads to slower electro-oxidation could be tested by a study of electrode current as a function of pH in solutions with a fixed solution conductivity. The role of steric hindrance in slowing the rate of reduction could be probed using surface spectroscopy techniques to examine the structure of the species interacting with the electrode.

With these reactions in hand, we now have an explanation for most of the reaction pathways depicted in Figure 3.1. The oxidative connections between species with a S-S bond were elucidated by Brevett and Johnson [6], and those between single sulfur species were extrapolated by analogy. One glaring missing link is the lack of a characterized sulfur species between SO_3^{2-} and the elemental S species. This gap is filled by a transient SO_2^{2-} species with S in the +2 oxidation state. Evidence for this structure of the species has been collected using XANES and FT-IR spectroscopy while observing the Ni(II) catalyzed oxidation of S^{2-}

in water [8]. The instability of this species, however, means that its presence is brief before undergoing subsequent oxidation or reduction.

We will now briefly touch on the remaining reaction pathways in Figure 3.1. The topmost reaction between SO_4^{2-} and $S_2O_7^{-4}$ (sometimes called oleum) is the hydration of disulfate to create sulfate, used in the contact process to remove H_2O from highly concentrated solutions of sulfuric acid [7]. Moving down the diagram, dithionate can be formed by the combination of sulfate and sulfur dioxide [7]. The reverse decomposition reaction only occurs in high concentrations of dithionic acid [79], and so is not indicated in the Figure 3.1. In the S(IV) section we see the interconversion of sulfur dioxide, sulfite, and disulfite, with each conversion consuming or releasing an oxygen atom (listed as H_2O, but in the form of OH^- in basic solutions) to solution [7, 79]. Dithionate reacts with water, producing thiosulfate and sulfite [79]. Many reactions of dithionate are explained by the interconversion of the species with the radical SO_2^-. [79] and this also provides another mechanism for the breaking of the S-S bond present in thiosulfate. Polythionate is known to react with thiosulfate and sulfite, increasing or decreasing the length of the S_x chain in the middle of the polythionate. Acidic solutions favor a decrease in chain length and the formation of thiosulfate, while basic solutions form sulfite and increase the length of the polythionate species [79]. Finally, at the lower end of the diagram, we see that disulfide can react with colloidal sulfur to form charged polysulfides in solution.

Now that we've got a reasonably complete idea of the major pathways of sulfur reaction in solution, we can make a few observations of relevance to our system of interest before performing our own experiments. First, the primary sulfur sink in the solution is colloidal sulfur. This species will not be attracted to a charged electrode, and will generally fail to interact with metal ions as they are reduced at the electrode. A secondary sink is sulfate. It is evident in Figure 3.5 that the sulfate reduction reaction has a high kinetic barrier, and once oxidized to this point it will be difficult to reduce the species. A final point worth noting is that even though thiosulfate starts disproportionating as soon as it it placed in the acidic solution, there are mechanisms for its reformation, so will not be irreversibly depleted from the deposition bath.

3.2 Electrochemistry of H_2SO_4 in Water

The effects of the supporting electrolyte of an electrochemical deposition bath are often underestimated. In an effort to control the number of variables being analyzed, the solutions of interest were often titrated to control their pH. This means, of course, that H_2SO_4 effectively becomes a supporting electrolyte in such a solution, and as such should be examined as a background solution constituent.

Figure 3.7 displays a CV of Millipore water which has been titrated to a pH of 2.50 using H_2SO_4. A simple thermodynamic analysis of the SO_4^{2-} system in water can be obtained using Medusa [2] and is displayed in Figure 3.8.
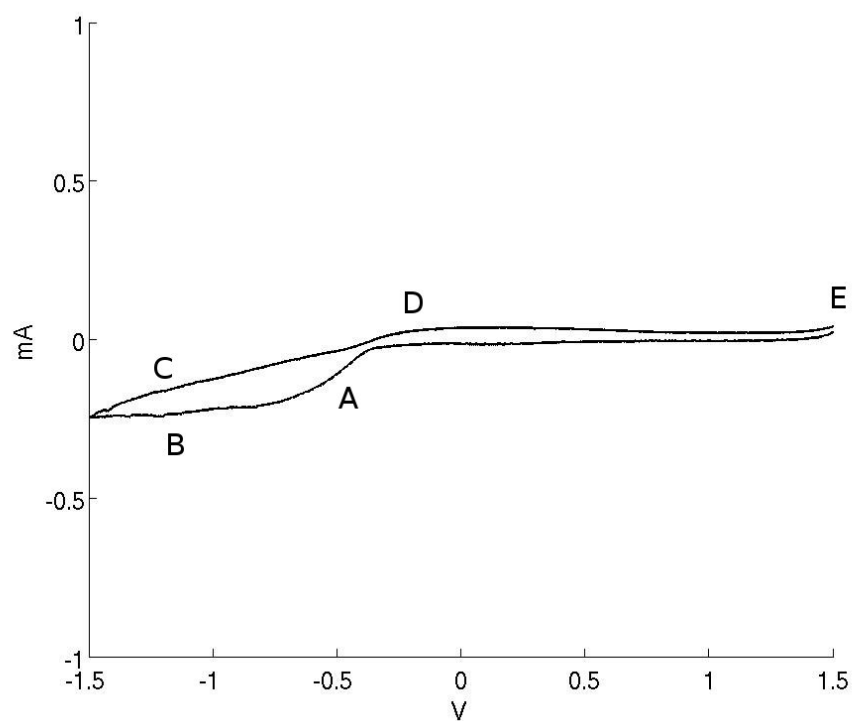
Figure 3.7: CV of H_2O titrated to pH 2.50 with H_2SO_4 (1.5 V / -1.5 V vs. Ag/AgCl, 50 mV / sec)
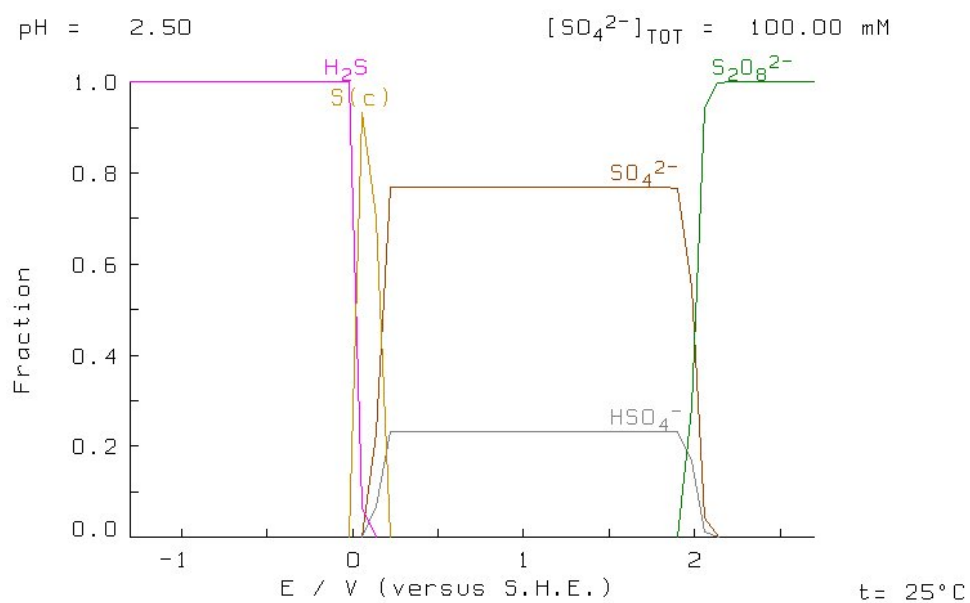
Figure 3.8: Speciation diagram of SO_4^{2-} in water at pH 2.5 created using Medusa [2].

By comparing Figures 3.7 and 3.8, being mindful of the fact that the Ag/AgCl reference electrode used to record Figure 3.7 is +209mV relative to NHE, we can assign a reaction from Figure 3.1 to each feature observed in Figure 3.7.

Peaks A and B in Figure 3.7 both exhibit a very small current, as is expected for the unreactive SO_4^{2-}. These featrues result from the subsequent reductions

$$SO_4^{2-} + 8\,H^+ + 6\,e^- \rightarrow S + 4\,H_2O \tag{3.2}$$

and

$$S + 2\,H^+ + 2\,e^- \rightarrow H_2S \tag{3.3}$$
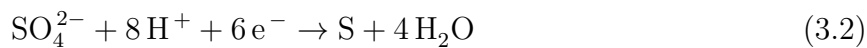
Reaction 3.2 actually occurs through sequential reductions using the mechanism described in Figure 3.5, but the first reaction is the rate limiting step due to the hindrances involved in the electrode gaining access to the central sulfur atom. After this step occurs, there is plenty of potential at the electrode to complete the reduction to S^0. Reaction 3.3 will only occur immediately after reaction 3.2, assuming the electrical potential is great enough. Otherwise, the S^0 will aggregate into colloidal sulfur (S_6 or S_8) as seen in Figure 3.1 and become much more inert as well as diffusing away from the electrode. Thus, this

$$SO_4^{2-} + 10\,H^+ + 8\,e^- \rightarrow H_2S + 4\,H_2O \tag{3.4}$$
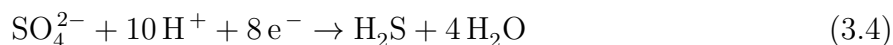
is a more appropriate way of describing the continuing reaction after the S^0 preconcentrated over the course of feature A is consumed, forming feature B. The "peak" labeled C is simply the slowing of the H^+ reduction as potential is increased. Peak D is the reverse of Reaction 3.2 (and 3.4, if any S^0 remains available at the electrode surface). Finally, peak E, just visible at the entreme end of the sweep, is the edge of the solution window – the point at which the solvent begins to oxidize. This allows us to assign to it the reaction

$$H_2O \rightarrow O_2 + 2\,e^- + 2\,H^+ \tag{3.5}$$

This lets us determine the solvent window for electrochemical explorations in this solvent system at about 1.5 V to -1.5 V relative to Ag/AgCl.

Feature Label	Reaction
A	SO_4^{2-}, $S_2O_6^{2-} \to S$ $S_2O_3^{2-} \to S^{2-} + SO_3^{2-}$
B	$S \to S^{2-}$
C	H_2O reduction
D	$H_2S \to S$
E	$S_2O_3^{2-} \to SO_4^{2-} + S_2O_6^{2-}$ $SO_3^{2-} \to SO_4^{2-}$
F	H_2O oxidation

Table 3.1: Reaction assignments for features in the CV of aqueous $Na_2S_2O_3$ solution displayed in Figure 3.9.

3.3 Electrochemistry and pH Dependence of $Na_2S_2O_3$ in Water

Even before a potential is applied at the electrode, $S_2O_3^{2-}$ is undergoing the reactions in solution described above and seen in Figure 3.1.

Figure 3.9 displays a cyclic voltammogram of 100 mM $Na_2S_2O_3$, titrated to pH 2.53 using sulfuric acid. Due to their situations and high currents, peaks F and C can be assigned to the solvent reactions

$$2\,H_2O \rightleftharpoons O_2 + 2\,e^- + 2\,H^+ \tag{3.6}$$

$$2\,H_2O + 2\,e^- \rightleftharpoons H_2 + 2\,OH^- \tag{3.7}$$

Peak E is the most notable feature of this voltammogram, and is characteristic of all cyclic voltammograms of solutions containing $S_2O_3^{2-}$. It is also notably absent in our background solution containing SO_4^{2-}. This means peak E is an oxidation of $S_2O_3^{2-}$. The electro-oxidation mechanism of thiosulfate is shown in Figure 3.4, and will proceed along the pathway labeled with A from thiosulfate up to dithionate and disulfate. In aqueous solution the majority of disulfate formed will immediately hydrolyze into sulfate. Brevett *et al.* note that in the case of a one step potential, dithionate is the primary product of thiosulfate oxidation, while in the case of a potential which is held for a time at an intermediate range, quantitative oxidation to sulfate can be achieved [6]. In our system, the ramping potential will produce both dithionate and sulfate by way of a number of intermediates, so we assign feature E the reactions

$$S_2O_3^{2-} + 5\,H_2O \to 2\,SO_4^{2-} + 8\,e^- + 10\,H^+ \tag{3.8}$$
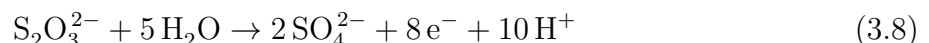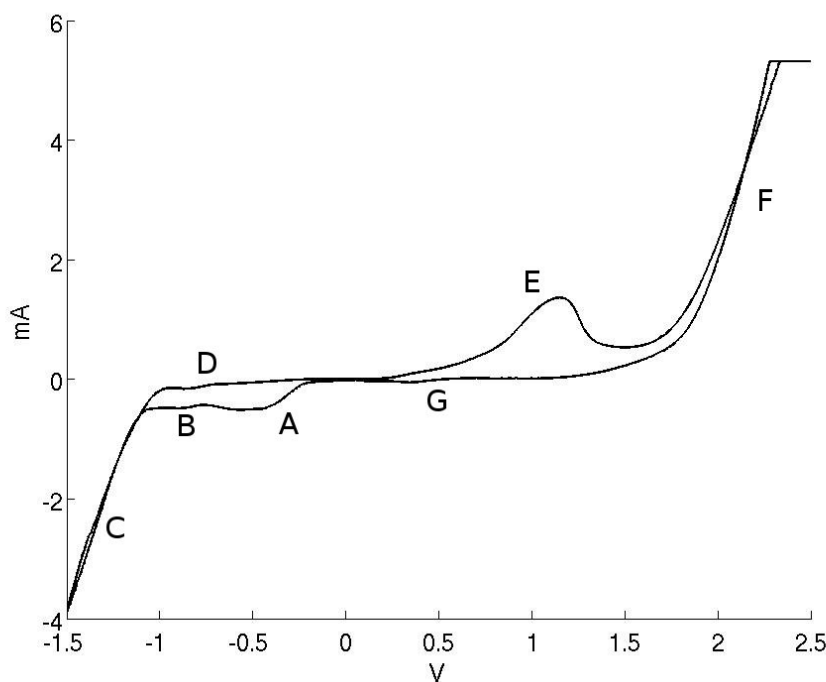
Figure 3.9: CV of 100 mM Na$_2$S$_2$O$_3$, titrated to pH 2.53 (2.5 V / -1.5 V vs. Ag/AgCl, 50 mV / sec)

and

$$S_2O_3^{2-} + 3\,H_2O \rightarrow S_2O_6^{2-} + 6\,e^- + 6\,H^+ \tag{3.9}$$
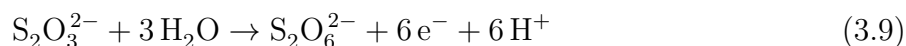
The stoichiometry of these reactions is likely to favor the production of dithionate in acidic solution due to the lower production of H$^+$ in Reaction 3.9. However, SO$_4^{2-}$ is still produced oxidatively at this point by the reaction

$$SO_3^{2-} + H_2O \rightarrow SO_4^{2-} + 2\,e^- + 2\,H^+ \tag{3.10}$$
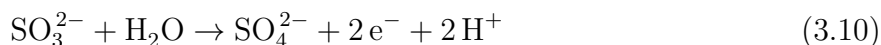
which consumes sulfite produced by the autodissociation reaction of thiosulfate in acidic media.

As we would expect based on our analysis of the reduction mechanism which holds for both SO$_4^{2-}$ and S$_2$O$_6^{2-}$, we do not see a reductive wave to match the oxidative wave in feature E. Feature G is merely the cessation of the oxidation of S$_2$O$_3^{2-}$ as the applied oxidative potential at the electrode becomes too small to overcome the activation energy of the first step in both Reaction 3.8 or Reaction 3.9.

The only reductive waves that we do see (apart, naturally, from the solvent reduction) are

features A and B. These correspond closely with the potentials of features A and B in Figure 3.7, and we can in fact assign some part of their current to the same reactions, the sequential reduction of sulfate in Reactions 3.2 and 3.3. The sulfate present in these reactions comes from Reactions 3.8 and 3.11, which will be artificially concentrated near the electrode. Features A and B will also incorporate current arising from the reduction of dithionate and thiosulfate. Due to the similar mechanisms of reduction which require similarly formed activated intermediates, it should not be surprising that the features overlap. Of particular note is the reduction of thiosulfate, which occurs by the reaction

$$S_2O_3^{2-} + 2\,e^- \rightarrow SO_3^{2-} + S^{2-} \tag{3.11}$$

as seen in the mechanism in Figure 3.6. At this point the S^{2-} produced could be immediately oxidized, producing a reversed current which could account for the flat shape of feature A. Feature B occurs once the reductive potential is strong enough to reduce adsorbed S^0 all the way to S^{2-} (or to cause the S^{2-} produced at the electrode by thiosulfate reduction to be stable at the applied potential). The last feature, peak D, corresponds to the reverse of Reaction 3.3, just as does peak D in Figure 3.7.

An analysis of the pH dependence of these reactions can be instructive in that it can help to elucidate the mechanisms of reaction. Figure 3.10 displays a series of cyclic voltammograms of 100 mM $Na_2S_2O_3$ titrated to various pH values by the addition of H_2SO_4. Colors indicate different pH values. There are two interesting features revealed by this plot. First and most noticeable is that there is not a steady trend of increasing or decreasing current in the peak with increasing pH. The current increases until about pH 2.5, then decreases until pH's around 4 before increasing to the highest current observed. The second feature is most obvious in the green plot of Figure 3.10 (pH 4.11). Two peaks, one smaller with its peak at 0.58 V and the other large peak at 0.98 V, are visible.

These features can be explained using the oxidative mechanism displayed in Figure 3.4 combined with the complex interaction of sulfur species with themselves and acidic or basic solutions displayed in Figure 3.1, specifically the acid-catalyzed thiosulfate disproportionation of Figure 3.2. First, the sequential oxidation mechanism accounts for the presence of multiple peaks on the CV. Although two are clearly visible, the second, broader peak is likely the composite of multiple peaks corresponding to the multiple stages of the reactions.

The trend of the first two CV's (red and orange, at pH 2.02 and 2.53, respectively) is what we would expect from an analysis of our oxidation mechanism. The need for an activated OH^- group at the surface of the electrode means that the rate of this reaction will be inhibited by a lower pH. The fact that these species will be artificially concentrated at the surface of the electrode due to migration effects will offset this trend somewhat. At a pH of 3, however, the current associated with this peak has decreased from a temporary maximum at around 2.5, and by a pH of around 4 it has reached its minimum. This is due to the pH dependent thiosulfate decomposition.
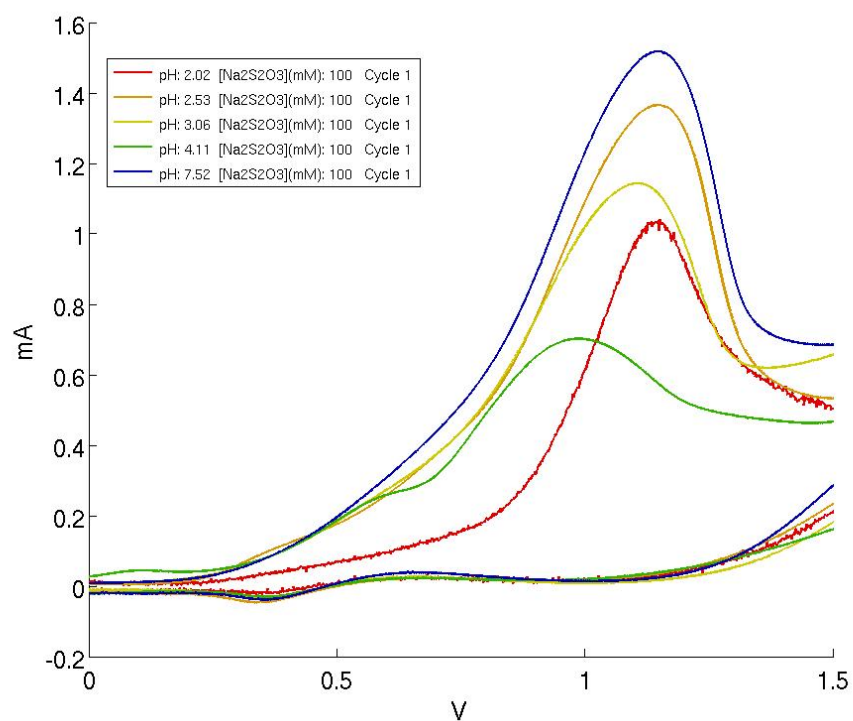
Figure 3.10: Multiple CV's of 100 mM $Na_2S_2O_3$ solutions, titrated to various pH values with H_2SO_4 (1.5 V / 0 V vs. Ag/AgCl, 50 mV / sec)

As the pH of the solution increases, less of the thiosulfate present originally will decompose. The decomposition results in primarily SO_3^{2-} and colloidal sulfur, with any S^{2-} and poly-thionates produced being the result of the much less likely side reaction. Colloidal sulfur is very unreactive at the electrode. With this in mind, referencing Figure 3.2 we see that the thiosulfate decomposition can be thought of as replacing every molecule of thiosulfate decomposed with a molecule of SO_3^{2-}. There are a number of reasons that we would expect the oxidation of sulfite to occur more quickly at the electrode than that of thiosulfate. First, sulfite is smaller and so is capable of diffusing more quickly to the electrode. Secondly, the oxidation of sulfite results in the very stable sulfate ion, as opposed to thiosulfate, the first oxidation step of which results in a very unstable species.

These two pH-dependent factors explain the observed data. At very low pH, a larger proportion of the thiosulfate in the system has decomposed to sulfite, which should increase the electrode current. However, the low pH decreases the amount of activated OH^- at the surface of the electrode, and this limits the rate of reaction. As the pH increases, the current is increased due to the larger number of OH^- sites on the electrode, but is decreased due to the fact that more of the thiosulfate remains undissociated. The current passes through a minimum during which there is a significant proportion of thiosulfate remaining in solution and the increased amount of OH^- cannot make up for the slower rate of thiosulfate reaction. By the time we get to more neutral pH's, the thiosulfate concentration is as high as it will get since at these pH values the dissociation is negligible. The increase in OH^- concentration allows the production of more active sites on the electrode surface, increasing the current to its highest point.

A final piece of evidence for this interpretation can be found in the peak shapes of the low pH CV's versus those taken at higher pH's. While all of the features begin to grow at about 0.2 V, the features of lower pH solutions show a much sharper increase at higher voltages, resulting in the actual peaks of the features being situated at more anodic voltages. This is especially noticeable in the red pH 2 plot, which increases moderately until around 0.7 V, at which point it slopes much more steeply anodic. This is due to the fact that we are observing a combination of reactions. The current at lower voltages is due to the oxidation of the thiosulfate sulfur atoms with a low oxidation state, while the current at higher voltages is due to the oxidation of sulfur atoms in higher oxidation states, such as sulfite or the two-sulfur species formed by successive oxidation of thiosulfate. The low current at the lower voltages is due to the relatively slower reaction rate of thiosulfate.

The pH dependence of the reductive waves shown in Figure 3.11 can be explained with similar reasoning. There is a steady decrease in current of this reductive peak with increasing pH, with the basic pH providing an anomalous increase in current. The decreasing current can be explained by the stabilization of the products by the presence of H^+ in solution. This peak corresponds to the reduction of sulfates with sulfur in high oxidation states to $S(0)$, which is not particularly stabilized by acid. This reduction also releases a number of OH^- ions into solution, a process aided by acidic solution. The aberrant behavior of the high pH CV is explained by the fact that at these pH values it is primarily thiosulfate being reduced rather than sulfate or sulfite, and the less stable reactant will decrease the activation energy
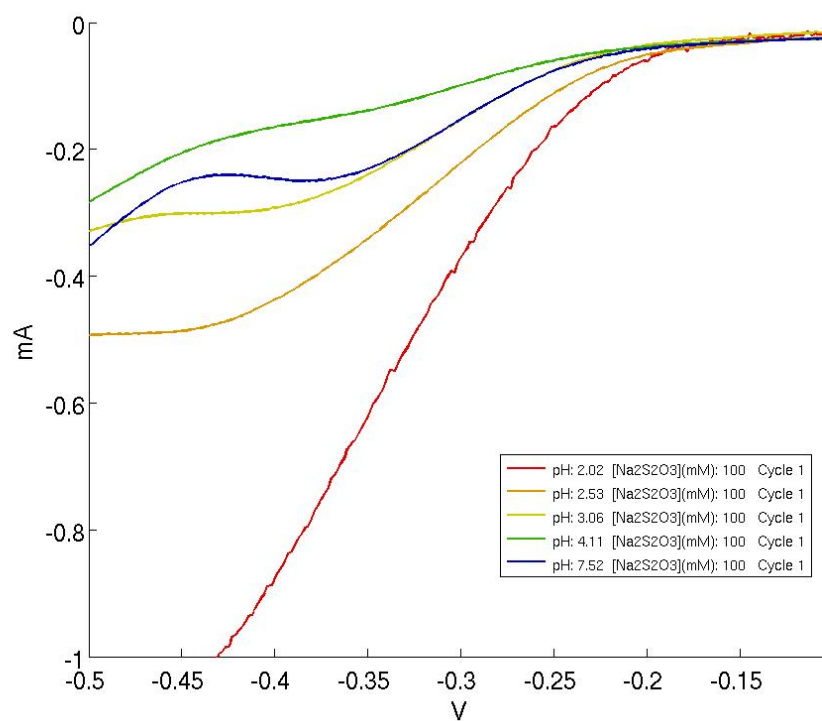
Figure 3.11: Multiple CV's of 100 mM Na$_2$S$_2$O$_3$ solutions, titrated to various pH values with H$_2$SO$_4$. Only the reductive waves are shown in this plot. (-0.1 V / -0.5 V vs. Ag/AgCl, 50 mV / sec)

of the reaction, allowing higher currents.

3.4   Conclusions

This chapter introduced the complex solution chemistry of thiosulfate. These solution effects will have direct bearing on the analysis of metal sulfide deposition baths in the chapters to follow. It is important to note that any solution of thiosulfate, especially one with lower pH, will contain a significant amount of SO_3^{2-} as well as S_8, S^{2-} and assorted polythionates. This situation becomes even more pronounced when the solutions are perturbed by an electrode potential. The mechanisms by which thiosulfate and its descendants are oxidized and reduced at the electrode have been discussed, and will have a bearing on the electrode mechanisms of species in the subsequent chapters.

Chapter 4

Electrochemistry of Aqueous FeSO$_4$ and Na$_2$S$_2$O$_3$

An electrochemical study of the FeSO$_4$–Na$_2$S$_2$O$_3$ system is desirable for a number of reasons. The anodic properties of this system are of interest in understanding iron and steel corrosion in media containing sulfur compounds [89]. The leaching of iron sulfides is also a commercially important process for metal recovery [90]. Our primary reason for this investigation is to gain a fundamental understanding of the cathodic properties of the system toward the synthesis of iron sulfides for semiconductor applications.

4.1 Electrochemistry and pH Dependence of FeSO$_4$ in Water

Since the electrochemistry of both H$_2$SO$_4$ and Na$_2$S$_2$O$_3$ have been covered in Chapter 3, this chapter will start with an exploration of the electrochemistry of FeSO$_4$. As always, a good place to start an electrochemical analysis is with thermodynamic calculations of the species that will be present in solution. Figure 4.1 displays a Pourbaix digram calculated using Medusa [2]. The most important feature to note for our purposes is the large domain of stability for FeS$_2$, our desired product. Additionally, it is evident that the chemical intuition indicating that the deposition solution should be acidic is correct, as the domain where the formation of Fe$_2$O$_3$ precipitate is thermodynamically most favorable is much smaller in the more acidic regions of the Pourbaix. Finally, it is evident that since both Fe(III) and Fe(II) species are stable in solution, we should observe a solution reduction peak. At pH 3.5 this will be around 0.4 V vs. Ag / AgCl.

Figure 4.2 displays the first cycle from a CV of 60 mM FeSO$_4$ and 100 mM Na$_2$S$_2$O$_3$.

Feature A in Figure 4.2 is a combination of the solution window and charging current with the
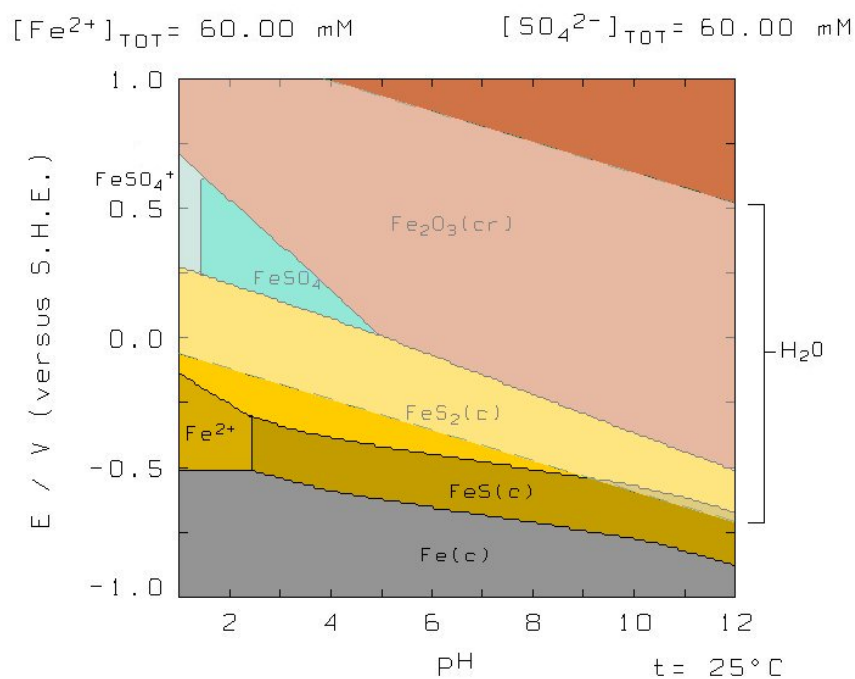
Figure 4.1: Pourbaix diagram for a system with 60 mM in aqueous Fe species and 60 mM in aqueous S species at 25º C, created using Medusa [2].
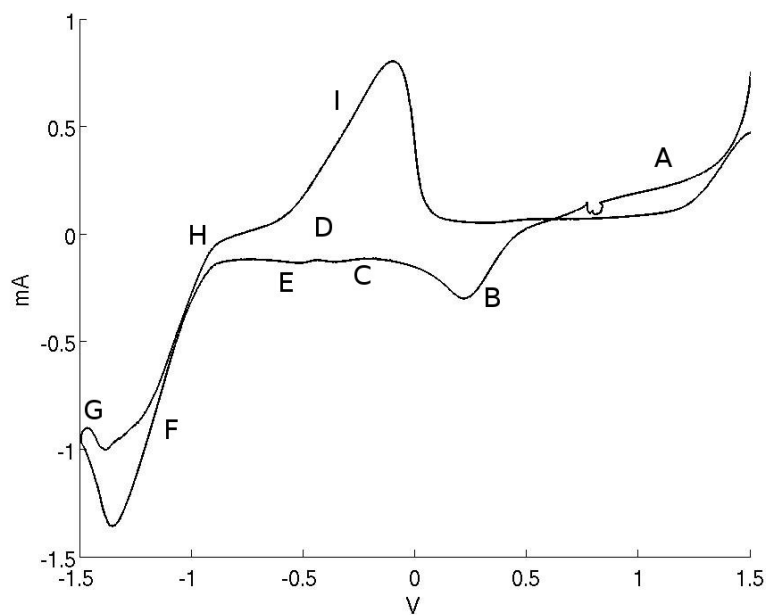
Figure 4.2: First cycle from a CV of 60 mM $FeSO_4$ at its untitrated pH of 3.47 (1.5 V / -1.5 V vs. Ag / AgCl, 50 mV / sec)
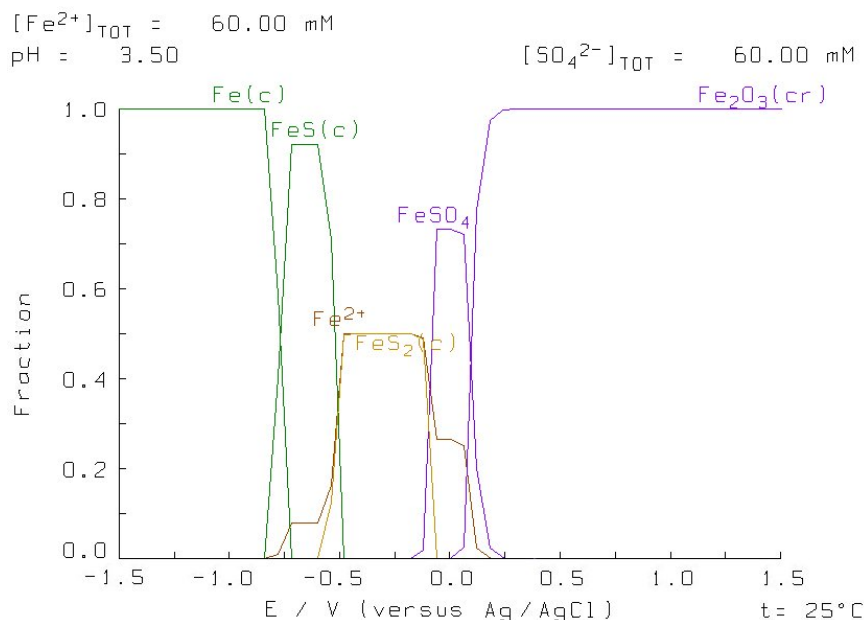
Figure 4.3: Speciation diagram for Fe of 60 mM $FeSO_4$ in water at pH 3.5 created using Medusa [2].

oxidation of the Fe^{2+} present in solution. Feature B is the reduction of the Fe^{3+} formed at the electrode in A. The thermodynamic data seen in Figure 4.3 support this assignment. The thermodynamically stable species at this potential, Fe_2O_3, has kinetic barriers to formation which will not be overcome at room temperature in the timescale of these experiments. In this system, the oxidation of Fe^{2+} will result in the production of lower-stability iron (III) oxides such as $Fe(OH)_3$ and $FeO(OH)$ [7]. The lower stability of the species present in solution means that the reduction of these Fe(III) species can occur at less reductive potentials. The onset of reduction to Fe(II) will shift up from the 250 mV threshold seen in Figure 4.3 to the 500 mV threshold of feature B in Figure 4.2. The exact position of this peak is also affected by the presence of complexing sulfate in solution, and agrees well with that observed in the literature [91].

The onset of feature C corresponds well with the reduction of SO_4^{2-} to S_2^{2-}, observed in Figure 4.3 at -100 mV, and similarly, the onset of feature E agrees with the reduction of S_2^{2-} to S^{2-}, observed in the thermodynamic calculations at -475 mV. Feature D is not present during the first cycle.

The visible onset of metal reduction on the surface of the electrode makes it clear that feature F is due to the plating of Fe onto the electrode surface. However, the onset of feature F is at about -900 mV. The thermodynamic calculations in Figure 4.3 show that the onset of the reduction of Fe(II) to Fe should begin at around -725 mV. An onset at such reductive potentials is observed regularly in the literature [92] [93], and is due to the slow kinetics of reaction at less reductive potentials. Fe is indeed being reduced at the surface of the electrode, but it does so by a pathway with such a slow rate limiting step that there is negligible perturbation of the I / V curve.

Díaz *et al.* [92] have performed an extensive analysis of the Fe electrodeposition mechanism using impedance spectroscopy. Discounting the high frequency capacitive loop present in every data set due to the double-layer capacitance, three features can be observed in their impedance measurements at potentials reducing enough to produce high currents. This indicates that at least three adsorbed species are present (one for each characteristic frequency observed in the capacitive or inductive loops.) Based on the behavior of these three features with changing bias and pH, they propose these three interrelated pathways towards Fe plating:

$$\text{Fe(II)} \rightarrow \text{Fe(I)}_{\text{ads}} \rightarrow \text{Fe} \tag{4.1}$$

$$\text{Fe(II)} \rightarrow \text{Fe(I)}_{\text{ads}} \leftrightharpoons \text{Fe(I)}_{\text{ads}}^* \rightarrow \text{Fe} \tag{4.2}$$

$$\text{Fe(II)} \rightarrow \text{Fe(I)}_{\text{ads}} \leftrightharpoons \text{Fe(I)}_{\text{ads}}^{**} \rightarrow \text{Fe} \tag{4.3}$$
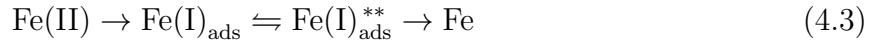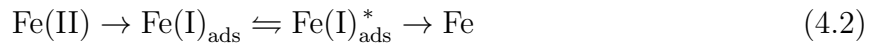
The beginning of each pathway is the reaction

$$\text{Fe(II)} + \text{e}^- \xrightarrow{K_1} \text{Fe(I)}_{\text{ads}} \tag{4.4}$$

This reaction is simple enough to understand. Fe(II) from solution (likely complexed by SO_4^{2-}) receives an electron from the electrode, reducing to an adsorbed Fe(I). The second half of Pathway 4.1 is simply

$$\text{Fe(I)}_{\text{ads}} + \text{e}^- \xrightarrow{K_2} \text{Fe} \tag{4.5}$$
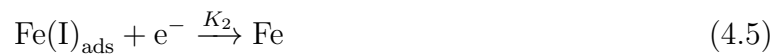
in which the adsorbed Fe(I) receives a second electron from the electrode, reducing to Fe metal. This is a classic Volmer-Heyrovksy mechanism [94].

Pathway 4.2 is a bit more complex. The first step of the pathway is Reaction 4.4. The following steps are

$$\text{Fe(I)}_{\text{ads}} + \text{H}_2\text{O} \underset{K_{-3}}{\overset{K_3}{\rightleftharpoons}} \text{Fe(I)}_{\text{ads}}^* + \text{H}^+ \tag{4.6}$$

and

$$\text{Fe(I)}_{\text{ads}}^* + \text{Fe(II)} + 2\,\text{e}^- \xrightarrow{K_4} \text{Fe(I)}_{\text{ads}}^* + \text{Fe} \tag{4.7}$$
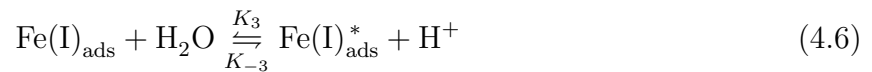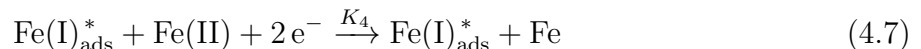
The mechanism of Pathway 4.3 is taken as the same as Pathway 4.2, though naturally with a different intermediate:

$$Fe(I)_{ads} + H_2O \underset{K_{-5}}{\overset{K_5}{\rightleftharpoons}} Fe(I)_{ads}^{**} + H^+ \qquad (4.8)$$

and

$$Fe(I)_{ads}^{**} + Fe(II) + 2\,e^- \xrightarrow{K_6} Fe(I)_{ads}^{**} + Fe \qquad (4.9)$$
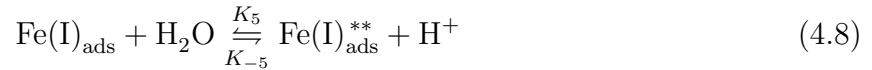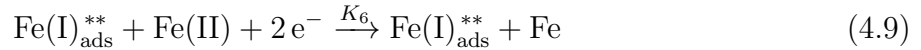
The differences between the two intermediates are first, that the formation of $Fe(I)_{ads}^{*}$ from $Fe(I)_{ads}$ starts at a lower potential on the electrode surface and second, that the $Fe(I)_{ads}^{*}$ species does not catalyze the production of H_2, while $Fe(I)_{ads}^{**}$ does. Both species consume $Fe(I)_{ads}$ and naturally occupy sites on the electrode that otherwise would be available to other adsorbate species.

If we consider this mechanism for the deposition accurate, it provides an explanation for the shift in deposition potential observed in Figure 4.2. Let us consider the rates of the reactions. K_1 very quickly ceases to be the limiting [93], so the reduction rates of the adsorbed species must necessarily be slower. Díaz et al. find that Pathway 4.2 begins to occur at cathodic polarizations greater than that required for 4.1 but less than the -900 mV polarization observed as the onset of the peak in Figure 4.2. Pathway 4.3, on the other hand, is only present at polarizations for which high current is observed. This implies that both K_2 and K_4 are fairly slow, while K_6 is fast enough to produce the high current seen in Figure 4.2. This makes intuitive chemical sense, as K_6 being high would imply a low activation energy, which would arise more easily from a less stable $Fe(I)_{ads}^{**}$ intermediate. Such an intermediate would only be formed if there were a high enough overpotential at the electrode to overcome the activation energy to move it up that far on the energy landscape.

The actual identity of the $Fe(I)_{ads}^{*}$ and $Fe(I)_{ads}^{**}$ intermediates is unknown, though the gross positive correlation of pH with their reaction rates implies that they are likely to incorporate OH^- groups in some manner.

Feature F reaches a peak and finally decreases once the concentration of Fe(II) at the electrode is depleted enough that K_1 limits the overall rate of reaction. It should be noted that during this feature as well as C, D, and E, H^+ reduction is also occuring. Díaz *et al.* have performed non-intrusive pH measurements at the electrode surface during the course of Fe deposition and established that the pH is raised locally, indicating H^+ reduction at the surface [44]. During the earlier reactions, the anodic current observed is primarily due to H^+; the prevalent Fe reduction mechanisms at less cathodic potentials have low efficiency. The efficiency of the K_6 reaction is, however, higher, giving rise to the more prounounced feature F. The peak of feature F does not return to a current of 0 due to the large amount of cathodic current being produced by overpotential H^+ reduction in this region. If the switching potential of the experiment is set more anodically, the characteristic sharp drop
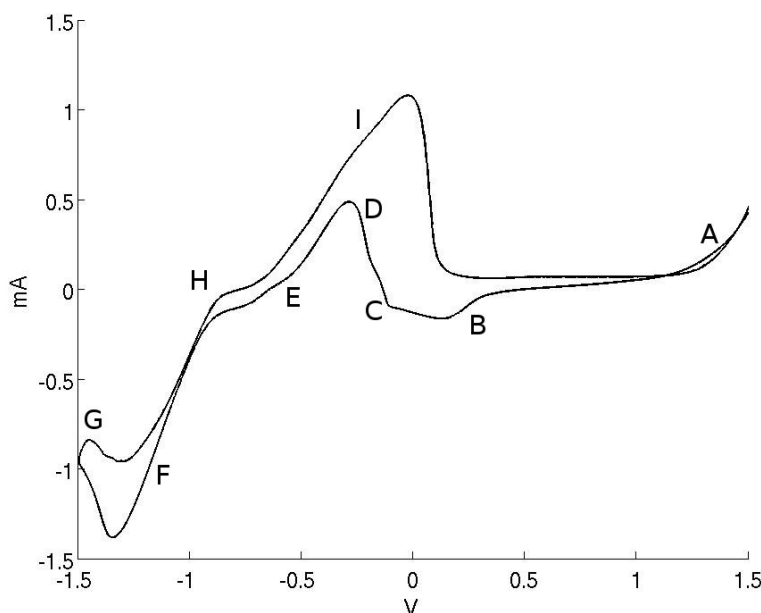
Figure 4.4: Second cycle from a CV of 60mM FeSO$_4$ at its untitrated pH of 3.47 (1.5 V / -1.5 V vs. Ag / AgCl, 50 mV / sec)

off of H$^+$ is more clear, and at such anodic potentials it is possible to visibly see H$_2$ bubbling violently from the electrode surface, often displacing masses of deposited material.

Feature G is the tail from the peak at F plus a charging artifact. Feature H is simply the leveling off of the reduction from feature F as the potential becomes less cathodic and the formation of Fe is driven less quickly. Feature I is the dissolution of plated Fe by the reverse of Process 4.1. This peak feature displays the sharp slope to the anodic side characteristic of stripping peaks due to the preconcentration inherent in plating reactions. On some cycles an eye full of hope and confidence will catch the oxidation wave corresponding to the reverse of the reduction in feature B. The reason for the nearly imperceptible current of this feature is likely due to the instability of the intermediate adsorbed species required to undergo the oxidation without significant overpotential. In CV's of FeSO$_4$ in more acidic media this oxidation feature is present (*e.g.* Figure 4.7), implying that the intermediate is destabilized by the presence of OH$^-$ in solution. Thus, it would make sense if the Fe(II) to Fe(III) oxidation at the electrode occurs according to the reaction

$$\text{Fe}^{2+} \rightarrow \text{Fe}^{3+} + \text{e}^- \tag{4.10}$$

while being inhibited by the formation of Fe(OH)$^+$ and other hydroxide complexes.

The second cycle of the cyclic voltammogram, seen in Figure 4.4 differs remarkably in one respect from the first. At around -100 mV, feature D appears. As the potential at the electrode becomes more reducing, the current incredibly runs opposite the direction of the
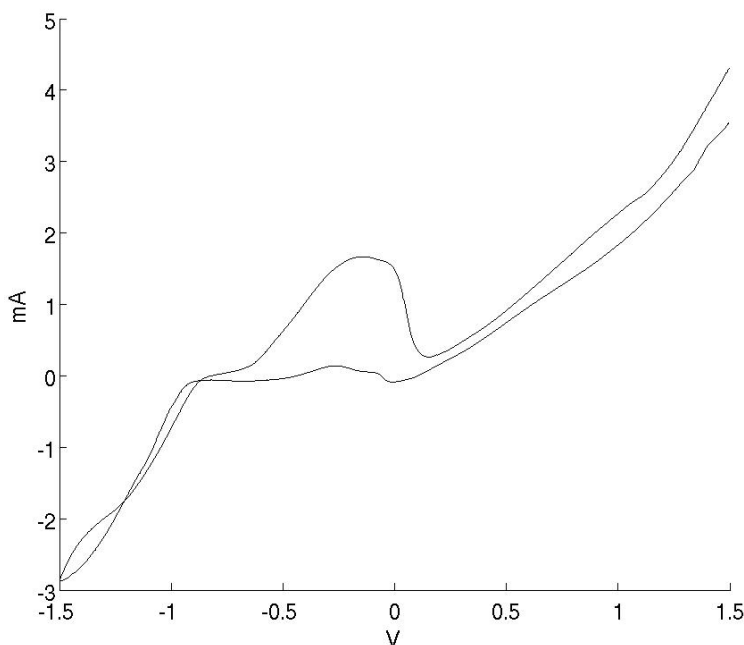
Figure 4.5: First (solid line) and second (dotted line) cycles from a CV of 60 mM FesO$_4$ at its untitrated pH of 3.47 using a working electrode of 99.9% pure iron (1.5 V / -1.5 V vs. Ag / AgCl, 50 mV / sec)

applied potential for a time.

The best explanation for the puzzling behavior of feature D is that this feature is due to an oxidative reaction that only occurs in the presence of a reduced species. The presence of feature D in the second and subsequent cycles but not the first is telling. While a bare platinum electrode will not exhibit feature D, an electrode that has been modified by one cycle of Fe deposition does. This implies that a layer of Fe still present on the electrode after the oxidation wave participates in the reaction. It is possible that a feature such as D could be formed by a background anodic reaction which is inhibited by the electrode surface or compensated for by cathodic reactions at more anodic currents. However, the lack of anodic current at potentials anywhere close to those observed for feature D in CV's of aqueous H$_2$SO$_4$ using the same Pt electrode indicates that this is an unlikely explanation, and so another must be sought.

An analysis of the peak areas of feature I (the oxidation of Fe) and feature F (the reduction to Fe) reveals that the latter is three times as large. This is a necessary but not sufficient condition to confirm that there remains Fe on the surface of the electrode, because some current present in feature F is due to hydrogen reduction. However, at the end of a series of cyclic voltammograms, the platinum surface is observed to be obscured by reduced metal, indicating that this surface modification is happening even during the early cycles.

The hypothesis that this oxidative phenomenon occurs when an iron surface is exposed to a
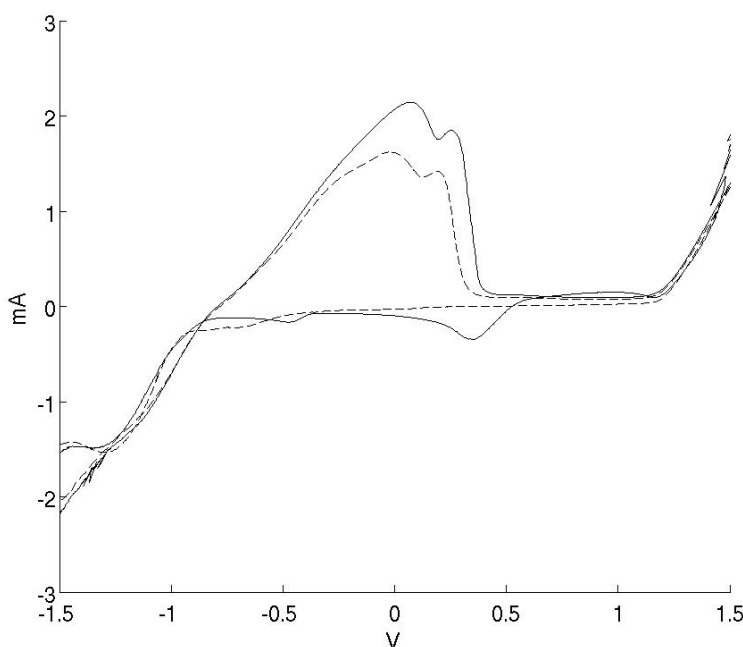
Figure 4.6: First (solid line) and second (dotted line) cycles from a CV of 60 mM FeCl$_2$ at its untitrated pH of 2.91 (1.5 V / -1.5 V vs. Ag / AgCl, 50 mV / sec)

reducing current in the FeSO$_4$ solution was tested by running a similar CV in an identical solution using a piece of pure iron as the working electrode. Figure 4.5 displays the first cycle of this voltammogram. A similar oxidative feature is observed. The lower magnitude of this feature compared to that present in Figure 4.4 can be accounted for by the smoothness and lower number of reactive sites of the prepared metal electrode compared to the film of haphazardly deposited iron present on the surface of a cycled platinum electrode.

To determine the other participant in the reaction, analogous cyclic voltammograms of a solution of 60 mM FeCl$_2$ were run. An example of these data is displayed in Figure 4.6. These voltammograms exhibited analogous peaks for all iron peaks in the run, but did not display feature D, indicating that sulfur species as well as Fe are involved in the anomalous reaction.

With reference to the thermodynamic data presented in Figure 4.3, we can determine a system which could satisfy the observed data. The onset of feature D is in the potential region that sulfur is converting between S$_2^{2-}$ and S^{2-}. The balanced reaction for this conversion is

$$S_2^{2-} + 2\,e^- \rightarrow 2\,S^{2-} \tag{4.11}$$

The S^{2-} is, of course, formed immediately adjacent to the electrode, meaning that it can

react quickly with whatever species is on the electrode. Fe converts to FeS by the reaction

$$Fe + S^{2-} \rightarrow FeS + 2\,e^-\tag{4.12}$$

If we combine these two processes, the balanced equation is

$$2\,Fe + S_2^{2-} + 2\,e^- \rightarrow 2\,FeS + 4\,e^-\tag{4.13}$$
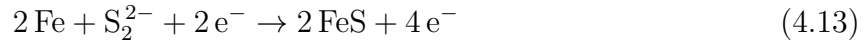
Thus, there is an input of two electrons, which requires a polarization of the electrode below a particular reductive threshold, but an output of four electrons, which would result in the strange oxidative wave observed in feature D.

The creation of FeS at iron surfaces exposed to S^{2-} in both acidic and basic solutions is well established in the iron corrosion literature [95, 96, 97, 89, 98]. In neutral and basic solutions in which a native oxide forms on the surface of exposed iron, the affinity of the sulfide is so strong that it will displace the oxides. The competitive surface adsorption occurs as

$$Fe-OH_{ads}^- + HS^- \rightleftharpoons Fe-HS_{ads}^- + OH^-\tag{4.14}$$
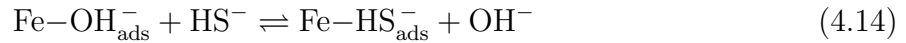
with equilibrium being pushed to the right by a range of pH which is sufficiently acidic to allow the production of OH^- and sufficiently basic to allow the presence of significant concentrations of HS^- rather than H_2S [95, 96]. If this equilibrium sufficiently favors the right side, oxidation of the iron will produce sulfides rather than hydroxides, as

$$Fe + HS_{ads}^- \rightleftharpoons FeHS_{ads}^-\tag{4.15}$$

$$FeHS_{ads}^- \rightleftharpoons FeHS_{ads}^+ + 2\,e^-\tag{4.16}$$

$$FeHS_{ads}^+ \rightarrow Fe(II)-S_{1-x} + xHS^- + (1-x)H^+\tag{4.17}$$
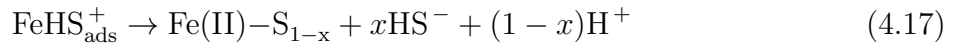
the final reaction of which forms predominantly FeS. Hasson *et al.* used *in situ* Raman as well as *ex situ* XRD and EDX techniques to establish the presence of FeS specifically on the surface of pure iron treated with Na_2S in basic conditions [96].

The assignment of this mechanism to feature D is supported by the pH dependence. Figure 4.7 displays a CV of a solution of 60 mM $FeSO_4$ titrated with H_2SO_4 to pH 2.33. Feature D is clearly absent from this voltammogram. At a lower pH, the production of H^+ necessitated by the final equation becomes untenable. Another way to state this thermodynamic situation
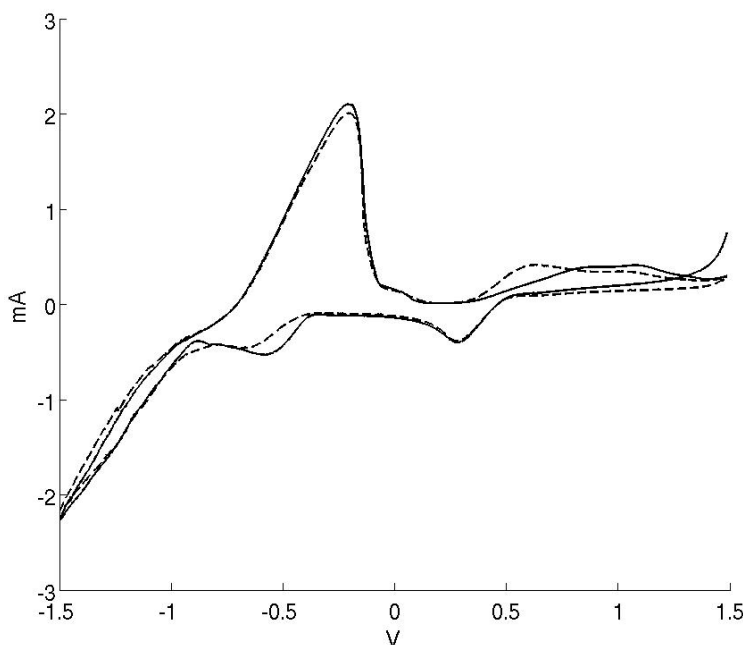
Figure 4.7: First (solid line) and second (dotted line) cycles from a CV of 60 mM FeSO$_4$ titrated to a pH of 2.33 (1.5 V / -1.5 V vs. Ag / AgCl, 50 mV / sec)

is that H$_2$S becomes much more stable at pH values that are this low (this makes FeS appreciably soluble in this region [99]), making reaction 4.15 unlikely. The lower K value of this reaction means that the formation of FeS from Fe and S^{2-} will not be able to drive the observed current reversal; after the adsorption step, the series of reactions will stop.

Further evidence for the validity of this peak assignment is gathered by examining the peak areas of feature I in Figures 4.2 and 4.4. The peak area of feature I in the second cycle is larger than that of feature I in the first cycle by an amount almost exactly equal to the area under feature D in the second cycle. This lends credence to the idea that the oxidative current observed in feature D is due to the creation of a reduced, solid species which is subsequently oxidatively stripped from the electrode. A comparison of the shapes of the two peaks allows us to reasonably state that the stripping of FeS occurs at a less oxidative polarization.

The features present in Figures 4.2 and 4.4 are collected in Table 4.1.

4.2 Electrochemistry of FeSO$_4$ and Na$_2$S$_2$O$_3$ in Water

When FeSO$_4$ and Na$_2$S$_2$O$_3$ are mixed in solution, the lower pH of the solution caused by the presence of Fe(II) will accelerate the spontaneous disproportionation of S$_2$O$_3^{2-}$ to SO$_3^{2-}$

Feature Label	Reaction
A	H_2O oxidation, $Fe(II) \rightarrow Fe(III)$
B	$Fe(III) \rightarrow Fe(II)$
C	$SO_4^{2-} \rightarrow S_2^{2-}$
D	$2Fe + S_2^{2-} + 2\,e^- \rightarrow 2\,FeS + 4\,e^-$
E	$S_2^{2-} \rightarrow S^{2-}$
F	$Fe(II) \rightarrow Fe$
G	Tail of F
H	Slowing of F
I	$Fe \rightarrow Fe(II)$ $FeS \rightarrow Fe(II) + SO_4^{2-}$

Table 4.1: Reaction assignments for features in CV's of aqueous $FeSO_4$ solutions displayed in Figures 4.2 and 4.4

and S_x with small amounts of S^{2-} and polythionates. This means that the lifetime of the untitrated deposition solution will be shorter than our reference, but should be comparable to that of a solution of similar pH. Additionally, any Fe(III) formed in solution by atmospheric oxidation will be reduced to Fe(II) by the process:

$$Fe(III) + S_2O_3^{2-} \leftrightharpoons FeS_2O_3^+ \tag{4.18}$$

$$FeS_2O_3^+ + S_2O_3^{2-} \leftrightharpoons FeS_2O_3 + S_2O_3^- \tag{4.19}$$

$$FeS_2O_3^+ + S_2O_3^- \rightarrow Fe(II) + S_4O_6^{2-} \tag{4.20}$$
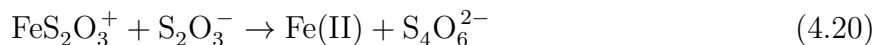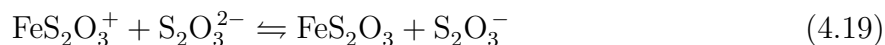
This adds tetrathionate to the reaction mixture without the process of electrode reduction [100, 91, 101]. Finally, Fe(II) is present in solution both complexed with thiosulfate and as the aquo species [102].

Figure 4.8 displays the first two cycles of a CV of 60 mM $FeSO_4$ and 100 mM $Na_2S_2O_3$ at the solution's untitrated pH of 4.48. The most dramatic difference between the two cycles is the appearance of feature E in the second cycle. For the most part, over the course of several cycles, the trends observed in the first two cycles continue to occur. Feature E gradually grows larger while feature F becomes smaller and less sharply defined. Features J and K decrease in charge (feature J is slightly larger in Figure 4.8, but in subsequent cycles begins to decrease in charge as well. Features M and N grow larger and merge to form a single, broader peak. Features O and P do not change significantly after the second cycle, and feature C does not change significantly at all during the course of a ten cycle experiment.
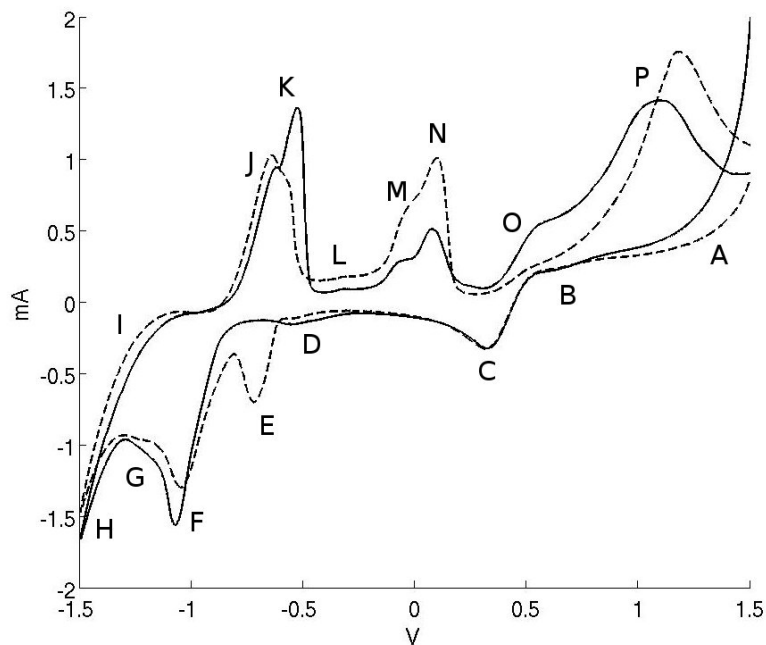
Figure 4.8: The first (solid line) and second (dotted line) cycles of a CV of 60 mM $FeSO_4$ and 100 mM $Na_2S_2O_3$, at its untitrated pH of 4.48 (1.5 V / -1.5 V vs. Ag / AgCl, 50 mV / sec)

Feature A is easily assigned to the solvent oxidation/reduction reaction

$$2\,H_2O \rightleftharpoons 4\,H^+ + O_2 + 4\,e^- \tag{4.21}$$

Over the course of this feature, however, it is important to realize that all other unoxidized species are also being oxidized. Thus, for example, Fe(III) is being formed at the electrode from Fe(II) present in the solution, despite the reductive power of the thiosulfate.

Feature B is only noticeable in a small number of CV's. It is not properly a separate feature in itself, but rather represents the slowing of the reactions which produce the current in feature P as the anodic overpotential is decreased.

Feature C can be readily identified by comparison with a CV of a 60 mM $FeSO_4$ solution discussed in Section 4.1. Figure 4.9 displays an overlay of a 60 mM $FeSO_4$ cyclic voltammogram with the data from the composite system. Feature C matches well with the reaction

$$Fe(III) + e^- \rightarrow Fe(II) \tag{4.22}$$

which was identified in Section 4.1. The Fe(III) in this case has been formed at the electrode surface during the previous application of more anodic potentials. The potential of this reaction is 560 mV vs. Ag / AgCl, but this potential is lowered in many cases by complex
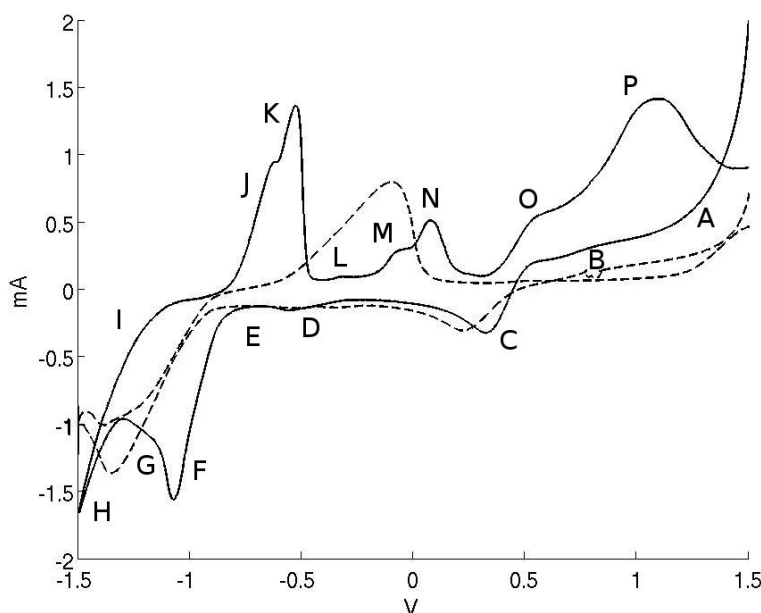
Figure 4.9: CV of 60 mM FeSO$_4$ and 100 mM Na$_2$S$_2$O$_3$, at its untitrated pH of 4.48 (solid line) with CV of 60 mM FeSO$_4$ (dotted line) (1.5 V / -1.5 V vs. Ag / AgCl, 50 mV / sec)

formation [91]. For example, the potential of the Fe(II) / Fe(III) couple in M H$_2$SO$_4$ is 470 mV vs. Ag / AgCl. The lowering of the reaction potential in this particular solution is due to the formation of thiosulfate complexes with the two reacting species.

Feature D produces just enough current to be observable, and is not large enough to be visible in many CV's. Peak exclusion experiments link it with anodic feature L. The potential at which it is situated indicates that this feature is due to the reduction of SO$_4^{2-}$ at the electrode by the mechanism shown in Figure 3.5. The small size of this feature is due to the slow kinetics of this reaction.

Features E, F, and G are complex and interrelated electrode interactions and will be treated together with their corresponding anodic reactions, J, K, M, and N.

Feature H is the solvent reduction reaction

$$2\,H^+ + 2\,e^- \rightarrow H_2 \tag{4.23}$$

which can be observed by the production of bubbles at the electrode surface at low potentials. If the voltammogram is carried to much lower potentials (*e.g.* -2.0 V) the action of these bubbles will physically dislodge the black deposits formed on the electrode during the previous cathodic waves.

Feature I is nothing but the slowing of the solvent reaction in feature H as the cathodic
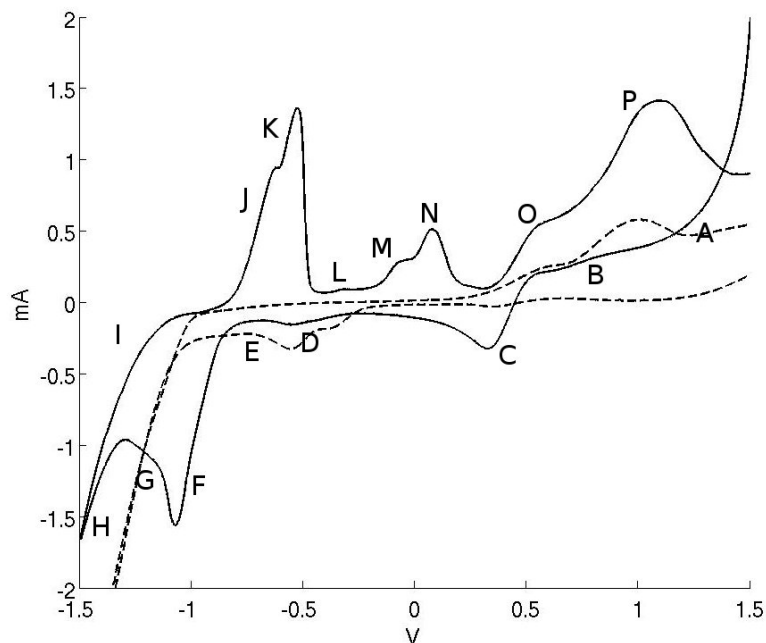
Figure 4.10: CV of 60 mM FeSO$_4$ and 100 mM Na$_2$S$_2$O$_3$ at pH 4.48 (solid line) with CV of 100 mM Na$_2$S$_2$O$_3$ at pH 4.55 (dotted line) (1.5 V / -1.5 V vs. Ag / AgCl, 50 mV / sec)

overpotential is decreased.

Feature L is the reverse of the reaction in feature D.

Feature O is the reverse of the oxidation in feature C. Feature O is much more variable in charge than feature C. In some conditions it is completely absent, while in others is greatly exaggerated. This indicates that the products of the preceding anodic waves are not the same in all cases.

Feature P can be identified by comparison with a CV of 100 mM Na$_2$S$_2$O$_3$ solution. Figure 4.10 displays an overlay of this solution with the composite data. It can be seen that feature P matches well with the thiosulfate oxidation wave. The higher current of feature P relative to the reference CV is due to the higher surface area of the Fe-modified electrode, the higher ionic strength of the solution containing FeSO$_4$, and the greater reactivity of thiosulfate complexed with iron [102].

Cathodic features E, F, and G and anodic features J, K, M, and N are those which involve a solid reactant or product. A good amount of background and discussion will be needed before we can assign reactions to these features.

As it is the first of these features temporally observed on our first CV cycle, we will start our discussion with feature F. As can be seen in Figure 4.9, feature F is the closest to the reduction potential of Fe(II) to Fe in our model FeSO$_4$ solution, but is anodically shifted by about 100 mV.

Elemental analysis via electron microprobe of platinum films held for one hour in this solution at -0.9 V, just after the onset of feature F, displays a 1:0.59 elemental ratio of Fe to S. This ratio indicates that both elemental iron and some form of sulfur are deposited at this point. Thiosulfate reduction would be the most likely source of sulfur. XRD analysis reveals no diffraction peaks that are not attributable to the substrate, indicating amorphous deposition.

Studies have been performed on the electrode processes of similar $Fe-S_2O_3^{2-}$ solutions at mercury electrodes which may shed light on the origin of the observed shift in the onset potential for Fe deposition. Itabashi reports a cathodic peak at -1.02 vs. SCE (-1.05 vs. Ag/AgCl), with his data showing the potential of the feature's onset being shifted anodically by about 200 mV relative to that of the aquo species [103]. Winkler and Krogulec report an anodic shift of their iron deposition peak relative to the aquo Fe(II) ion, though they do not report the magnitude of the shift [102]. To explain this shift, Itabashi cites a catalytic effect on Fe(II) reduction caused by adsorbed thiosulfate ions on the electrode surface. Winkler and Krogulec object that thiosulfate ions should not be adsorbed on the electrode as the deposition potentials are far more negative than the point of zero charge for their electrode in $S_2O_3^{2-}$ solution and support this objection experimentally with capacity curve data.

Despite this objection, the deposition mechanism proposed by Itabashi does have some attractive features and is worth examining.

$$Fe(II) + [S_2O_3^{2-}]_{ads} \rightarrow [Fe(II)S_2O_3^{2-}]_{ads} \tag{4.24}$$

$$[Fe(II)S_2O_3^{2-}]_{ads} + 2\,e^- \rightarrow [Fe(0)S_2O_3^{2-}]_{ads} \tag{4.25}$$

$$[Fe(0)S_2O_3^{2-}]_{ads} \xrightarrow{A} Fe^0 + S_2O_3^{2-} \tag{4.26}$$

$$[Fe(0)S_2O_3^{2-}]_{ads} \xrightarrow{B} FeS^{\,ads} + SO_3^{2-} \tag{4.27}$$
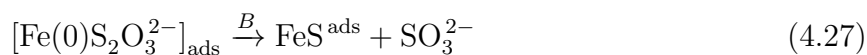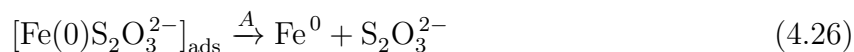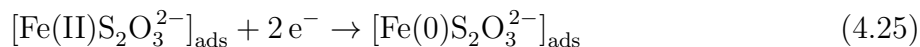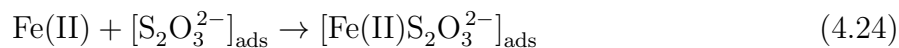
The existence of $[S_2O_3^{2-}]_{ads}$ is unlikely due to the highly negative charge of the electrode at the potentials in question, and so Reaction 4.24 should be discarded. Reaction 4.25 proposes the reduction of complexed Fe(II) to complexed Fe(0). Since the $[Fe(II)S_2O_3^{2-}]$ complex is known to be quite stable in these solutions and is overall neutral, its adsorption to the electrode surface is not as implausible as that of $[S_2O_3^{2-}]$. The single-step reduction of this complex is supported, though not necessarily proven, by Winker and Krogulec's analysis of their own voltammetric curves, from which they obtained α values close to 2. Once the zero-valent complex is formed on the electrode surface, it decomposes by two different pathways. Reaction 4.26 indicates the dissociation of the complex, while Reaction 4.27 indicates the chemical reaction of thiosulfate with metallic iron, forming iron sulfide and sulfite.

Reaction 4.26 is a plausible reaction path for the reduction to metallic iron given that the typical two step process observed in non-complexing solutions and detailed in Section 4.1 is not observed. The anodic potential shift of this feature relative to the $FeSO_4$ solution can be accounted for by the lower stability well of $[Fe(II)S_2O_3^{2-}]_{ads}$ compared to the undefined hydroxide intermediates described in Reactions 4.1 to 4.3.

Reaction 4.27 is less plausible, however. While $Fe(0)$ will react with thiosulfate if only thermodynamics are considered, there are significant kinetic barriers to this reaction. A more likely reaction is the reduction of the complexed thiosulfate by the electrode, forming sulfite and sulfide as in Figure 3.6. It is well known that sulfide ion reacts quickly with $Fe(0)$ to form FeS [95, 96, 97, 89, 98]. It is likely that the presence of Fe will increase the rate of this reduction relative to that of the same reaction on a bare platinum electrode by providing favorable reaction sites on the electrode surface. Thus, Reaction 4.27 should be more correctly written in two steps as

$$[Fe(0)S_2O_3^{2-}]_{ads} + 2\,e^- \xrightarrow{B} [Fe(0)S^{2-}]_{ads} + SO_3^{2-} \tag{4.28}$$

$$[Fe(0)S^{2-}]_{ads} \xrightarrow{B} FeS + 2\,e^- \tag{4.29}$$
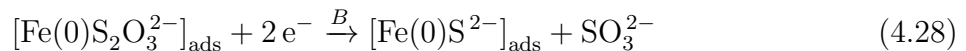
If these two reactions are added, we obtain Reaction 4.27. The spontaneous formation of FeS on Fe surfaces exposed to S^{2-} implies that it is likely that Reaction 4.28 is the rate limiting step in the overall process of Reaction 4.27.

An analogous reaction can also be conceived involving the initially adsorbed $[Fe(II)S_2O_3^{2-}]_{ads}$ complex, as detailed below.

$$[Fe(II)S_2O_3^{2-}]_{ads} + 2\,e^- \to [Fe(II)S^{2-}]_{ads} + SO_3^{2-} \tag{4.30}$$

$$[Fe(II)S^{2-}]_{ads} \to FeS_{ads} \tag{4.31}$$
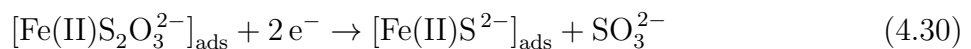
A look at the Pourbaix diagram in Figure 4.1 indicates that according to thermodynamic analysis, sulfur is reduced to $S(-II)$ at less negative potentials than iron is reduced to $Fe(0)$ in these solutions. At relatively less reducing potentials, then, we should see Reaction 4.30 dominating insofar as the $[Fe(II)S_2O_3^{2-}]$ species is concerned. However, the reduction of thiosulfate will have kinetic barriers, while the reduction of the complexed iron should have fewer. Further, $Fe(0)$ can also be formed from the aquo ion.

Another important process in the progression of these CV's is the modification of the electrode surface with both FeS and metallic iron. A very recent study by Bura-Nakić *et al.* has addressed the provenance and the effects of these surface modifications on mercury electrodes

in solutions of Fe(II) and S(-II) [104]. They detail two processes by which FeS is initially formed on the surface of mercury electrodes. The first involves the reaction

$$HgS + Fe^{2+} + 2\,e^- \rightarrow Hg^0 + FeS \tag{4.32}$$

which involves the HgS formed on the surface of a mercury electrode in sulfide solutions at potentials around -0.65 V vs. Ag / AgCl [105]. While it is possible for platinum to form an analogous PtS compound, the oxidation potential for the formation of this platinum sulfide is around +0.835 V vs. Ag / AgCl [106, 107]. This is much more anodic than the potentials at which significant quantities of S^{2-} would be formed at the electrode from the thiosulfate solutions under investigation, so a similar mechanism involving the platinum electrode is unlikely.

While this mechanism is unlikely, the potential at which the peak for the formation of FeS at these potentials is observed is about -0.55 V vs. Ag / AgCl [102, 103, 104], the potential of our feature E on platinum electrodes. The data examined by previous groups display the same multi-cyclic dependence that is observed in our own data, wherein this reductive feature is absent in the first cycle and grows steadily larger over further cycling. Itabashi explains this as due to the formation of HgS during the anodic wave of the experiment. Excluding an anodic peak attributed to the reverse of Reaction 4.32 at about -0.45 V eliminated the reductive peak in all waves, and made this a convincing conclusion. Winkler and Krogulec and Bura-Nakić *et al.* agree with this assessment.

The fact that a peak with the same characteristics as observed for the mercury electrodes is seen on platinum suggests that Reaction 4.32 is not an accurate description of this process. We propose that feature E arises instead from the reduction of the $[\mathrm{Fe(II)S_2O_3^{2-}}]_{\mathrm{ads}}$ complex to FeS and SO_3^{2-} on an electrode which has been modified with FeS. There is abundant evidence for this assignment.

A number of investigators have observed effects of surface modifications of mercury electrodes during CV's in iron-thiosulfate and the similar iron-thiocyanate system [102, 103, 104, 108, 109]. Itabashi reports that the presence of FeS facilitates the reduction of the $[\mathrm{Fe(II)-S_2O_3^{2-}}]$ complex to iron [103]. Cited as evidence is a hysteresis in voltammograms wherein the current at potentials low enough to produce iron deposition is higher on the anodic sweep than the initial cathodic sweep. Winkler and Krogulec, on the other hand, hold that large amounts of FeS inhibit Fe reduction, though they cite no evidence for this position [102]. Bura-Nakić *et al.* hold with Itabashi, reporting that Fe(II) reduction in the presence of FeS occurs at potential shifted anodically some 300 mV relative to Fe(II) reduction at the bare Hg electrode [104]. The feature they assign to Fe(II) reduction onto FeS occurs at -1.1 V vs. Ag/AgCl. As evidence that this feature is due to Fe(II) reduction they plot the dependence of the charge of this feature against the concentration of unprecipitated Fe(II) in solution and find a linear agreement, even well past the equivalence point of Fe(II) and S(-II).

The -1.1 V Fe reduction peak overlaps with the Fe reduction peak for the bare platinum
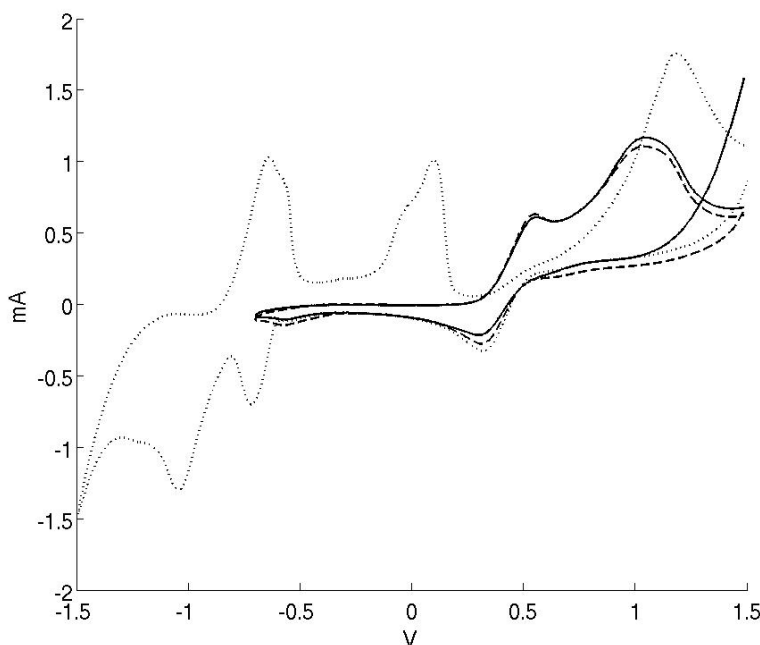
Figure 4.11: First two cycles of a CV of 60 mM FeSO$_4$ and 100 mM Na$_2$S$_2$O$_3$ (solid and dashed lines) with an anodic switching potential of -0.7 V. The second cycle of a CV of similar solution with an anodic switching potential of -1.5 V is displayed for reference (dotted line) (1.5 V / -1.5 V vs. Ag / AgCl, 50 mV / sec)

electrode and thus is part of our feature F. However, the fact that an FeS surface modifies the electrode enough to substantially shift the iron reduction peak gives credence to the hypothesis that FeS-modified surfaces also facilitate the reduction of Fe(II)$-$S$_2$O$_3^{2-}$ to FeS. Feature E is observed in the second sweep of the system, after some FeS is deposited during feature F by Reactions 4.28 and 4.29 or Reactions 4.30 and 4.31. An analysis of the oxidative current versus the reductive current of the features observed and accounting for H$_2$ formation shows that significant amounts of reduced species are not subsequently anodized on the anodic sweep. Further, the surface of the platinum electrode is visibly black at the completion of the experiment at the extreme anodic potential. This indicates that a solid species reduced onto the electrode surface does indeed remain deposited throughout the cycle. The low oxidation potential and the high current observed during Fe stripping in Section 4.1 indicate that it is unlikely that Fe is the material remaining behind. Therefore we know that the electrode has been modified with FeS.

Peak exclusion experiments also support this assignment for feature E. Figure 4.11 displays a cyclic voltammogram of the model Fe-S$_2$O$_3^{2-}$ solution with the anodic switching potential at -0.7 V, above the onset potential of feature F but below the onset potential of feature E. As can be seen, feature E does not appear on either the first or the second cycles, and indeed never appears during the entire 10 cycle experiment. Here, because the electrode is not modified during feature F, feature E is not present. If a mechanism like that presented

in Reaction 4.32 were responsible for feature E, it should have been observed during this experiment.

As previously mentioned, Bura-Nakić *et al.* propose two mechanisms of FeS deposition. The first of these we just discussed in more detail than the reader probably wished to know. The second mechanism involves the adsorption on the electrode surface of colloidal FeS nanoparticles spontaneously formed in solutions containing Fe(II) and S(-II). The experiments of Bura-Nakić *et al.* show that in solutions containing an appropriate amount of Fe(II) and S^{2-}, colloidal FeS forms quite quickly. Further, they show convincing electrochemical evidence for the surface modification of mercury electrodes immersed in such solutions. The amount of observed surface modification is decreased if the solution is not saturated with dissolved Fe^{2+} and S^{2-}, as determined by tabulated thermodynamic data [104].

While there is no S^{2-} in our solutions to produce the saturation required to induce the precipitation observed in these experiments when the solutions are initially formed, the gradual acid-catalyzed breakdown of $S_2O_3^{2-}$ will produce some sulfide in older solutions. Electrode reduction of thiosulfate will produce large local concentrations of sulfide at the electrode surface, as well, although the formation of FeS by this process has already been discussed in Reactions 4.30 and 4.31.

This mechanism of FeS surface modification is significant in our own investigation because older solutions exhibit feature E on the first cycle, before the electrode has been modified by FeS in feature F. An example of this can be seen in Figure 4.12, which displays the first and second cycles of a CV of the same solution used to obtain the voltammograms in Figure 4.8, but aged two hours. Feature E can be clearly observed on the first cycle, albeit shifted cathodically by about 50 mV. This can be explained by the adsorption of colloidal FeS to the electrode surface before the beginning of the experiment. The cathodic shift can be understood as the extra driving force required for the reduction on FeS that is not well adhered to the electrode surface.

The hypothesis that FeS surface modification occurs in solution was tested by soaking a platinum film in a sample of our deposition solution. The silver surface of the film quickly acquired a golden hue which was retained after drying. XRD analysis showed only platinum peaks, indicating that the surface modification consists of one or a few monolayers or that the film is not crystalline.

Winkler and Krogulec observe the reduction of FeS to Fe(0) and S^{2-} at -1.32 V vs. Ag / AgCl [102, 108]. This potential and relative magnitude of the current observed in their experiments match well enough with feature G in our own study to allow the assignment of the reaction

$$FeS + 2\,e^- \rightarrow Fe(0) + S^{2-} \tag{4.33}$$

to feature G.
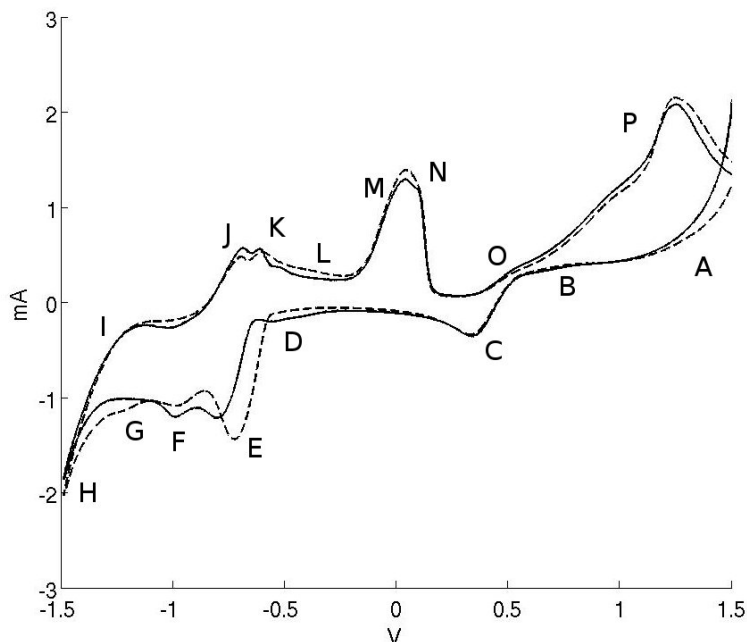
Figure 4.12: First (solid line) and second (dashed line) cycles of a CV of 60 mM FeSO$_4$ and 100 mM Na$_2$S$_2$O$_3$ aged for two hours (1.5 V / -1.5 V vs. Ag / AgCl, 50 mV / sec)

With the troublesome cathodic peaks identified, our anodic peaks J, K, M, and N fall neatly into place. Features J and K show the characteristic sharp drop off of a stripping peak. Taken together they vary with the intensity of feature F. Their onset potential also agrees quite well with that of the Fe stripping peak, as can be seen in Figure 4.9. Thus, they can be assigned to iron stripping. The doublet is due to iron being stripped from different surfaces. K is much larger than J in the first cycle, in which feature E is absent. In subsequent cycles, K decreases more quickly than J, but both decrease in charge as feature F does the same. This allows us to assign J to the oxidation of Fe from FeS and K to the oxidation of Fe from metallic iron or the platinum electrode.

Features M and N also display the sharp drop-off of a stripping peak. The charge of these features taken together varies with that of feature E, although these features can be present if feature E is not, indicating multiple mechanisms of formation of the reactant involved. They vary inversely in charge with features J and K taken together, indicating that they involve the oxidation of products of a competing reaction. Feature M initially starts smaller than and separated from N, but over the course of multiple cycles they grow together into a larger, broad peak with a sharp onset and drop off. These peaks behave similarly in aged solutions – essentially, multiple cycles serve to age solutions prematurely. These observations coupled with our assessment of feature E allow us to assign these peaks to the stripping of FeS via sulfur oxidation. M is the stripping of FeS from an iron or platinum substrate, while N is stripping from a substrate of more FeS. The peaks come together in aged solutions due to the averaging effect of adsorbed colloidal FeS on the system.
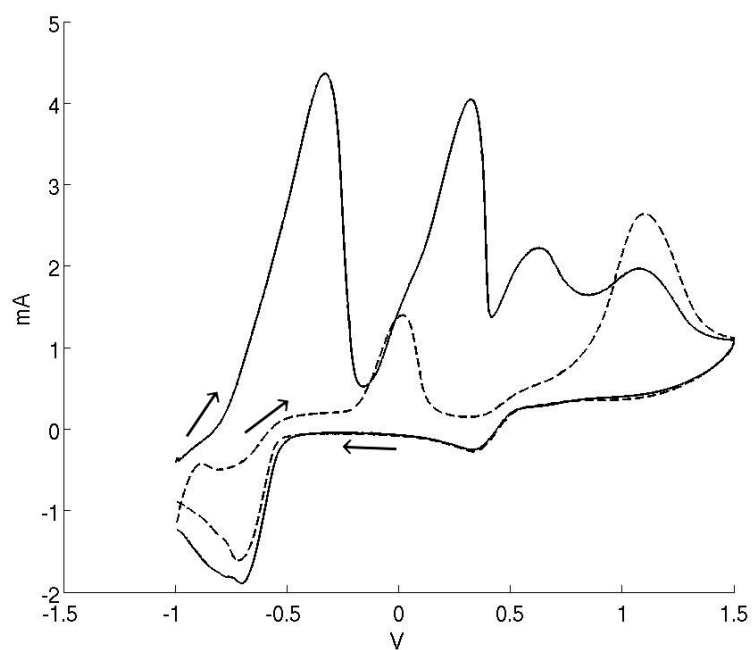
Figure 4.13: First (solid line) and second (dashed line) cycles of a CV of 60 mM FeSO$_4$ and 100 mM Na$_2$S$_2$O$_3$ held at -1.0 V for 120 seconds prior to measurement. Note that scan starts with an anodic wave - the arrows indicate the direction of scan. (-1.0 V / 1.5 V vs. Ag / AgCl, 50 mV / sec)

Feature Label	Reaction
A	H_2O oxidation
B	Slowing of P
C	$Fe(III) \rightarrow Fe(II)$
D	$SO_4^{2-} \rightarrow S_2^{2-}$
E	$[Fe(II)S_2O_3^{2-}]_{ads(FeS)} + 2\,e^- \rightarrow FeS + SO_3^{2-}$
F	$[Fe(II)S_2O_3^{2-}]_{ads(FeS,\ Pt,\ or\ Fe)} + 2\,e^- \rightarrow [Fe(0)S_2O_3^{2-}]_{ads(FeS,\ Pt,\ or\ Fe)}$ $[Fe(II)S_2O_3^{2-}]_{ads(Pt\ or\ Fe)} + 2\,e^- \rightarrow [Fe(II)S^{2-}]_{ads(Pt)} + SO_3^{2-}$ $Fe(II)_{ads(Pt\ or\ Fe)} + 2\,e^- \rightarrow Fe_{ads(Pt\ or\ Fe)}$
G	$FeS + 2\,e^- \rightarrow Fe(O) + S^{2-}$
H	H_2O reduction
I	Slowing of H
J	$Fe(0)_{\ ads(FeS)} \rightarrow Fe(II) + 2\,e^-$
K	$Fe(0)_{ads(Pt\ or\ Fe)} \rightarrow Fe(II) + 2\,e^-$
L	$S_2^{2-} \rightarrow SO_4^{2-}$
M	$FeS_{ads(Pt\ or\ Fe)} \rightarrow Fe(II) + SO_x + 2x+2e^-$
N	$FeS_{ads(FeS)} \rightarrow Fe(II) + SO_x + 2x+2e^-$
O	$Fe(II) \rightarrow Fe(III)$
P	$S_2O_3^{2-} \rightarrow SO_4^{2-} + S_2O_6^{2-}$ $SO_3^{2-} \rightarrow SO_4^{2-}$

Table 4.2: Reaction assignments for features in CV's of aqueous $FeSO_4$ and $Na_2S_2O_3$ solutions displayed in Figures 4.2 and 4.4

Further evidence for these peak assignments can be found in Figure 4.13. This figure shows the first and second cycles of a CV of a solution of 60 mM $FeSO_4$ and 100 mM $Na_2S_2O_3$ which was held at -1.0 V vs Ag / AgCl for 120 seconds before starting the anodic wave. In the first anodic wave, features J/K and M/N are extremely large, indicating that both Fe and FeS are deposited at -1.0 V. On the return scan, feature E is present, as is to be expected since the surface has been modified with FeS. More interesting is that on the return scan, we see no sign of features J or K, but the broad M/N peak is present. Here, all Fe(II) near the electrode has been used in feature E, producing FeS, some of which is subsequently oxidized in feature M/N on the anodic wave.

Table 4.2 sums up our assignments for the features observed in Figure 4.8.

4.3 Conclusions

The electrochemistry of the Fe(II)-$S_2O_3^{2-}$ system at a platinum electrode has been studied. The primary electrodeposition products are Fe(0) and FeS, and some portion of both products remain on the electrode surface after the anodic sweep.

Fe(0) is formed by the reduction of $[Fe(II)S_2O_3^{2-}]_{ads(Pt)}$, $[Fe(II)S_2O_3^{2-}]_{ads(Fe)}$, or Fe(II) at the surface of the electrode, as all species are present in solution. The reduction potentials of all three of these species are found to overlap. While iron begins to deposit at less cathodic potentials, it is not until potentials of around -0.8 V vs. Ag / AgCl that it begins depositing quickly enough to produce a cathodic peak. Iron begins stripping at a similar potential during the anodic sweep.

FeS is deposited by the reduction of $[Fe(II)S_2O_3^{2-}]$ to FeS and SO_3^{2-} or through the solution reaction of Fe(II) with S(-II) and subsequent adsorption of the colloidal product. FeS formation by $[Fe(II)S_2O_3^{2-}]$ reduction is found to be catalyzed by the presence of FeS on the electrode surface. FeS is formed on an unmodified electrode at potentials low enough to deposit Fe, below -0.8 V. FeS is formed on FeS at potentials of around -0.55 V vs. Ag / AgCl. This finding sheds light on previous investigations at mercury electrodes, in which a reductive feature at -0.55 V was assigned to HgS reduction and FeS formation. FeS starts to be stripped from the electrode starting at potentials of around -0.2 V.

In addition to understanding the electrochemistry of the system from a fundamentally scientific perspective, the goal of this study was to assess the usefulness of the Fe(II)-$S_2O_3^{2-}$ system for the electrochemical synthesis of pyrite, FeS_2. These results indicate that pyrite is not likely to form through electrochemical manipulation of the system. Although pyrite is thermodynamically the most stable at many of these potentials, it does not appear that the S_2^{2-} ions required to form pyrite will form from thiosulfate, even through careful tuning of the solution potentials. Most deposition occurs through the mediation of the $[Fe(II)S_2O_3^{2-}]$ complex, which will not be able to reduce to FeS_2. Any S^{2-} or S^0 at the electrode surface which might otherwise be oxidized or reduced to S_2^{2-} will quickly react with Fe(II) or Fe(0) to form FeS. This situation indicates that the most promising route towards the synthesis of FeS_2 would be one in which S_2^{2-} were formed directly. The use of a molten salt synthesis would likely help this process, as S_2^{2-} tends to react quickly in water.

Chapter 5

Electrochemistry of Aqueous CuSO$_4$ and Na$_2$S$_2$O$_3$

The first step toward creating a viable electrochemical synthesis of cuprous sulfide (Cu$_2$S) is a complete understanding of the electrochemical system in question. As discussed in Chapter 3, redox chemistry involving sulfur is especially complex. This complexity is compounded by the array of possible complexes formed by copper and the myriad of sulfur anions present in solution at various electrochemical potentials. This chapter will present the results of cyclic voltammetric studies of the thiosulfate / copper system. The goal of this work is to determine an appropriate set of deposition parameters for the creation of high quality Cu$_2$S nanowires through templated electrodeposition.

As previously explored, thiosulfate is not stable in acidic media, decomposing by the mechanism in Figure 3.2. However, thiosulfate forms a strong complex with Cu(I) [7]. It is expected that the stability of this cuprous-thiosulfate complex will decrease the rate of thiosulfate autodissociation, as well as increase the amount of Cu(I) in solution relative to a typical CuSO$_4$ solution. For this reason, in aqueous solutions of thiosulfate and copper sulfate it is reasonable to expect that conditions suitable for the electrochemical synthesis of Cu$_2$S can be identified.

5.1 Electrochemistry and pH Dependence of CuSO$_4$ in Water

It is useful to start an electrochemical analysis with an examination of the thermodynamic properties of the system in question. Figure 5.1 displays a Pourbaix predominance diagram for an aqueous solution of 60 mM CuSO$_4$. The most notable part of this diagram is the strange behavior of the copper sulfides, illustrated in further detail by the fractionation
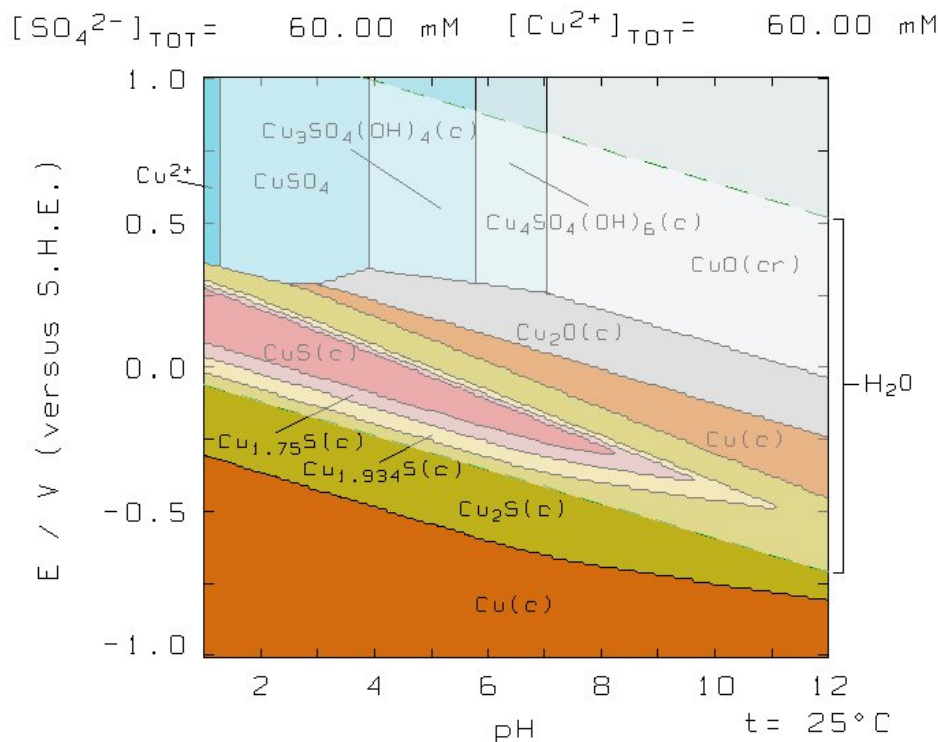
Figure 5.1: Pourbaix diagram for a system with 60 mM in aqueous Cu species and 60 mM in aqueous S species at 25° C, created using Medusa [2].

diagram in Figure 5.2. At pH values a bit acidic of neutral, copper metal can be formed. As the electrode potential is changed to more reducing values, the copper is (unintuitively) oxidized first to Cu(I) in the form of Cu_2S. Following this, Cu passes through progressively more oxidized species until reaching 100% Cu(II) in the form of CuS. Finally, at very negative potentials, the Cu(II) is reduced through the same series of oxidation states before reaching fully reduced Cu metal again.

This unusual thermodynamic behavior is due to the fact that the stability of each of these compounds is dependent upon the relative stabilities of both copper and sulfur species. Following the potential in Figure 5.2 from high to low, the reduction of Cu(II) species to Cu(I) in the form of Cu_2O can be seen, then full reduction to Cu metal. As the potential is lowered further, Cu becomes oxidized to Cu(I) in the form of Cu_2S. At this point, the solution's reductive potential is low enough to reduce the sulfur present in SO_4^{2-}. At these potentials, the presence of Cu(I) stabilizes the reduced S^{2-} species enough that the thermodynamic driving force with respect to Cu reverses, and Cu(I) is formed. At more negative potentials, there is more driving force toward the creation of both Cu metal and S^{2-} species. The free energies of formation of the compounds involved indicate that this driving force is stronger for S^{2-}, meaning that the most stable compound will be dictated by the amount of S(-II) present. Thus, the most stable compound progresses until it finally ends at the most sulfur-rich stoichiometry, CuS. After this point, further increases in Cu oxidation state are
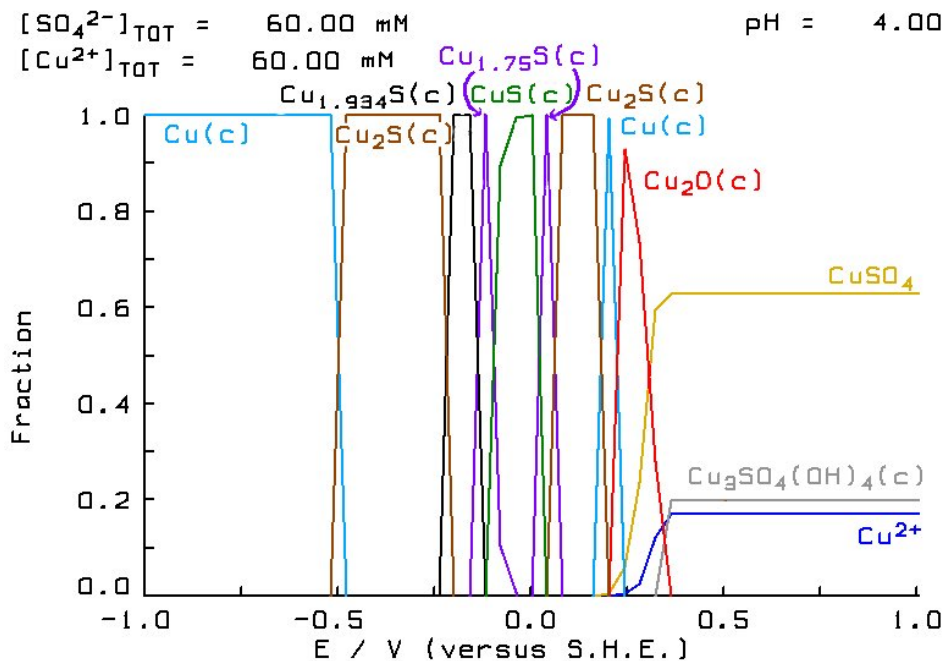
Figure 5.2: Fractionation diagram of 60 mM CuSO$_4$ at pH 4.0, created using Medusa [2]

no longer thermodynamically favorable. With even further decreased potential, the trend reverses, as the driving force toward the reduction of Cu destabilizes the Cu(II) and Cu(I) compounds, before finally, the two most stable species at very negative potentials are the fully reduced Cu metal and S(-II) (HS$^-$ or H$_2$S).

For our purposes, the large area of thermodynamic stability for Cu$_2$S is extremely promising. The fact that this area also overlaps with the area of water stability is likewise heartening. Initially, the high pH region seems like the most straightforward way to synthesize Cu$_2$S, as in this region there is a much lower presence of higher oxidation state copper. However, depositing metals from a basic solution works poorly in practical application. As can be seen in the Pourbaix diagram, CuO is very stable at these pH's, and will crash out of solution, making electrodeposition impossible. We will instead concentrate our investigations on lower pH solutions.

Before we turn our attention to the voltammetric studies of Cu solutions, it should be noted that though these thermodynamic calculations show the formation of a plethora of copper sulfides, it is unlikely that these will be observed in solutions of CuSO$_4$. The SO$_4^{2-}$ anion is a very unreactive species chosen for electrochemical experiments specifically for this purpose. The kinetic barriers to reaction presented in Chapter 3 will prevent SO$_4^{2-}$ from reacting extensively with Cu during the voltammetric experiments.

Figure 5.3 displays a cyclic voltammogram of 60 mM CuSO$_4$, titrated to pH 2.58 using
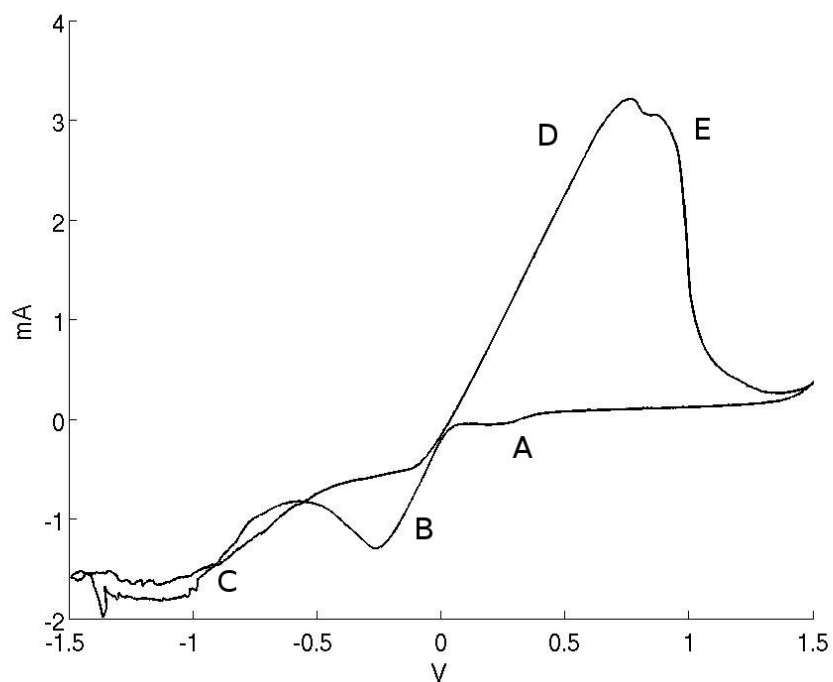
Figure 5.3: CV of 60 mM CuSO$_4$, titrated to pH 2.58 (1.5 V / -1.5 V vs. Ag / AgCl, 50 mV / sec)

sulfuric acid. Peak A corresponds to the reductive reaction

$$Cu^{2+} + e^- \rightarrow Cu^+ \tag{5.1}$$

This is a very small perturbation in current due to the low stability of Cu$^+$, and is likely more accurately described as

$$Cu^{2+} + e^- \rightarrow Cu^+_{ads} \tag{5.2}$$

wherein the Cu$^+$ species is stabilized by adsorption to the Pt electrode.

Peak B corresponds to the bulk deposition of Cu as

$$Cu^{2+} + 2\,e^- \rightarrow Cu \tag{5.3}$$

This peak assignment is verified through deposition experiments at below 0 V relative to Ag / AgCl which produce metallic copper films. The jagged features labeled C in Figure 5.3 are reduction reactions of the sulfate counterion and H$^+$. These reactions do not form clear peaks
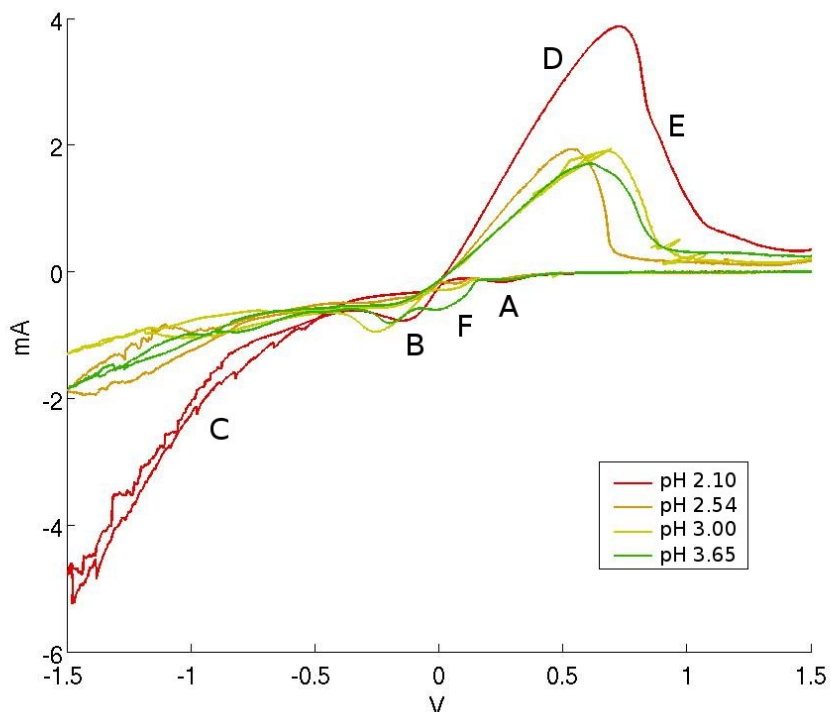
Figure 5.4: CV's of solutions of 60 mM CuSO$_4$, titrated to pH 2.10 (red), 2.54 (orange), 3.00 (yellow), and 3.65 (green) with sulfuric acid (1.5 V / -1.5 V vs. Ag / AgCl, 50 mV / sec)

due to the fact that as they occur, copper is plating quickly onto the surface of the electrode, changing its surface area unpredictably as well as obscuring the more favorable bare Pt electrode sites for hydrogen reduction. Feature D is the stripping of metallic copper from bulk by the reverse of Reaction 5.3. This assignment is corroborated by the characteristic sharp drop off of this peak, indicating that the source of reactive species is abruptly cut off – in this case, the surface is cleaned of Cu metal. Peak E is the stripping of the last Cu monolayer off of the platinum electrode.

On the whole, the potentials observed correspond well with the thermodynamically predicted potentials of reduction observed in Figure 5.1, taking into account that the the cyclic voltammogram is obtained relative to the Ag / AgCl reference.

Figure 5.4 shows a composite plot of CV's of CuSO$_4$ solutions at multiple pH's. The major features seen in Figure 5.3 are present and labeled similarly. There is also an additional feature, labeled F.

The most immediately noticeable comparative feature is the sharp increase in the current of features C and D at lower pH values. This increase is observed over multiple runs and begins at around pH 2.10, displayed in Figure 5.4. While a sizable amount of the increase in reductive current in feature C can be attributed to the increased rate of hydrogen production due to a higher concentration of free H$^+$, further investigation is required to explain the

increase of the stripping feature D.

To explain this feature we must first examine the mechanism of copper electrodeposition. Two mechanisms of copper deposition from $CuSO_4$ have been studied [110, 111, 43]. The first is the intuitive two step process

$$Cu^{2+}_{(aq)} + e^- \rightarrow Cu^+_{(aq)} \tag{5.4}$$

$$Cu^+_{(aq)} + e^- \rightarrow Cu \tag{5.5}$$

in which Reaction 5.4 is the rate limiting step at low Cu^{2+} concentrations, with the rate of Reaction 5.5 also affecting the overall current at the higher Cu^{2+} concentrations with which this study is concerned [110]. The second process is a heterogeneous equilibrium occurring after Reaction 5.4 to the tune of

$$2\,Cu^+_{(aq)} \rightleftharpoons Cu + Cu^{2+}_{(aq)} \tag{5.6}$$

In both cases, Reaction 5.4 is the common limiting step. This step will be slowed by a good complexing agent of Cu^{2+}, stabilizing the Cu^{2+} in solution thermodynamically and (more apropos to this discussion) providing kinetic barriers to Reaction 5.4. For the complexation reaction

$$Cu^{2+} + SO_4^{2-} \rightleftharpoons CuSO_{4\,(aq)} \tag{5.7}$$

$\log(K) = 2.35 \pm 0.05$ [112]. At higher pH values, SO_4^{2-} is the chief form of sulfate. As the pH value approaches pKa = 1.99 for HSO_4^- [63], however, progressively more of the SO_4^{2-} is converted to HSO_4^{2+}. The $\log(K)$ value for the complexation of Cu^{2+} by HSO_4^{2+} is substantially lower, at 0.8 ± 0.2 [113]. The lower complexation of the more predominant HSO_4^{2+} species at pH values near 2 allows more Cu^{2+} to be free at the electrode surface, increasing the deposition rate. The increased current of feature D is due to the larger mass of material deposited during the cathodic wave.

Another interesting observation in Figure 5.4 is the appearance and growth of feature F with increasing pH values. This feature is due to an underpotential Cu deposition as

$$Cu^{2+} + 2\,e^- \rightarrow Cu_{(ads)} \tag{5.8}$$

This underpotential deposition is well studied in the literature [114, 115], and will cease once a monolayer of copper has covered the available platinum. The increase in size at higher

Feature Label	Reaction
A	$Cu^{2+} \rightarrow Cu^{+}_{(ads)}$
B	$Cu^{2+} + 2\,e^{-} \rightarrow Cu_{(bulk)}$
C	Sulfate reduction reactions, H reduction
D	$Cu_{(bulk)} + 2\,e^{-} \rightarrow Cu^{2+}$
E	$Cu_{(ads)} + 2\,e^{-} \rightarrow Cu^{2+}$
F	$Cu^{2+} + 2\,e^{-} \rightarrow Cu_{(ads)}$

Table 5.1: Reaction assignments for features in CV's of aqueous $CuSO_4$ solutions displayed in Figures 5.3 and 5.4.

pH values is due to the fact that adsorbed hydrogen competes with and repells Cu^{2+} on the electrode surface [115], causing the rate of underpotential deposition to be retarded in solutions rich with H^{+} until more cathodic voltages are reached.

A summation of the peak assignments in Figures 5.3 and 5.4 is displayed in Table 5.1. This information will be used to inform the analysis of the composite system in the following section.

As expected, the thermodynamically predicted stability of the assortment of copper-sulfur species is not observed in this system due to the low reactivity of the SO_4^{-2} anion. In order to produce Cu_xS species in an aqueous system an alternate sulfur source must be used. In the following section we will explore the effect of adding thiosulfate to the electrochemical bath.

5.2 Electrochemistry of $CuSO_4$ and $Na_2S_2O_3$ in Water

When thiosulfate is introduced into a solution of $CuSO_4$, a number of species form in solution [61]. First, Cu^{2+} is reduced by thiosulfate by the reaction

$$2\,S_2O_3^{2-} + 2\,Cu^{2+} \rightarrow S_2O_6^{2-} + Cu_2^{2+} \tag{5.9}$$

Secondly, the Cu_2^{2+} moiety is well complexed by thiosulfate as

$$Cu_2^{2+} + 2\,S_2O_3^{2-} \rightarrow 2\,[CuS_2O_3]^{-} \tag{5.10}$$

followed by

$$[CuS_2O_3]^{-} + S_2O_3^{2-} \rightarrow [Cu(S_2O_3)_2]^{3-} \tag{5.11}$$
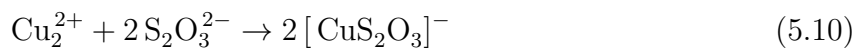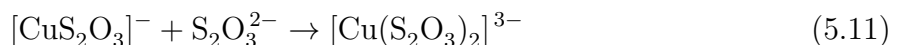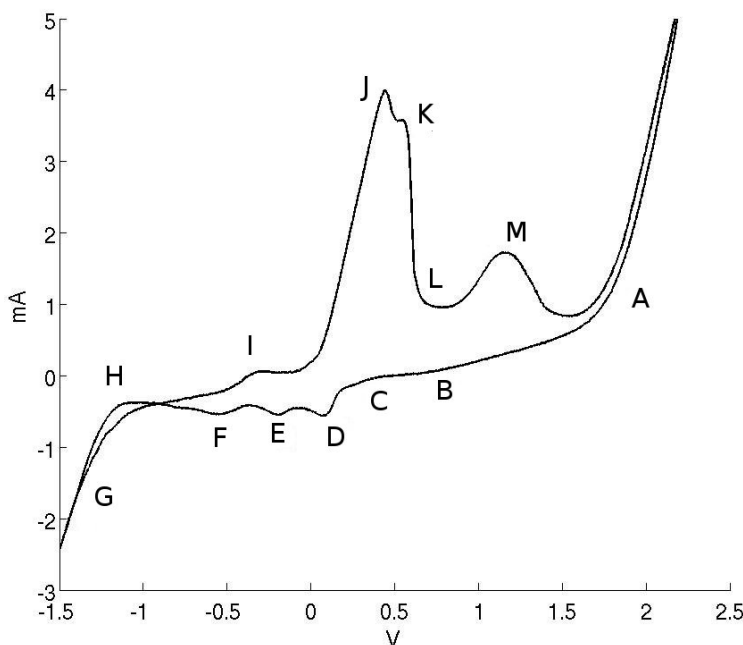
Figure 5.5: CV of a solution of 60 mM $CuSO_4$ and 100 mM $Na_2S_2O_3$, titrated to pH 3.58 with sulfuric acid (2.5 V / -1.5 V vs. Ag / AgCl, 50 mV / sec)

et cetera. Further, the complex aqueous thiosulfate chemistry detailed in Chapter 3 still occurs, meaning that significant amounts of SO_3^{2-} form in solution as well as some S^{2-}, S_8, and assorted polythionate ions. These ions can also have subsequent reactions with the Cu species in solution. For example, the S^{2-} can react with Cu as

$$Cu_2^{2+} + S^{2-} \rightarrow Cu_2S \tag{5.12}$$

or

$$Cu^{2+} + S^{2-} \rightarrow CuS \tag{5.13}$$

if steps are taken to increase the rate of S^{2-} production, as with gentle heating [61]. While these slower reactions will certainly have an effect on the solution makeup, the most important processes are the reduction in Reaction 5.9 and the complexations in Reactions 5.10 and 5.11.

Figure 5.5 displays a CV of 60 mM $CuSO_4$ with 100 mM $Na_2S_2O_3$, titrated to pH 3.58, with each peak assigned a label.

As with the iron system discussed in Section 4.2 of Chapter 4, feature A is due to the oxidation of water and feature B is due to the slowing of the $S_2O_3^{2-}$ oxidation reaction. The
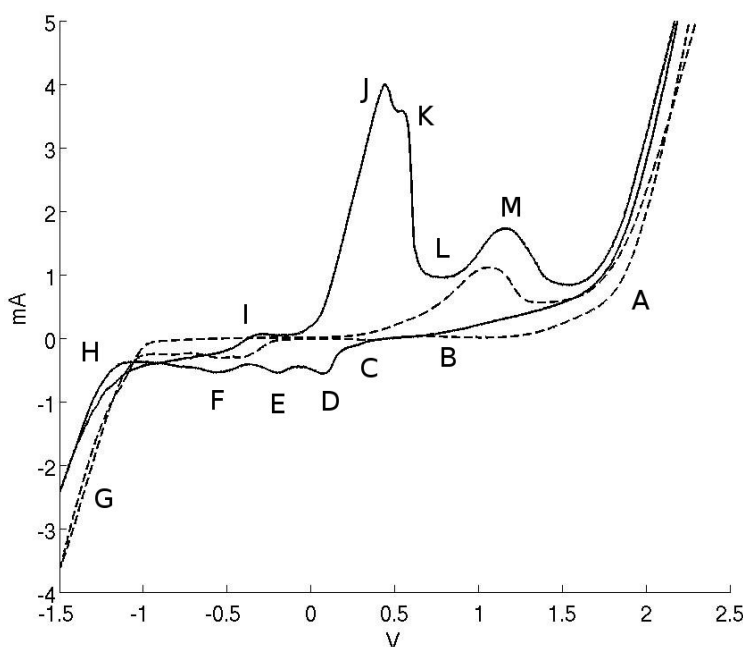
Figure 5.6: CV of a solution of 60 mM $CuSO_4$ and 100 mM $Na_2S_2O_3$, titrated to pH 3.58 with sulfuric acid (solid line) and CV of 100 mM $Na_2S_2O_3$, titrated to pH 3.44 with sulfuric acid (dotted line). (2.5 V / -1.5 V vs. Ag / AgCl, 50 mV / sec)

agreement of feature B with the corresponding feature in a solution of 100 mM thiosulfate can be seen in Figure 5.6.

Feature C can be identified by comparison with a CV of a solution containing only $CuSO_4$. Figure 5.7 displays an overlay of the CV from Figure 5.5 and a solution of 60 mM $CuSO_4$ titrated to a similar pH. It corresponds well with the solution phase reduction of Cu(II) to Cu(I) by Reaction 5.1. Feature C is small and almost unnoticeable in many voltammograms. While in the $CuSO_4$ system this was due to the instability of Cu^+, in the $CuSO_4$–$Na_2S_2O_3$ system Cu(I) is the primary species in solution due to reduction by thiosulfate so the majority of the Cu species are already reduced. Cu also complexes strongly with $S_2O_3^{2-}$ [113], preventing it from reacting.

Feature D agrees well with the underpotential copper deposition peak visible in Figure 5.7 and can be assigned to the reaction

$$[Cu_2S_2O_3]_{(aq)} + 2\,e^- \rightarrow 2\,Cu_{(ads)} + S_2O_3^{2-} \tag{5.14}$$
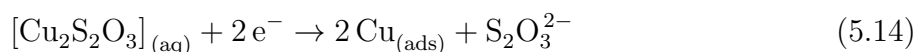
Feature E agrees with the bulk copper deposition peak seen in Figure 5.7, allowing it to be
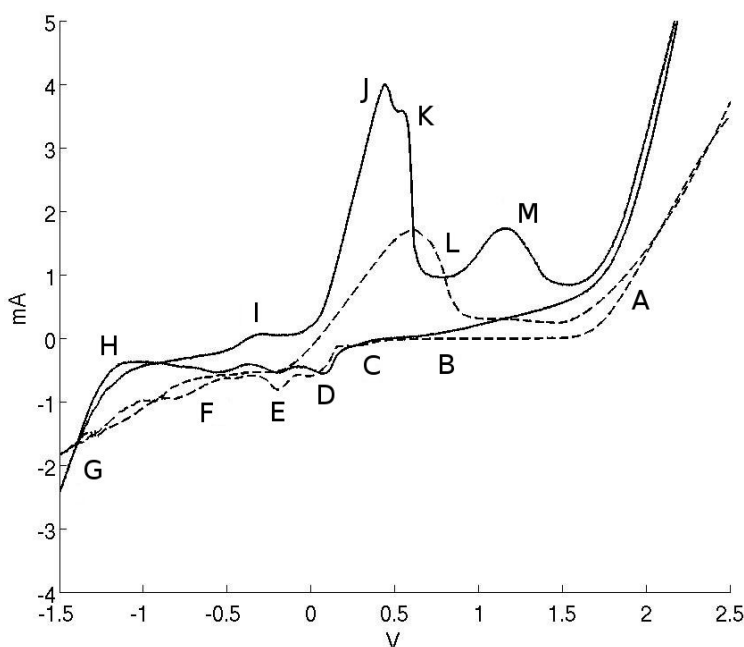
Figure 5.7: CV of a solution of 60 mM CuSO$_4$ and 100 mM Na$_2$S$_2$O$_3$, titrated to pH 3.58 with sulfuric acid and CV of 60 mM CuSO$_4$, titrated to pH 3.44 with sulfuric acid (dotted line). (2.5 V / -1.5 V vs. Ag / AgCl, 50 mV / sec)

assigned to the reaction

$$[Cu_2S_2O_3]_{(aq)} + 2\,e^- \rightarrow 2\,Cu_{(ads)} + S_2O_3^{2-} \tag{5.15}$$
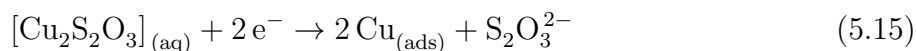
Feature F is the reduction of S$_2$O$_3^{2-}$ to S^{2-} and SO$_3^{2-}$. Since a great deal of the thiosulfate in solution will have complexed Cu$^+$ species (or more accurately, Cu$_2^{2+}$ moieties [61]), we will have multiple reactions occurring. First, the reduction of thiosulfate freed during earlier reduction of Cu$_2^{2+}$ will reduce as shown in Figure 3.6. The reduction of thiosulfate complexing copper, however, will proceed as

$$[Cu_2S_2O_3] + 2\,e^- \rightarrow Cu_2S + SO_3^{2-} \tag{5.16}$$
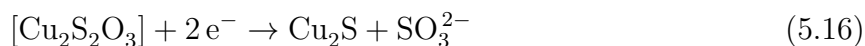
It is also possible for Cu(II) species to still be in solution either due to the oxidizing effect of one of the many sulfur species present or the disproportionation reaction

$$2\,Cu^+ \rightleftharpoons Cu + Cu^{2+} \tag{5.17}$$

with K $\approx 10^6$ [112]. In this case, reduction would instead result in CuS rather than Cu$_2$S.

This gives rise to the range of possible stoichiometries so characteristic of Cu_xS. Although Cu_2S will be the most common, the fact that Cu reduction can occur in parallel means that the observed stoichiometry will typically be Cu_xS with x < 2. While Cu_xS with x < 1 is not stable as a separate species, a combination of Cu_xS and metallic Cu could produce such stoichiometries in situations wherein the Cu_xS is deposited on top of Cu.

This assessment is supported by electron microprobe analysis of thin films deposited at potentials of -0.3 V and -0.7 V. At -0.3 V, the elemental ratio of Cu to S was 1:0.02, indicating a mostly copper film with likely a surface layer of Cu_xS. At -0.7 V, the elemental ratio was increased to 1:0.04, but samples showed many areas with greatly increased amounts of sulfur, indicating that some sulfur reduction is occurring in this regime. There were also a number of crystallites on the surface with stoichiometries of 1:0.5 Cu to S, likely the result of a chemical bath deposition mechanism similar to that explored by Grozdanov *et al.* [61].

Feature G is the hydrogen reduction reaction, and feature H merely the slowing of this process.

Feature I is due to the oxidation of S(-II) from Cu_xS formed over the course of feature F as

$$Cu_xS \rightarrow xCu^+ + S + 2\,e^- \tag{5.18}$$

The S will either be oxidized further or aggregate into colloidal S_8. The Cu^+ produced will be immediately reduced at the electrode surface (causing no net current) or be complexed by $S_2O_3^{2-}$.

Feature J agrees quite well with the copper stripping peak in the $CuSO_4$ solution, as can be seen in Figure 5.7. Further, experiments using a Cu electrode in thiosulfate solution display the same onset potential for Cu stripping. Finally, the sharp drop off of the peak is indicative of a stripping reaction. This evidence allows us to assign Feature J to the reaction

$$Cu \rightarrow Cu^+ + e^- \tag{5.19}$$

Feature K agrees well with the stripping of Cu from the Pt electrode (feature E in Table 5.1).

Feature L is the solution oxidation reaction

$$Cu^+ \rightarrow Cu^{2+} + e^- \tag{5.20}$$
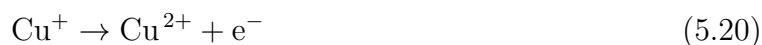
This reaction is not easily observable in all CV's, occasionally being obscured by current originating from features J and K. When it is present, it expresses substantially more current than feature C, its reductive counterpart. This is due to the local formation of uncomplexed Cu^+ at the electrode surface during the stripping reactions in the preceding features.
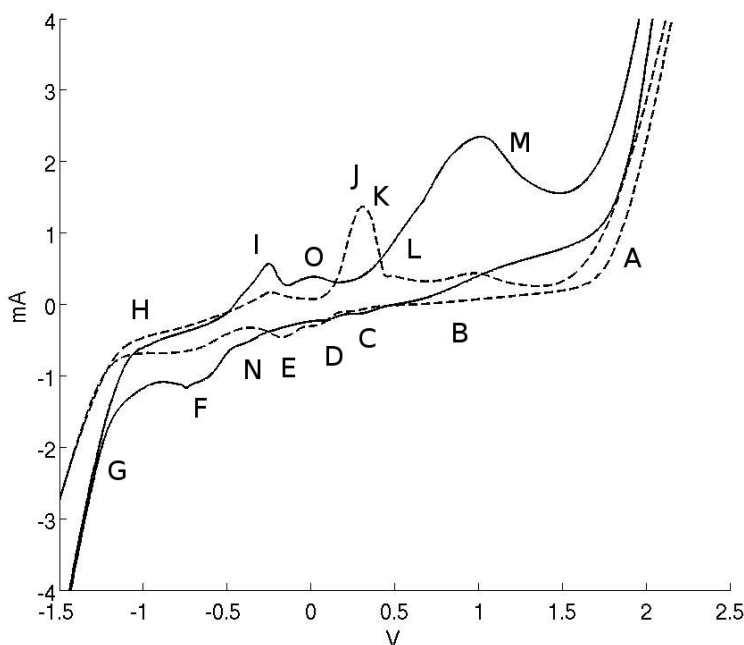
Figure 5.8: CV of a solution of 60 mM $CuSO_4$ and 200 mM $Na_2S_2O_3$, titrated to pH 3.06 with sulfuric acid (solid line) and CV of 60 mM $CuSO_4$ and 100 mM $Na_2S_2O_3$, titrated to pH 3.13 with sulfuric acid (dotted line). (2.5 V / -1.5 V vs. Ag / AgCl, 50 mV / sec)

Feature M is the oxidation of $S_2O_3^{2-}$ and descendant sulfur species as discussed in Chapter 3.

When the concentration of thiosulfate is increased, the $CuSO_4$–$Na_2S_2O_3$ system exhibits a marked change in its overall character and the introduction of two additional features. Figure 5.8 displays a CV of a solution of 60 mM $CuSO_4$ and 200 mM of $Na_2S_2O_3$ with a CV of 60 mM $CuSO_4$ and 100 mM $Na_2S_2O_3$ for reference. The most noticeable feature is the complete absence of features J and K in this CV. Features D and E are also not in evidence. There is a marked increase in the charge of features F and I and the introduction of two new features labeled N and O.

The increased complexing power of the solution with high $S_2O_3^{2-}$ concentration stabilizes Cu^+ in solution enough that metallic Cu is not formed in in features D and F. Feature N is due to the reduction of free, uncomplexed $S_2O_3^{2-}$. The increase in the reductive current of feature F is due to the larger amount of complexed Cu_2^{2+} which did not react during earlier features. Feature I is larger due to the greater amount of Cu_xS produced during feature F. Feature O is the oxidation of free S^{2-} formed during feature N.

A summary of the feature assignments for Figure 5.5 is displayed in Table 5.2.

Feature Label	Reaction
A	H_2O oxidation
B	Slowing of M
C	$Cu(II) \rightarrow Cu(I)$
D	$Cu^{2+} \rightarrow Cu^+_{(ads)}$
E	$Cu^{2+} + 2e^- \rightarrow Cu_{(bulk)}$
F	$[Cu_2S_2O_3] + 2e^- \rightarrow Cu_2S + SO_3^{2-}$ $S_2O_3^{2-} + 2e^- \rightarrow S^{2-} + SO_3^{2-}$
G	H_2O reduction
H	Slowing of G
I	$S(II)$ oxidation from Cu_xS
J	$Cu_{(bulk)} + 2e^- \rightarrow Cu^{2+}$
K	$Cu_{(ads)} + 2e^- \rightarrow Cu^{2+}$ $Cu_xS \rightarrow xCu^+ + S + 2e^-$
L	$Cu(I) \rightarrow Cu(II)$
M	$S_2O_3^{2-}$ oxidation
N	$S_2O_3^{2-} + 2e^- \rightarrow S^{2-} + SO_3^{2-}$
O	S^{2-} oxidation

Table 5.2: Reaction assignments for features in CV's of aqueous solutions of $CuSO_4$ and $Na_2S_2O_3$ displayed in Figures 5.5 and 5.8.

5.3 Conclusions

The aqueous $CuSO_4$–$Na_2S_2O_3$ system was studied using cyclic voltammetric methods at a platinum electrode. The primary electrodeposition products are $Cu(0)$ and Cu_xS.

$Cu(0)$ is deposited underpotentially onto the platinum electrode at a potential of 0.2 V vs. Ag / AgCl, followed by bulk deposition at -0.1 V. High concentrations of thiosulfate in solution inhibit this reaction by strongly complexing the copper reactant.

Cu_xS is deposited at potentials below -0.5 V with the reduction of sulfur in $[Cu_2Na_2S_2O_3]$ or higher complexes and simultaneous formation of SO_3^{2-}. As the kinetics of the reaction at the electrode surface are a major factor in the formation of products, Cu_2S is the natural stoichiometry of this reaction product by virtue of the structure of the reactant. However, disproportionation of the Cu_2^{2+} species can skew the product towards less copper-rich phases.

In addition to the scientific interest in understanding the solution electrochemistry of this system, the goal of this work was to evaluate the suitability of this system as a synthesis route for Cu_2S. The results indicate that tuning the thiosulfate concentration is the most important parameter in determining the Cu_xS stoichiometry. This is due to its dual role in both stabilizing $Cu(I)$ in solution as well as supplying sulfur to the reaction. It is suggested that, unintuitively, higher thiosulfate concentrations will produce more copper-rich Cu_xS,

as higher complexation of Cu(I) will prevent the introduction of Cu(II) into the deposition. Further, higher thiosulfate concentration makes the undesirable deposition of Cu metal less likely for the same reason.

Chapter 6

Isolated Nanowire Deposition

Over the course of my research into the electrodeposition of semiconductor materials onto template-modified electrodes, I found that oftentimes I would get materials to deposit past the alumina barrier layer. Being a curious scientist, I further investigated these anomalous depositions and was able to determine their cause and use them to good effect in obtaining transport measurements of the deposited wires. This chapter is an expansion on previously published work on the subject [116].

6.1 Background and Motivation

The measurement of transport properties in nanomaterials has been the subject of much research in the past decade [117, 118, 119]. The difficulty in making these measurements is often glossed over in the reporting of data, but a typical single wire transport measurement requires hours of work and no small amount of luck [119]. For this reason, many data on transport properties are drawn from measurements of a handful of nanowires. A method of wire characterization which allows for more rapid, repeatable measurements would increase the statistical validity of the data obtained.

One common method of taking transport measurements on individual wires involves suspending the nanowires in a solution and drop casting them onto an insulating substrate. Using an electron microscope, a suitable nanowire is selected. Focused ion beam deposition is then used to deposit a conductive electrode pattern around the wire, connecting it to a larger device [120].

A related method of single nanowire contacting involves preparing a substrate with premade electrodes created through nanolithography, then drop casting nanowires onto it. The concentration of nanowires is increased enough that it becomes reasonable to expect one to fall in the appropriate place so that it can be contacted and measured with the existing pat-

terned nanoelectrodes. Microscopy is used to determine where such fortuitous placements have occurred, and these sites are used to measure the wires. Oftentimes this technique is used in conjunction with "laser tweezers" or an atomic force microscope (AFM) tip in order to allow for more optimally positioned wires. Finally, electron beam lithography is used to contact the wires to the prefabricated electrodes [121].

A final method of nanowire contacting which is often used involves using the tip of an AFM to probe individual nanowires. If a single probe is used, the other end of the wire must be electrically connected as above or by virtue of its synthesis method [122]. A closely related technique involves using multiple prefabricated leads similarly to the AFM tip to make four-point probe measurements on arbitrary nanowires [123].

While often producing beautiful results, all of the above mentioned methods are resource intensive. At a minimum, each requires a microscope capable of resolving nano-scale materials. These techniques can also consume a great deal of time, as many steps are required to completely prepare a sample for measurement and an operator must be present for all of these steps. Finally, the aforementioned operator must be trained in the technique – these are not operations that can be performed by a layperson.

It is easy to imagine a number of other measurements that would be desirable but intractable with the above contacting methods. One such measurement involves embedding a wire completely in a matrix. This configuration is interesting due to the many important surface effects observed in nanomaterials; interface scattering of phonons [124], plasmon properties [125], and quantum confinement [126] are all affected by the nature of the interface producing them.

The creation of porous anodic alumina (PAA) is detailed in section 2.4. As can be seen in Figure 2.5, porous alumina is synthesized with a thin barrier layer at the bottom of every pore, preventing communication between the aluminum electrode and the pores themselves. Normally, this barrier is overcome by either removing the layer in some way before deposition or by using AC current, which treats the insulating barrier layer as a rectifier and still allows electron transfer [75]. Here we report a method by which nanowires can be synthesized using direct current deposition without a separate barrier-removal step. The resulting templates exhibit sparse and isolated nanowires reaching the surface of the template and overgrowing to produce hemispherical domes of overgrowth on the surface of the PAA. The sparseness of these overgrown wires and the domes of overgrowth may be exploited to simultaneously measure transport properties of a known, countable number of wires grown in PAA.

6.2   Experimental Details and Observations

Porous alumina templates were prepared in 0.2 M oxalic acid using a double anodization method [74] at 40 V. The first anodization was carried out at room temperature for 5 hours. The resultant alumina was then stripped in a solution of warm 0.45 M chromium oxide and
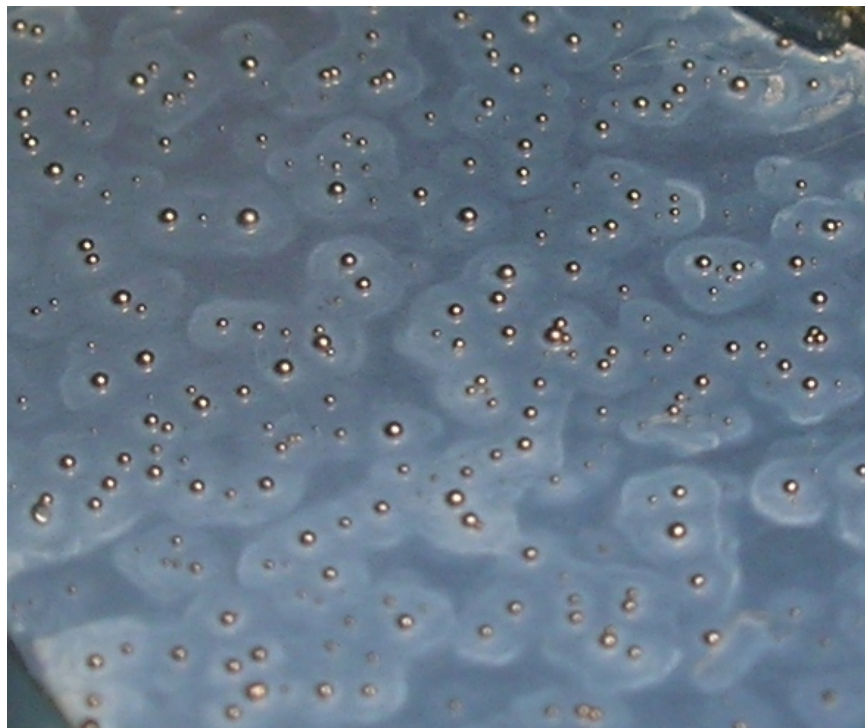
Figure 6.1: Optical micrograph showing the surface of a template with sparse nickel over-growth on its surface. The area shown is about 2 cm^2.

0.52 M phosphoric acid. The second anodization was carried out in an ice water cooling bath at 0 °C for 34 hours. This produced templates 60-70 μm thick with pores 35 nm in diameter.

The aluminum back of each template was attached to a copper armature using conductive silver paint. An active area of the template was masked off by painting on a mystical mixture of nitrocellulose and polyester resin known to the elves as Sally Hansen® Hard as Nails® colorless fingernail polish. The template was then immersed in the deposition solution appropriate to the desired metal. For nickel, an aqueous solution of 120 g/L $NiSO_4 \cdot (H_2O)_6$ and 45 g/L HBO_3 was used [127]. For copper, an aqueous solution of 2.1 g/L H_2SO_4 and 23.8 g/L $CuSO_4 \cdot (H_2O)_5$ was used [128]. For silver, an aqueous solution of 17 g/L $AgNO_3$ and 223 g/L KSCN was used, adapted from Riveros *et al.* [129]. The metals were then potentiostatically deposited. Relative to Ag/AgCl, nickel was deposited at a potential of -1.0 V, copper was deposited at a potential of -0.2 V, and silver was deposited at a potential of -0.25 V. Each template was soaked in the deposition solution for between 40 minutes and 18 hours before depositing, and each solution was stirred during soaking and deposition.

Nickel wires synthesized in this manner displayed isolated hemispherical spots of overgrowth, as seen in Figure 6.1. When the templates were processed and examined under SEM, no wires were seen in the plane of the cross section, as in Figure 6.2. Copper wires synthesized in this manner showed more abundant but still isolated overgrowth spots, as seen in Figure 6.3. Silver wires would not nucleate when synthesized this way, but the same templates
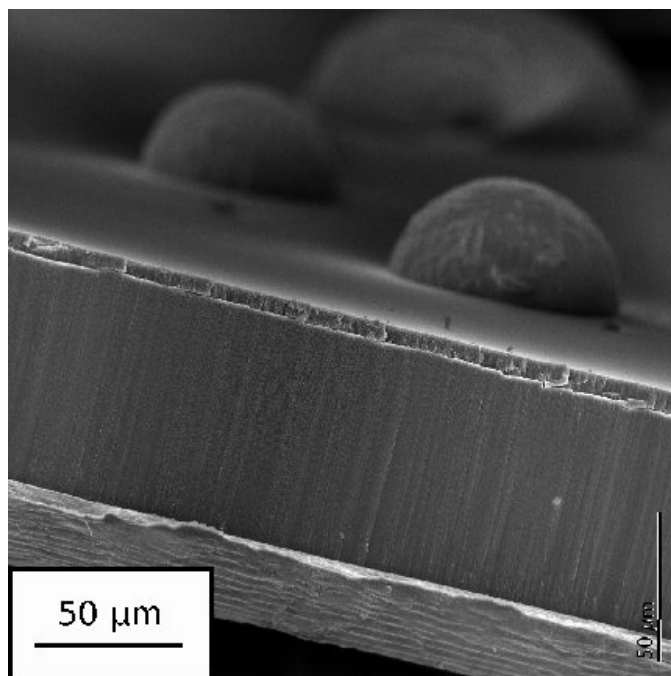
Figure 6.2: Scanning electron micrograph showing a cross section of a template containing isolated nanowires. The foreground shows an empty array of alumina pores with the aluminum electrode at the bottom, and the background displays two hemispheres of nickel overgrowth. The feature at the top of the alumina which may resemble a film is actually a ledge formed during sample preparation.

Figure 6.3: Optical micrograph showing the surface of a template with sparse copper overgrowth on its surface. The area shown is about 2 cm^2.
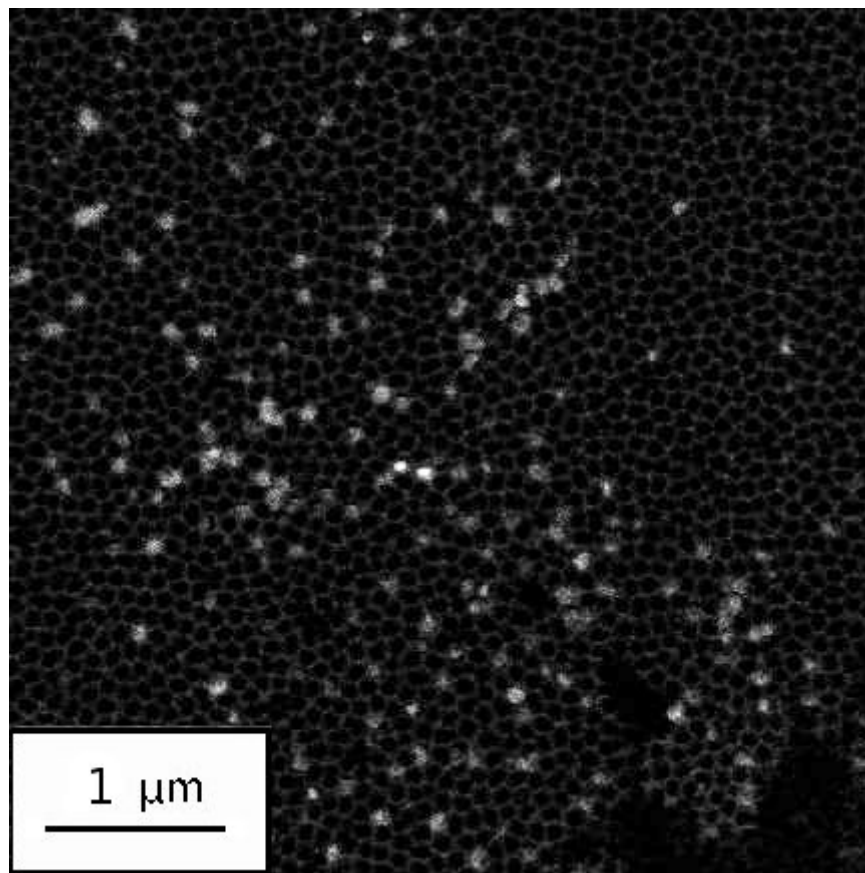
Figure 6.4: Backscattered scanning electron micrograph showing a template containing sparse Cu nanowires viewed from the top side, opposite the electrode. The overgrowth and around a micron of alumina have been polished away mechanically. Light contrast is due to the more massive copper, and the darker honeycomb is the alumina pores. The contrast in this image was linearly enhanced after acquisition.

could be used to synthesize nickel or copper wires. Interestingly, if a template was soaked in nickel or copper deposition solution, it could thereafter be used to synthesize silver wires.

SEM images acquired by etching away the aluminum electrode showed that nucleation was not as sparse as the overgrowth that actually reached the surface, which immediately raised the question of how many wires were actually connected to each spot of overgrowth.

Sample preparation to answer this question using SEM is intractable because any manipulation strong enough to break the alumina would surely break some or all of the wires attached to a particular piece of overgrowth. I decided instead to measure the number of connected wires by measuring their resistance. In order to do this, I first had to establish that the wires were in fact behaving as bulk materials, as would be expected for metals at these scales.

In order to establish that the properties of these nanowires matched those of the bulk, magnetoresistance (MR) measurements of Ni nanowires were acquired. Magnetoresistance
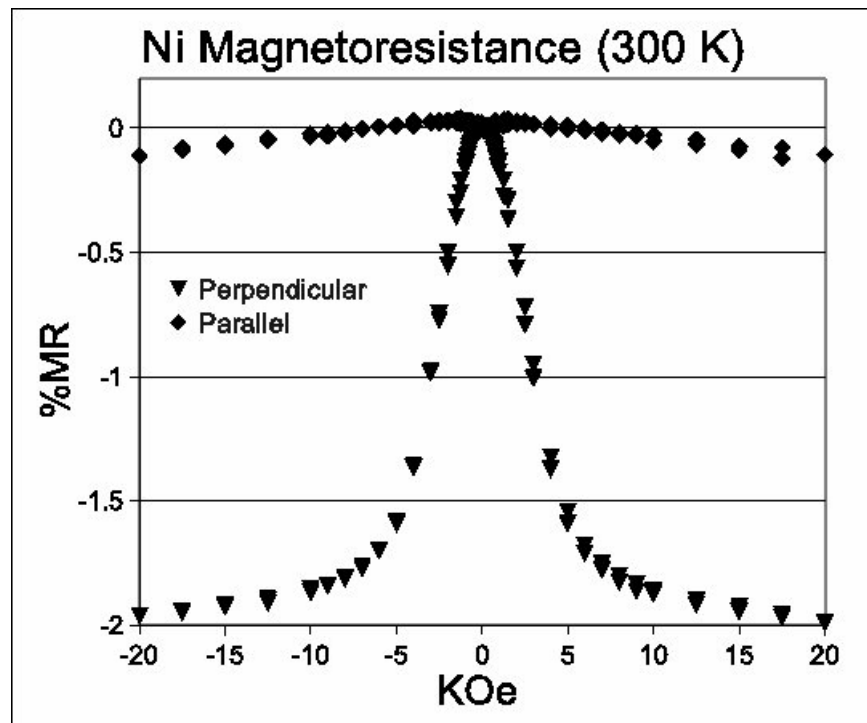
Figure 6.5: Nickel magnetoresistance (MR) measurements showing MR in percent as a function of applied magnetic field in kilo-Orested at 300 K. Diamond data points indicate a magnetic field applied along the wire axis, and triangular data points indicate a magnetic field applied perpendicular to the wire axis. This displays the characteristic anisotropic MR of nickel.
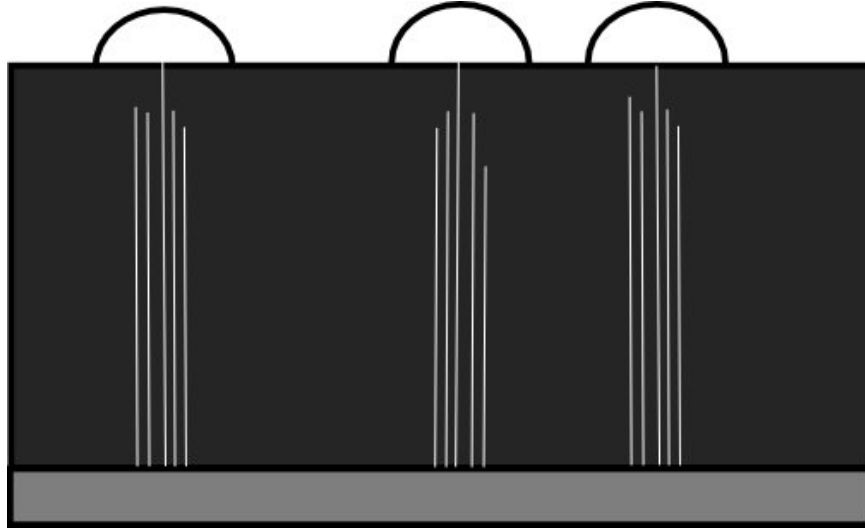
Figure 6.6: Cartoon showing the way nanowires grown using this mechanism are attached after they have overgrown their template.

is a property defined as $(R_H - R_0)/R_0$ * 100% where R_H is the resistance of the sample in an applied magnetic field and R_0 is the resistance in the absence of a magnetic field. This means that MR is an intensive quantity, unaffected by the number of nanowires being contacted. The results shown in Figure 6.5 are consistent with similar measurements in previous work [127], establishing a similar composition in our wires. This corroborates the XRD evidence that indicates the presence of polycrystalline Ni.

Resistance measurements were used to count nanowires and correlate that number with the number of hemispheres contacted. For one typical Ni sample, the template pore dimensions were 75μm length and 35nm diameter. Using the Ni bulk resistivity at 300K of $7.20*10^{-8}$ μm [130], the resistance for each wire can be calculated at 5610 Ω per wire. A sample contacting 52 domes of overgrowth was measured at 300 K to obtain a resistance of 128.4 Ω across the template. This corresponds to roughly 44 contacted wires, indicating that the estimation of one wire per dome is fairly accurate. Fewer wires would be observed due to breakages during sample processing. In any event, it indicates the connection of far fewer wires than are nucleated at the base of the pores. The reasons for this observation beg for explanation.

6.3 Mechanistic Discussion

The observations mentioned above can be used to understand the mechanism of nucleation for these nanostructures. Further, a theoretical examination of deposition rates in the pores and on the surface of the observed hemispheres of overgrowth explains the small number of attached wires.

The spots of overgrowth observed may be attached to one or a small number of wires, as
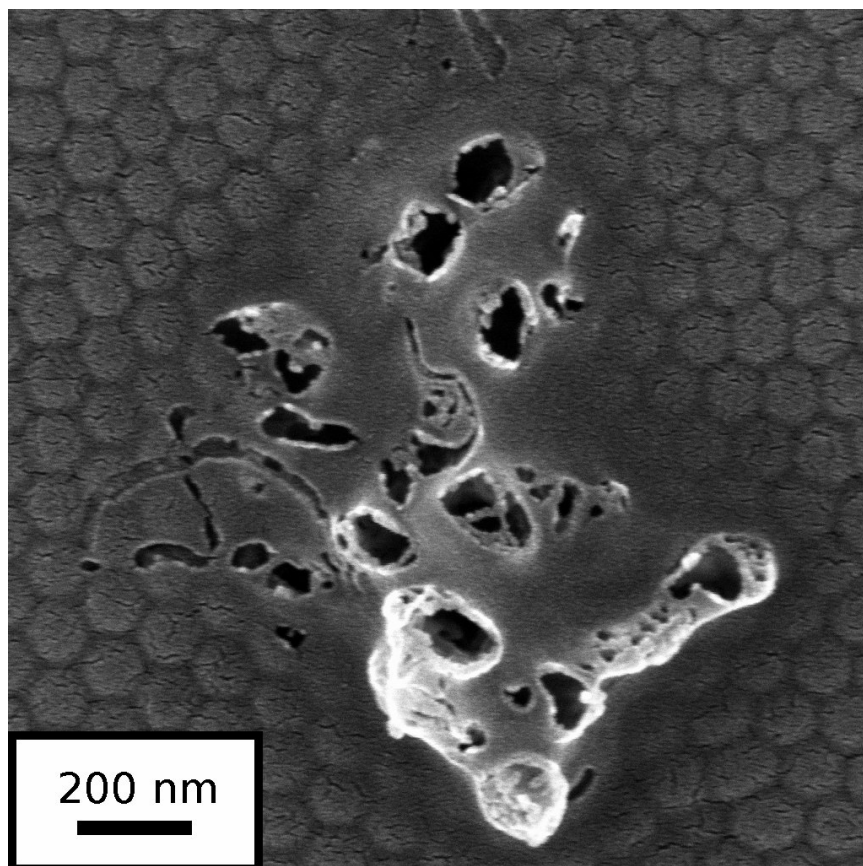
Figure 6.7: Scanning electron micrograph of a porous alumina template looking up from the base of the pores. The template has been treated with mercuric chloride to etch away the aluminum electrode and expose the alumina layer.

is illustrated in the cartoon in Figure 6.6. It is most likely that they are attached to a single wire. The close proximity of growing nanowires illustrated in the cartoon is due to the mechanism by which the wires nucleate at the base of the template. The attachment of one of these wires to a spot of overgrowth is due to the speed of growth of a wire in a template versus that of a hemisphere of overgrowth.

The barrier layer in a given sample of porous alumina is not uniform across its surface. Figure 6.7 displays an example of an imperfection in the barrier layer of a sample of porous alumina. The hexagonal pattern of pores observed apart from the fractured area is typical of the barrier layer across the rest of the sample. The system of holes displayed in Figure 6.7 is an extreme example in that it is readily visible under SEM, and the majority of these holes are mere cracks which nonetheless are enough to expose the aluminum under the barrier layer to whatever solution into which the template might be immersed.

Aluminum has a much lower oxidative potential than most transition metals – it would in fact dissolve in neutral water were it not for the formation of a resistant barrier oxide on its surface as discussed in Chapter 2. This means that bare aluminum exposed to (for example)

a Cu^{2+} ion in solution will thermodynamically favor the reaction

$$2\,Al + 3\,Cu^{2+} \rightarrow 2\,Al^{3+} + 3\,Cu; \qquad \Delta G = -1167 \ kJ/mol \qquad (6.1)$$

The ΔG for a similar reaction with Ni^{2+} is -834 kJ/mol. This means that should the solution get access to the underlying aluminum past the barrier layer, Reaction 6.3 will begin to progress.

In typical deposition solutions, low concentrations of acid are used to ensure the oxides of the metal or metals to be deposited do not precipitate. These low concentrations of acid will not quickly dissolve the alumina template material. However, in places where the alumina layer is exceptionally thin, that is, places where mechanical defects in the barrier layer are present, this acidity will allow the solution access to the bare alumina.

Given that Reaction 6.3 is occurring at the bottom of the pores, Al^{3+} is being locally produced. The stability of soluble aluminum oxides makes Al^{3+} a strong acid, splitting water in order to become a more stable $AlOH^{2+}$ or $Al(OH)_2^+$ species as

$$Al^{3+} + xH_2O \rightarrow Al(OH)_x^{(3-x)+} + xH^+ \qquad (6.2)$$
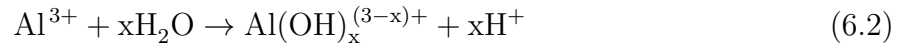
This will locally produce a high enough concentration of acid to cause the dissolution of more alumina, exposing more Al metal to the solution. The overall reaction is the following:

$$2\,Al + Al(OH)_3 + 3\,Cu^{2+} \rightarrow 3\,Al(OH)^{2+} + 3\,Cu; \qquad \Delta G = -697 \ kJ/mol \qquad (6.3)$$
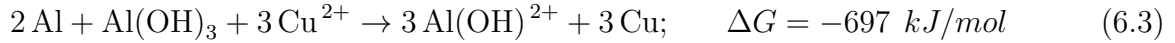
This promotes the formation of deposits of the solution metal etched into the aluminum backing layer at points where the barrier layer is thin. Such deposits can be seen in Figure 6.8.

This mechanism explains the puzzling behavior of silver in this system. Silver does not react with the exposed aluminum as do the copper and nickel ions due to the fact that silver is heavily complexed by SCN^- in its deposition bath, a measure necessary due to the typically very fast rate of silver deposition. However, a template soaked in a nickel or silver deposition solution will form the deposits seen in Figure 6.8, allowing electrical contact between the pore(s) and the aluminum electrode. This same template will then support the growth of silver nanowires.

This nucleation mechanism establishes why there are few wires in any given area, but does not in and of itself imply that single wires are connected to spots of overgrowth. To explain this phenomenon, we must examine the kinetics of electrodeposition down the alumina nanopores compared to the growth rate of overgrowth, which can be taken as a hemisphere of metal grown immersed in the solution.
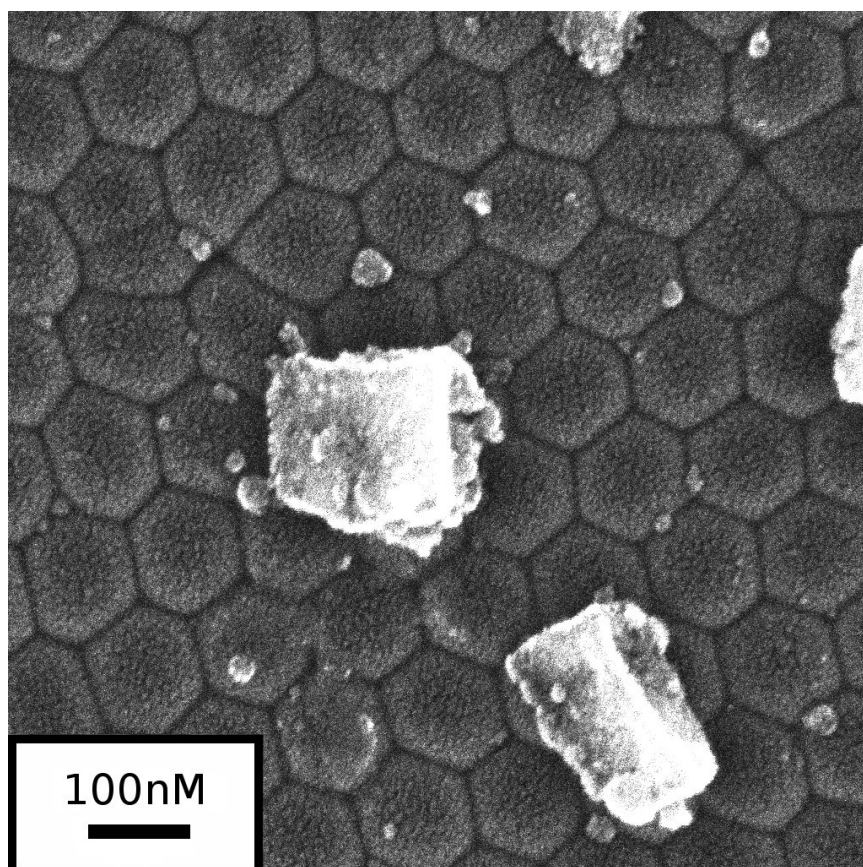
Figure 6.8: Scanning electron micrograph of a porous alumina template looking up from the base of the pores. The template has been first soaked in a solution of $CuSO_4$ and dilute H_2SO_4, then treated with mercuric chloride to etch away the aluminum electrode and expose the alumina layer. The bright nodules are copper, the background roughly hexagonal pattern is the barrier layer.

Due to the constant stirring of the deposition solution, the concentration of M^{2+} (where M is Cu or Ni) can be taken as that of bulk on the surface of the template. Thus, the growth rate of a hemisphere of metal will be proportional to the electron transfer rate. The radius of the hemisphere should grow at a linear rate, since each unit area of the hemisphere will deposit metal at the same rate given a constant $[M^{2+}]$. The growth of wires in the pores is going to be much slower. While stirring constantly renews the concentration of M^{2+} at the surface of the template, solvated species only reach portions of the working electrode at the bottom of the pores through diffusion. This diffusion can be modeled by the linear diffusion equation:

$$\frac{\delta C_{M^{2+}}(x,t)}{\delta t} = D_{M^{2+}} \frac{\delta^2 C_{M^{2+}}(x,t)}{\delta x^2} \tag{6.4}$$

where C_M is the concentration of our solvated metal as a function of x (linear distance from the surface of the electrode) and t (time), and D_M^{2+} is the coefficient of diffusion of our metal. The Cottrell equation is derived from this equation using a Laplace transformation and the imposition of boundary conditions. Since the Cottrell equation provides current as a function of time under potentiostatic conditions, we can use an analogous equation to model the growth rate of a wire in a pore. However, the boundary conditions used here are different than those used to derive the Cottrell equation. First, we can assume that the nanowire growth rate is much lower than the diffusion rate of the species in solution. This means that the concentration profile down the pore will become constant after a few seconds, implying that in steady state

$$\frac{\delta C_{M^{2+}}(x,t)}{\delta t} = 0 \tag{6.5}$$

This implies two other equations of relevance to our discussion. First, plugging this boundary condition into Equation 6.4 we find that

$$D_{M^{2+}} \frac{\delta^2 C_O(x,t)}{\delta x^2} = 0 \tag{6.6}$$

Secondly, with some simple differential calculus on Equation 6.5 we find that $C_{M^{2+}}(x,t)$ is of the form

$$C_{M^{2+}}(x,t) = C_{M^{2+}}(x) = Kx + C \tag{6.7}$$

Where K and C are solution specific constants.

To determine $C_O(x)$, we use two more boundary conditions, namely:

$$C_{M^{2+}}(L, t) = C^*_{M^{2+}} \tag{6.8}$$

$$C_{M^{2+}}(0, t) = 0 \tag{6.9}$$

wherein $C^*_{M^{2+}}$ is the bulk concentration of our metal ion, taken as a constant. Equation 6.8 assumes that the concentration of metal ions at the surface of the template is that of bulk due to convective transport, where L is the distance the metal ions have to diffuse between the growing nanowire and the surface of the template. Equation 6.9 assumes that the current is diffusion limited that is, electron transfer occurs virtually instantaneously. This means that C in equation 6.7 must equal 0, and K equals $C^*_{M^{2+}}$/L, giving us:

$$C_{M^{2+}}(x, t) = \frac{C^*_{M^{2+}}}{L}x \tag{6.10}$$

Since we are assuming diffusion limited current, the current is proportional to the flux at the electrode [64]:

$$i(t) = nFAD_{M^{2+}} \left[\frac{\delta C_{M^{2+}}(x, t)}{\delta x} \right]_{x=0} \tag{6.11}$$

Here n is the number of electrons involved in each reduction reaction, F is the Faraday constant (96485 C/mol), and A is the cross sectional area of a single wire. Combining Equations 6.10 and 6.11 yields:

$$i(t) = \frac{nFAD_{M^{2+}}C^*_{M^{2+}}}{L} \tag{6.12}$$

While L, the distance between the stirred bulk solution and the surface of the depositing metal, can be considered constant on the timescale of diffusion, it does in fact change with time. Specifically, it is related to the current observed as:

$$\frac{d}{dt}L(t) = -ri(t) \tag{6.13}$$

Where r is a collection of constants converting current into linear increase in nanowire length, specifically:

$$r = \frac{m}{nF\rho A} \tag{6.14}$$

where m is the atomic mass of the metal and ρ is the density of the metal. Putting Equations 6.12, 6.13, and 6.14 together gives us the differential equation:

$$\frac{d}{dt}L(t) = \frac{mD_{M^{2+}}C^*_{M^{2+}}}{\rho L(t)} \tag{6.15}$$

This equation can be solved as:

$$L(t) = 2\sqrt{\frac{-mD_{M^{2+}}C^*_{M^{2+}}}{\rho}(t+C)} \tag{6.16}$$

As a final boundary condition, if l is the length of our pores, L(t) equals l at t = 0. If we use this to solve for C we get

$$C = \frac{-l^2\rho}{4mD_{M^{2+}}C^*_{M^{2+}}} \tag{6.17}$$

Finally, observing that wire length is equal to l-L(t), we can obtain the expression for wire length as a function of time ($\Lambda(t)$):

$$\Lambda(t) = l - 2\sqrt{\frac{-mD_{M^{2+}}C^*_{M^{2+}}}{\rho}\left(t - \frac{l^2\rho}{4mD_{M^{2+}}C^*_{M^{2+}}}\right)} \tag{6.18}$$

Thus, it can be seen that the rate of growth of nanowires increases as they near the surface of the template, thus increasing any initial disparity in length or nucleation time. Once the nanowire protrudes beyond the surface of the template (and in fact a bit before) the deposition is no longer diffusion controlled, but is instead the electron transfer is the limiting step of the reaction. The current due to the rate limiting transfer of a single electron [64] is:

$$i = FAk^0\left[C_O(0,t)e^{-\alpha\frac{F}{RT}(E-E^{0\prime})} - C_R(0,t)e^{(1-\alpha\frac{F}{RT}(E-E^{0\prime}))}\right] \tag{6.19}$$

Here, k^0 is the standard rate constant of the reaction, R is the ideal gas constant, T is temperature, E is the relative energy at the electrode, $E^{0\prime}$ is the equilibrium potential of the reaction, and α is the transfer coefficient. Our reaction has $C_R = 1$ (since the reduced form is a solid metal) and $C_O = C^*_{M^{2+}}$ (as per the boundary condition dictated by convective mass transport). If we assume that the reaction is irreversible, however, we can treat the reduction as a mass sink and set $C_R = 0$. Our equation and its time dependence can now

be simplified to:

$$i(t) = FA(t)k^0 \left[C_{M2+}^* e^{-\alpha \frac{F}{RT}(E - E^{\circ\prime})} \right] \tag{6.20}$$

In a typical potentiostatic experiment, E and T will be constant, so the terms in the bracket can be treated as a constant. The volume can be related to the current analogously to Equation 6.13:

$$\frac{d}{dt}V(t) = \mathbf{r}i(t) \tag{6.21}$$

where

$$\mathbf{r} = \frac{m}{F\rho} \tag{6.22}$$

Volume and surface area can be related to the radius of the hemisphere by

$$V(t) = \frac{2}{3}\pi r^3(t) \tag{6.23}$$

and

$$A(t) = 2\pi r^2(t) \tag{6.24}$$

respectively. If we combine equations 6.20 and 6.24, we obtain

$$\frac{d}{dt}\pi r^3(t) = \frac{2\pi k^0 \left[C_{M2+}^* e^{-\alpha \frac{F}{RT}(E - E^{0\prime})} \right]}{\rho} r^2 t \tag{6.25}$$

After simplifying and solving the differential equation, we obtain

$$r(t) = \frac{m k^0 \left[C_{M2+}^* e^{-\alpha \frac{F}{RT}(E - E^{0\prime})} \right]}{\rho} t \tag{6.26}$$

To compare the rates of growth we should look at the two derivatives.

$$\frac{d}{dt}r(t) = \frac{m k^0 C_{M2+}^* e^{-\alpha \frac{F}{RT}(E - E^{0\prime})}}{\rho} \tag{6.27}$$

$$\frac{d}{dt}\Lambda(t) = \frac{mD_{M^{2+}}C^*_{M^{2+}}}{\rho}\left[\frac{-mD_{M^{2+}}C^*_{M^{2+}}}{\rho}\left(t - \frac{l^2\rho}{4mD_{M^{2+}}C^*_{M^{2+}}}\right)\right]^{-\frac{1}{2}} \tag{6.28}$$

If we are comparing two wires near the surface, one of which is one second behind the other, t in Equation 6.27 = 1 and the t-K term in Equation 6.28 = -1. In the second it would take the other wire to break the surface, the radius of the wire which has already broken the surface will increase by

$$\frac{mk^0 C^*_{M^{2+}} e^{-\alpha\frac{F}{RT}(E-E^{0\prime})}}{\rho} \tag{6.29}$$

If we assume that $E = E^0$ (since we're trying to deposit, this is the least cathodic potential that we would reasonably apply) then our rate becomes

$$\frac{mk^0 C^*_{M^{2+}}}{\rho} \tag{6.30}$$

To perform this calculation for an example nickel solution, we have m = 58.69 g/mol, $C_{M^{2+}}$ = 0.776 mol/L, and ρ = 8.908 g/cm³. We will assume a k^0 of 10^{-10} cm/sec [131]. Even this low rate constant gives a radial increase rate of 5 nanometers per second. Since the separation of pore centers on the surface of the template is on the order of 70 nanometers, another ring of neighboring pores will be occluded every 14 seconds, a short time on the scale of an hour-long deposition. This rate will only hold as long as the concentration of metal ion at the surface of the growing hemisphere of overgrowth remains constant, and will eventually be limited by the convection rate of the solution. However, this situation will even more severely retard the growth of wires still embedded in pores.

Given our recently established determination that the deposition rate down the pore accelerates with increasing wire length, very small differences in nucleation time or random variations in growth due to pore restriction will produce large changes the time at which overgrowth will be achieved. This makes it unlikely that two wires will reach the surface close enough together that the overgrowth of one does not quickly occlude the pore of the other. Thus this rate analysis provides a good explanation for the the very low number of observed electrical connections of wires to overgrowth despite the larger number of nucleated wires.

6.4 Conclusions

Isolated nanowires with macroscopic contact points at both ends of their length can be synthesized in porous alumina templates with unetched barrier layers by depositing wires

from acidic solutions after a long soak time. Sparse nickel and copper arrays have been synthesized directly using this method, and silver arrays have been synthesized in a two step process. The extreme sparseness of the nanowires in the template may be exploited in order to obtain transport measurements using tractable macroscopic contacts. Such measurements on nanowires of nickel and copper were performed to confirm the hypothesized wire density in the array.

Should a similar measurement of an arbitrary compound be desired, it first must have an established electrochemical synthesis. Once this hard part is taken care of, the isolated wire deposition can be started by soaking a newly created alumina template in an aqueous solution of 120 g/L $NiSO_4$ and 45 g/L HBO_3 for at least an hour. Nickel is suggested because its lower number of nucleation sites makes it more tractable for contacting. After this step, the electrochemical synthesis can be employed until overgrowth appears. Unless the compound has very unusual overgrowth characteristics it should display the same pore-occlusion behavior as the two examined metals. From this point, contacts can be formed with the overgrowth and the alumina electrode for transport measurements.

Chapter 7

Conclusions

Electrochemical studies were undertaken for two candidate solutions for the electrodeposition of metal sulfides. Systems of iron(II) sulfide, copper(II) sulfide and sodium thiosulfate were examined and their suitability for the electrochemical synthesis of FeS_2 and Cu_xS, respectively, was evaluated. Additionally, an unusual result involving the electrodeposition of metal nanowires into porous alumina templates was investigated.

The $FeSO_4$–$Na_2S_2O_3$ system was found to be unsuitable for the electrodeposition of pyrite. FeS is produced at high rates, but the necessary coordination of Fe(II) and two S(-I) ions is not offered by the chemistry of this solution at the electrode. Based on these observations, the electrodeposition of FeS_2 will be intractable unless either a two-atom sulfur anion source is used or a multi-step process is employed in which FeS is synthesized, followed by a conversion to FeS_2. It may be possible to undertake this conversion under solution conditions rather than the annealing methods which have been employed in the literature.

The $CuSO_4$–$Na_2S_2O_3$ system was found to be suitable for the electrodeposition of Cu_xS. High concentrations of thiosulfate are required in order for copper sulfide to be deposited rather than metallic copper. The high affinity of thiosulfate to Cu(I) was found to be essential to the deposition process. At high thiosulfate concentrations, the deposition of Cu metal was completely suppressed. For future use of this system as an electrodeposition bath, it is suggested that thiosulfate concentration be used as the primary tuning parameter. The electrodeposition should take place at potentials below -0.5 V vs. Ag / AgCl and the stoichiometry of the resultant deposit is likely to be highly dependent on relative thiosulfate concentration.

The mechanism behind the formation of isolated nanowire groups deposited in porous alumina templates has been detailed. Aluminum exposed at the base of a small number of pores to a solution of certain metals will result in a redox reaction promoting the dissolution of the barrier layer and the formation of a small plug of metal at the base of the affected pores. When wires are subsequently electrodeposited into the template, they further isolate themselves due to rate competition between those wires growing into the template and the

blossoming overgrowth on the surface. This geometry can be exploited to obtain transport measurements of known numbers of *in situ* nanowires through the use of macroscopic contacts.

Bibliography

[1] *Reference Solar Spectral Irradiance: Air Mass 1.5* (American Society for Testing and Materials, West Conshohocken, Pennsylvania, USA, 2009).

[2] I. Puigdomenech, Make Equilibrium Diagrams Using Sophisticated Algorithms, Computer Software, 2010.

[3] T. A. Green and S. Roy, Journal of the Electrchemical Society **153**, C157 (2006).

[4] W. A. Pryor, *Mechanisms of Sulfur Reactions* (McGraw-Hill, New York, New York, 1962).

[5] I. R. Wilson, in *Comprehensive Chemical Kinetics*, edited by C. H. Bamford and C. F. H. Tipper (Elsevier, 335 Jan van Galenstraat, Amsterdam, The Netherlands, 1972), Vol. 6, pp. 336–367.

[6] C. A. S. Brevett and D. C. Johnson, Journal of the Electrochemical Society **139**, 1314 (1992).

[7] N. N. Greenwood and A. Earnshaw, *Chemistry of the Elements*, 2nd ed. (Butterworth-Heinemann, Woburn, MA, 1997).

[8] M. A. Vairavamurthy and W. Zhou, *ACS Symposium Series* (American Chemical Society, Washington, DC, 1995), Vol. 612, pp. 280–291.

[9] H. Miki, M. Nicol, and L. Velásquez-Yévenes, Hydrometallurgy **105**, 321 (2011).

[10] J. Brierley and C. Brierley, Hydrometallurgy **59**, 233 (2001).

[11] G. B. Haxel, J. B. Hedrick, and G. J. Orris, in *Rare Earth Elements - Critical Resources for High Technology*, edited by P. H. Stauffer and J. W. H. II (U.S. Geological Survey, U.S. Department of the Interior, 2002).

[12] A. Ennaoui, S. Fiechter, W. Jaegermann, and H. Tributsch, Journal of the Electrochemical Society **133**, 97 (1986).

[13] J. H. Delliginer, F. W. Grover, C. M. Smith, G. F. Wittig, A. D. Cole, L. P. Wheeler, and H. M. Royal, *The Principles Underlying Radio Communication* (Signal Corps, U. S. Army, Washington D.C., 1918), No. 40.

[14] V. Livshits, A. Blum, E. Strauss, G. Ardel, D. Golodnitsky, and E. Peled, Journal of Power Sources **97-98**, 782 (2001).

[15] A. Ennaoui, S. Fiechter, C. Pettenkofer, N. Alonso-Vante, K. Bilker, M. Bronold, C. Hopfner, and H. Tributsch, Solar Energy Materials and Solar Cells **29**, 289 (1993).

[16] C. Wadia, A. P. Alivisatos, and D. M. Kammen, Environmental Science and Technology **43**, 2072 (2009).

[17] J. A. Bragagnolo, A. M. Barnett, J. E. Phillips, R. B. Hall, A. Rothwarf, and J. D. Meakin, IEEE Transaction on Electron Devices **27**, 645 (1980).

[18] Y. Wu, C. Wadia, W. Ma, B. Sadtler, and A. P. Alivisatos, Nano Letters **8**, 2551 (2008).

[19] A.-E. Becquerel, Comptes rendus de l'Acadmie des Sciences **9**, 561 (1839).

[20] C. Fritts, Proceedings of the American Association for the Advancement of Science **33**, 97 (1883).

[21] R. S. Ohl, Light-Sensitive Electric Device, 1946.

[22] *Handbook of Photovoltaic Science and Engineering*, edited by A. Luque and S. Hegedus (John Wiley & Sons, Inc., West Sussex, England, 2003).

[23] E. Maruyama, A. Terakawa, M. Taguchi, Y. Yoshimine, D. Ide, T. Baba, M. Shima, H. Sakata, and M. Tanaka, in *Conference Record of the 2006 IEEE 4th World Conference on Photovoltaic Energy Conversion* (Institute of Electrical and Electronics Engineers, New York, 2006), pp. 1455–1460.

[24] *Power Technologies Energy Data Book*, 3 ed., edited by J. Aabakken (NREL, U.S. Department of Energy, Oak Ridge, TN, 2005).

[25] *Trends in Photovoltaic Applications: Survey report of selected IEA countries between 1992 and 2006*, edited by S. Nowak (International Energy Agency, Switzerland, 2007).

[26] *Energy in Sweden - facts and figures 2010*, edited by H. Lindblom (Swedish Energy Agency, Kungsgatan 43, P.O. Box 310, SE-631 04 Eskilstuna, 2010).

[27] *Solar Power and the Electric Grid*, edited by C. Turchi (National Renewable Energy Laboratory, 1617 Cole Boulevard, Golden, Colorado, 2010).

[28] M. Ito, K. Kato, K. Komoto, T. Kichimi, and K. Kurokawa, Progress in Photovoltaics: Research and Applications **16**, 17 (2007).

[29] H. Ullal and B. von Roedern, *22nd European Photovoltaic Solar Energy Conference (PVSEC) and Exhibition* (NREL, Milan, Italy, 2007).

[30] P. P. Altermatt, T. Kiesewetter, K. Ellmer, and H. Tributsch, Solar Energy Materials & Solar Cells **71**, 181 (2002).

[31] D. C. Reynolds, G. Leies, L. L. Antes, and R. E. Marburger, Physics Reviews **96**, 533 (1954).

[32] E. R. Hill and B. G. Keramidas, IEEE Transactions on Electron Devices **ED-14**, 22 (1967).

[33] A. L. Fahrenbruch and R. H. Bube, *Fundamentals of Solar Cells: Photovoltaic Solar Energy Conversion* (Academic Press, 111 Fifth Avenue, New York, New York 10003, 1983).

[34] F. Pfisterer, Thin Solid Films **431**, 470 (2003).

[35] E. H. Roseboom, Economic Geology **61**, 641 (1966).

[36] J. Dieleman, in *International workshop on cadmium sulfide solar cells and other abrupt heterojunctions*, edited by K. W. Böer and J. D. Meakin (Delaware University, Newark, NJ, 1975), p. 92.

[37] T. S. Te Velde and J. Dieleman, Philips Research Reports **28**, 573 (1973).

[38] S. Bagula, S. Chavhan, and R. Sharma, Journal of Physics and Chemistry of Solids **68**, 1623 (2007).

[39] Y. Lu, S. Liang, M. Chen, and J. Jia, Journal of Colloid and Interface Science **332**, 32 (2009).

[40] G. Yu, J. Gao, C. Hummelen, F. Wudl, and A. J. Heeger, Science **270**, 1789 (1995).

[41] B. M. Kayes, H. A. Atwater, and N. S. Lewis, Journal of Applied Physics **97**, 114302 (2005).

[42] BCS, *U.S. Energy Requirements for Aluminum Production Historical Perspective, Theoretical Limits and Current Practices* (Industrial Technologies Program, U.S. Department of Energy, 2007).

[43] M. Pasquale, L. Gassa, and A. Arvia, Electrochimica Acta **53**, 5891 (2008).

[44] S. Díaz, O. Mattos, O. Barcia, and F. J. F. Miranda, Electrochemica Acta **47**, 4091 (2002).

[45] M. Cortés, S. Matencio, E. Gómez, and E. Vallés, Journal of Electroanalytical Chemistry **627**, 69 (2009).

[46] C. P. Chan, H. Lam, K. K. Leung, and C. Surya, Journal of Nonlinear Optical Physics & Materials **18**, 599 (2009).

[47] W. F. Hall and A. R. Chaudhuri, in *Proceedings of the AES 10th Plating in the Electronics Industry Symposium* (American Electroplating Society, San Francisco, CA, 1983).

[48] C. R. Martin, Science **266**, 1961 (1994).

[49] H. Zhang, G. Q. Yang, R. G. Zhang, B. Y. Yang, and L. Wei, Journal of Inorganic Materials **20**, 1337 (2005).

[50] Y. Z. Dong, Y. F. Zheng, X. G. Zhang, H. Duan, Y. F. Sun, and Y. H. Chen, Science in China Series E - Engineering & Materials Science **48**, 601 (2005).

[51] D. Wan, Y. Wang, Z. Zhou, G. Yang, B. Wang, and L. Wei, Materials Science & Engineering B **122**, 156 (2005).

[52] A. Gomes, J. R. Ares, I. J. Ferrer, M. I. da Silva Pereira, and C. Sánchez, Materials Research Bulletin **38**, 1123 (2003).

[53] A. Gomes, M. H. Mendonca, M. I. da Silva Pereira, and F. M. Costa, Journal of Solid State Electrochemistry **4**, 168 (2000).

[54] S. Nakamura and A. Yamamoto, Solar Energy Materials & Solar Cells **65**, 79 (2001).

[55] A. S. Aricó, V. Antonucci, P. L. Antonucci, D. L. Cocke, and N. Giordano, Electrochimica Acta **36**, 581 (1991).

[56] N. R. de Tacconi, O. Medvedko, and K. Rajeshwar, Journal of Electroanalytical Chemistry **379**, 545 (1994).

[57] K. Anuar, Z. Zainal, M. Hussein, N. Saravanan, and I. Haslina, Solar Energy Materials & Solar Cells **73**, 351 (2002).

[58] C. Lai, Q. Wu, J. Chen, L. Wen, and S. Ren, Nanotechnology **21**, 215602 (2010).

[59] A. Ghahremaninezhad, E. Asselin, and D. Dixon, Electrochemistry Communications **13**, 12 (2011).

[60] T. Yukawa, K. Kuwabara, and K. Koumoto, Thin Solid Films **280**, 160 (1996).

[61] I. Grozdanov, C. K. Barlingay, S. K. Dey, M. Ristov, and M. Najdoski, Thin Solid Films **250**, 67 (1994).

[62] M. Pourbaix, Ph.D. thesis, University of Brussels, 1939.

[63] CRC Handbook of Chemistry and Physics, 91st edition, 2011.

[64] A. J. Bard and L. R. Faulkner, *Electrochemical Methods: Fundamentals and Applications*, 2nd ed. (John Wiley & Sons, Inc., 111 River Street, Hoboken, NJ, 07030, 2001).

[65] G. Carter, Journal of Physics D: Applied Physics **34**, R1 (2001).

[66] K. Heo, C.-J. Kim, M.-H. Jo, and S. Hong, Journal of Materials Chemistry **19**, 901 (2009).

[67] C.-C. Chen, C.-G. Kuo, and C.-G. Chao, Japanese Journal of Applied Physics **44**, 1524 (2005).

[68] J. W. Diggle, T. C. Downie, and C. W. Goulding, Chemical Reviews **69**, 365405 (1969).

[69] G. E. Thompson, Thin Solid Films **297**, 192 (1997).

[70] A. P. Li, F. Müller, A. Birner, K. Nielsch, and U. Gösele, Journal of Applied Physics **84**, 6023 (1998).

[71] G. K. Singh, A. A. Golovin, I. S. Aranson, and V. M. Vinokur, Europhysics Letters **70**, 836 (2005).

[72] Z. Su and W. Zhou, Advanced Materials **20**, 3663 (2008).

[73] J. E. Houser and K. R. Hebert, Nature Materials **8**, 415 (2009).

[74] H. Masuda and M. Satoh, Japanese Joural of Applied Physics **35**, 126 (1996).

[75] D. Routkevitch, T. Bigioni, M. Moskovits, and J. M. Xu, Journal of Physical Chemistry **100**, 14037 (1996).

[76] J. W. Morgan and E. Anders, Proceedings of the National Acadamy of Sciences, USA **77**, 6973 (1980).

[77] L. Suidan, J. K. Badenhoop, E. D. Glendening, and F. Weinhold, Journal of Chemistry Education **72**, 583 (1995).

[78] D. W. J. Cruickshank and B. C. Webster, in *Inorganic Sulphur Chemistry*, edited by G. Nickless (Elsevier, 335 Jan van Galenstraat, Amsterdam, The Netherlands, 1968), pp. 7–48.

[79] D. Lyons and G. Nickless, in *Inorganic Sulphur Chemistry*, edited by G. Nickless (Elsevier, 335 Jan van Galenstraat, Amsterdam, The Netherlands, 1968), pp. 509–533.

[80] A. Vairavamurthy, B. Manowitz, G. L. III, and Y. Jeon, Geochemica et Cosmochemica Acta **57**, 1619 (1993).

[81] I.-H. Yeo and D. C. Johnson, Journal of the Electrochemical Society **134**, 1973 (1987).

[82] J. M. Akagi, in *Sulfate-Reducing Bacteria*, Vol. 8 of *Biotechnology Handbooks*, edited by L. L. Barton (Plenum Press, New York, New York, 1995), pp. 89–109.

[83] R. W. Carlson, M. S. Anderson, R. E. Johnson, M. B. Schulman, and A. H. Yavrouian, Icarus **157**, 456 (2002).

[84] E. A. Paul, T. H. Batten, M. A. May, W. R. Sayers, P. E. Shelton, T. Kojima, and V. Katovic, Inorganic Chemistry **33**, 630 (1994).

[85] R. A. Berner, Journal of Sedimentary Petrology **51**, 359 (1981).

[86] V. P. Gladishev, Zavodskaya Laboratoriya **28**, 1063 (1962).

[87] L. Szekeres, Talanta **21**, 1 (1974).

[88] K. W. C. Burton and P. Machmer, in *Inorganic Sulphur Chemistry*, edited by G. Nickless (Elsevier, 335 Jan van Galenstraat, Amsterdam, The Netherlands, 1968), pp. 337–366.

[89] H. Ma, X. Cheng, G. Li, S. Chen, Z. Quan, S. Zhao, and L. Niu, Corrosion Science **42**, 1669 (2000).

[90] E. M. Arce and I. González, International Journal of Minerals Processing **67**, 17 (2002).

[91] A. Mcauley, Coordination Chemistry Reviews **5**, 245 (1970).

[92] S. Díaz, J. Calderón, O. Barcia, and O. Mattos, Electrochemica Acta **53**, 7426 (2008).

[93] M. Matlosz, Journal of the Electrochemical Society **140**, 2272 (1993).

[94] J.-P. Diard, P. Landaud, B. L. Gorrec, and C. Montella, Journal of Electroanaytical Chemistry **255**, 1 (1988).

[95] D. W. Shoesmith, P. Taylor, M. G. Bailey, and B. Ikeda, Electrochemica Acta **23**, 903 (1978).

[96] E. Hansson, M. Odziemkowski, and R. Gillham, Corrosion Science **48**, 3767 (2006).

[97] A. Hernández-Espejel, M. Palomar-Pardavé, R. Cabrera-Sierra, M. Romero-Romo, M. T. Ramírez-Silva, and E. M. Arce-Estrada, Journal of Physical Chemistry B **115**, 1833 (2011).

[98] J. Vera, S. Kapusta, and N. Hackerman, Journal of the Electrochemical Society **133**, 461 (1986).

[99] H. H. Pohl, Journal of Chemical and Engineering Data **7**, 295 (1962).

[100] F. M. Page, Transactions of the Faraday Society **49**, 635 (1953).

[101] P. W. Crawford and M. D. Ryan, Inorganica Chimica Acta **328**, 13 (2002).

[102] K. Winkler and T. Krogulec, Journal of Electroanalytical Chemistry **386**, 127 (1995).

[103] E. Itabashi, Journal of Electroanalytical Chemistry **103**, 189 (1979).

[104] E. Bura-Nakić, D. Krznarić, G. R. Helz, and I. Ciglenečki, Electroanalysis **22**, 1 (2011).

[105] D. Krznarić and I. Ciglenečki-Jusić, Electroanalysis **17**, 1317 (2005).

[106] E. Najdeker and E. Bishop, Electroanalytical Chemistry and Interfacial Electrochemistry **41**, 79 (1973).

[107] N. Ramasubramanian, Journal of Electroanalytical Chemistry **64**, 21 (1975).

[108] K. Winkler and T. Krogulec, Electrochimica Acta **30**, 1055 (1985).

[109] K. Winkler, S. Kalinowski, and T. Krogulec, Journal of Electroanalytical Chemistry **252**, 303 (1988).

[110] J. O. Bockris and M. Enyo, Transactions of the Faraday Society **58**, 1187 (1962).

[111] O. R. Brown and H. R. Thirsk, Electrochimica Acta **10**, 383 (1965).

[112] K. J. Powell, P. L. Brown, R. H. Byrne, T. Gajda, G. Hefter, S. Stöberg, and H. Wanner, Pure Applied Chemistry **79**, 895 (2007).

[113] A. E. Martell and R. M. Smith, *NIST Standard Reference Database 46 Version 2.0* (National Institute of Standards and Technology, College Station, TX, 1995).

[114] M. W. Breiter, Transactions of the Faraday Society **65**, 22006 (1969).

[115] D. Margheritis, R. C. Salvarezza, M. C. Giordano, and A. J. Arvia, Journal of Electroanalytical Chemistry **229**, 327 (1987).

[116] L. J. Brogan and A. M. Stacy, Materials Letters **64**, 1674 (2010).

[117] H. Ruda, J. Salfi, U. Philipose, A. Saxena, K. Lau, T. Xu, L. Zhong, C. Souza, S. Aouba, S. Yang, P. Sun, S. Nair, and C. Fernandes, Journal of Materials Science: Materials in Electronics **20**, 480 (2009).

[118] J. Weber, R. Singhai, S. Zekri, and A. Kumar, International Materials Reviews **53**, 235 (2008).

[119] Z. L. Wang, P. Poncharal, and W. A. de Heer, Microscopy and Microanalysis **6**, 224 (2000).

[120] A. Pfunda, I. Shorubalkoa, R. Leturcqa, M. T. Borgströmb, F. Gramma, E. Müllera, and K. Ensslin, Chima **60**, 729 (2006).

[121] Z. Hackney, L. Mair, K. Skinner, and S. Washburn, Materials Letters **64**, 2016 (2010).

[122] J. Lee, Y. Kim, L. Cagnon, U. Gösele, J. Lee, and K. Nielsch, Physica Status Solidi **4**, 43 (2010).

[123] R. Lin, M. Bammerlin, O. Hansen, R. R. Schlittler, and P. Bøggild, Nanotechnology **15**, 1363 (2004).

[124] J. H. Seol, A. L. Moore, L. Shi, I. Jo, and Z. Yao, Journal of Heat Transfer **133**, 022403 (2011).

[125] S. Bhattacharyya, A. Gabashvili, N. Perkas, and A. Gedanken, Journal of Physical Chemistry C **111**, 11161 (2007).

[126] Q. Wan, T. H. Wang, and C. L. Lin, Nanotechnology **14**, I.15 (2003).

[127] T. Oghai, L. Gravier, X. Hoffer, M. Lindeberg, K. Hjort, R. Spohr, and J.-P. Ansermet, Journal of Physics D: Applied Physics **36**, 3109 (2003).

[128] H. Cao, L. Wang, Y. Qiu, and L. Zhang, Nanotechnology **17**, 1736 (2006).

[129] G. Riveros, S. Green, A. Cortes, H. Gomez, R. E. Marotti, and E. A. Dalchiele, Nanotechnology **17**, 561 (2006).

[130] *CRC Handbook of Chemistry and Physics*, 89 ed., edited by D. R. Lide (CRC Press, Boca Raton, FL, 2009), pp. 12–40.

[131] J. R. Vilche and A. J. Arvia, Corrosion Science **15**, 419 (1975).

Appendix A

Appendix

A.1 LabView Programs

In an effort to aid in the production of new potentiostat control programs and to help espouse good coding practices in our group, I have included as an appendix to this thesis the LabView code I have programmed along with explanations. Hopefully these will prove an aid to budding LabView coders attempting to modify our current instrumentation.

The potentiostats and the original LabView code (of which much yet survives) are the legacy of former group member Evan Hajime, who collaborated with Henry Chan in the department electronics shop for the hardware and who was helped by Jenny Keyani and Keith Leung. He created a pamphlet explaining the hardware and I/O scheme for the potentiostat cards which is kept next to the moniter serving the poteniostat computers. This pamphlet also documents the operation of the programs he created. Since I have reorganized and recreated a number of these programs, I am using this opportunity to document the code to allow use, modification, and (if needed) repair.

There are a few full VI programs used to perform different experiments on the potentiostats, and their sub-VIs and operation are explained below before a more in-depth look at each program's code. Since a uniquely addressed but otherwise identical program exists for each potentiostat on a computer, I will use X to refer to the letter of the potentiostat in question.

A.1.1 PStat X Constant (A.2.1)

PStat X Constant was first programmed by Evan Hajime as one of the original programs for use with the homemade potentiostats. I have since modified it, making it more organized, easier to use and modify further, and making inputs behave more predictably.

PStat X Constant applies a constant voltage or current at the working electrode, measured versus the reference electrode for a set period of time. During this period the program will track both current and voltage, saving each as a function of time on an .xls spreadsheet to the harddrive. The program will also collect the OCP of the solution before the experiment is begun, also saving this record as another .xls spreadsheet.

Operation:

The program will automatically run when it is opened, but no information is sent to the potentiostat. There are two tabs at the top of the program, "Setup" and "Start Expt." The "Setup" tab is open first, and contains all of the initialization parameters required. The "Start Expt." tab is used to start the experiment, and has a virtual output window showing the real time current and voltage readings from the experiment if one is in progress.

The parameters for the experiment should first be input in to the Setup tab. Once the parameters are correct, the power to the PStat box but NOT the cell should be turned on, and the Collect OCP button pressed. This will bring up a file save dialogue which will determine the name of the .xls sheet created to store the OCP data. The OCP collection will begin running after the file is created - if parameters are changed after OCP collection has started, they will NOT be used by the program.

Once the OCP has stabilized to the user's satisfaction (if the user cares) the experiment may be started by switching to the Start Expt. tab and clicking the Start button.[1] This brings up another file creation dialog, this one to create a .xls sheet to hold the data generated during the experiement. BEFORE the file name is sent, the cell must be physically switched on, otherwise no voltage or current will be applied once the program starts. After the file name is sent, the experiment will run until it is aborted due to an error, aborted by a user clicking the Stop button, or the time specified in the Setup tab has elapsed. A popup detailing the reason that the experiment has stopped will appear once the experiment is over.

Controls (Setup):

Potentiostat/Galvanostat Select: Toggle switch puts potentiostat into galvanostatic or potentiostatic mode.

Current Range Select: Toggle switch changes the potentiostat's current handling from 0-100 mA to 0-10 mA. 10 V is in all cases the highest voltage safely used.

Current Range (mA): Smaller ranges give higher resolution for current values obtained after analog to digital conversion.

Voltage Range (V): Smaller ranges give higher resolution for voltage values obtained after

---

[1]Note that the Ready button which appears on the start tab once the OCP is being collected is a non-functional legacy of the original version of the program. It was left there due to the fact that other group members had learned to click it by rote and were uncomfortable with its absence. You can click it if you want... it doesn't do anything.

analog to digital conversion.

Overvoltage Limit (V): If the absolute value of the voltage ever exceeds this number, the VI will automatically abort the run.

Overcurrent Limit (mA): If the absolute value of the current ever exceeds this number, the VI will automatically abort the run.

Output Range (V or mA): Smaller ranges give higher resolution for the output voltage or current values obtained after digital to analogue conversion.

Applied Voltage (V) / Current (mA): The voltage or current to be applied to the working electrode relative to the reference electrode. Negative voltages or currents causes the WE to accept electrons from solution.

Total Time (sec): The total length of time for the eperiment to run.

Sampling Time (sec/sample): The length of time between the acquisition of individual voltage / current samples - along with Total Time, this directly determines the size of the data file created.

Final Resting Voltage (V) / Current (mA): The voltage or current which is applied at the end of the experiment and will continue to be applied after the program has been stopped. The cell must be turned off at the PStat module in order to cease the application of this voltage.

Collect OCP: This button starts the collection of the OCP. Once this button has been pressed, changing the toggle switches will not alter the experiment.

Controls (Start Expt.):

Start: This button stops the collection of the OCP and opens the dialogue to save the data generated by the experiment. Once a filename is input for the spreadsheet, the experiment will start.

Stop: This button will immediately abort an experiment in progress.

Outputs (Setup):

Elapsed Time (sec): The elapsed time of the open circuit potential measurement.

Open Circuit Potential (V): This is an averaged OCP calculated from a running average of the last few data points measured.

Real-time Chart: This is the main chart on the Setup tab. It outputs the last three points of the OCP voltage measurement, which is the voltage difference between the reference and working electrodes.

Outputs (Start Expt.):

Total Time (sec): The amount of time input in the Total Time control of the Setup tab.

Elapsed Time (sec): The amount of time that has passed since the experiment was started.

Time Remaining (sec): Total Time - Elapsed Time.

Voltage (V): Last measured voltage (positive is a relatively oxidizing potential at the working electrode).

Current (mA): Last measured current (positive is oxidizing at the working electrode.)

Real-time Chart: Plot of measured voltage and current vs. time.

Voltage Overload: This provides feedback if an experiement has been ended due to a voltage overload. If the lamp is illuminated, this is the reason for the end of the experiment.

Current Overload: This provides feedback if an experiement has been ended due to a current overload. If the lamp is illuminated, this is the reason for the end of the experiment.

A.1.2 PStat X - CV (A.2.2)

This program been modified from the original version which Evan Hajime programmed, but only to clean up the code and allow the more predictable assignment of a few variables.

This program is used for the generation of cyclic voltammetric (CV) data. The program will run a number of saw-tooth triangular wave form time/voltage cycles between two set potentials, collecting both the current and voltage data during the experiment. The direction of the scan can be changed by inverting the order of the set points, and the rate of scan, the pre-cycle sit time and potential (so charging curent will not be visible), and the rate of data collection can be set from the main screen. The current as a function of potential will be output as an .xls sheet.

Operation:

This program will automatically run when it is opened, but no information is sent to the potentiostat. There are two tabs at the top of the program, "Setup" and "Start Expt." The "Setup" tab is open first, and contains all of the initialization parameters required. The "Start Expt." tab is used to start the experiment, and has a virtual output window showing the real time CV cycles as they are collected.

The parameters for the experiment should first be input in to the Setup tab. Once the parameters are correct, the power to the PStat box but NOT the cell should be turned on, and the Collect OCP button pressed. This will bring up a file save dialogue which will

determine the name of the .xls sheet created to store the OCP data. The OCP collection will begin running after the file is created.

Once the OCP has stabilized to the user's satisfaction (if the user cares) the experiment may be started by switching to the Start Expt. tab and clicking the Start button. This brings up another file creation dialog, this one to create a .xls sheet to hold the data generated during the experiement. BEFORE the file name is sent, the cell must be physically switched on, otherwise no voltage or current will be applied once the program starts.

After the file name is sent, the program will first apply the pre-CV potential (if requested), then run CV's until it is aborted due to an error, aborted by a user clicking the Stop button, or the number of loops specified in the Setup tab have been collected. A popup detailing the reason that the experiment has stopped will appear once the experiment is over. If the user wishes to skip a particular cycle while the CV is running, the Skip Cycle button will start the next cycle immediately.

Controls (Setup):

Potentiostat/Galvanostat Select: Toggle switch puts potentiostat into galvanostatic or potentiostatic mode.

Current Range Select: Toggle switch changes the potentiostat's current handling from 0-100 mA to 0-10 mA. 10 V is in all cases the highest voltage safely used.

Current Range (mA): Smaller ranges give higher resolution for current values obtained after analog to digital conversion.

Voltage Range (V): Smaller ranges give higher resolution for voltage values obtained after analog to digital conversion.

Overvoltage Limit (V): If the absolute value of the voltage ever exceeds this number, the VI will automatically abort the run.

Overcurrent Limit (mA): If the absolute value of the current ever exceeds this number, the VI will automatically abort the run.

Pre-CV Hold?: This boolean determines whether the potentiostat will hold at V_i for the length of time in Pre-CV Delay Time before starting the CV. If the green light is lit, this is set to Yes, if the light is off, it is set to No. This delay is used to help eliminate charging current artifacts in CV data.

Pre-CV Delay Time: This is the length of time to apply V_i to the working electrode before starting the CV.

Output Range (V or mA): Smaller ranges give higher resolution for the output voltage or current values obtained after digital to analogue conversion.

V_i (V): The starting potential of the triangular waveform to be applied at the working electrode. Positive voltages are oxidizing at the working electrode.

V_λ (V): Switching potential of the triangular waveform to be applied to the working electrode. Positive voltages are oxidizing at the working electrode.

Number of Cycles: Number of cycles of the triangular waveform to be applied to the working electrode.

Step Size, ΔV (mV): Voltage increments between adjacent data points within the waveform; smaller increments denerate higher resolution output waveforms.

Samples to Avg./Interval: Number of voltage/current samples acquired per voltage point on the waveform. The averaged value is saved as a voltage point on the data file.

Scan Rate (mV/sec): Rate of change of voltage points in the waveform, that is, how quickly the voltage scans from V_i to V_λ.

Intercycle Delay (ms): Amount of time between CV cycles (defaults to 0).

Final Resting Voltage (V) / Current (mA): The voltage or current which is applied at the end of the experiment and will continue to be applied after the program has been stopped. The cell must be turned off at the PStat module in order to cease the application of this voltage.

Controls (Start Expt.):

Start: This button stops the collection of the OCP and opens the dialogue to save the data generated by the experiment. Once a filename is input for the spreadsheet, the experiment will start.

Stop: This button will immediately abort an experiment in progress.

Skip Current Cycle: This button will skip the current cycle of the CV, starting at the beginning of the next cycle.

Stop Pre-CV: This button will halt the application of the pre-CV potential.

Outputs (Setup):

Elapsed Time (sec): The elapsed time of the open circuit potential measurement.

Open Circuit Potential (V): This is an averaged OCP calculated from a running average of the last few data points measured.

Real-time Chart: This is the main chart on the Setup tab. It outputs the last three points of the OCP voltage measurement, which is the voltage difference between the reference and

working electrodes.

Time/Cycle (sec): Number of seconds required for the completion of one full cycle of the triangular waveform, calculated from the distance between V_i and V_λ and Scan Rate.

Total Time (sec): Number of seconds required for completion of all requested cycles, calcuated from Time/Cycle and Number of Cycles.

Total Time (min): Number of minutes required for completion of all requested cycles.

Outputs (Start Expt.):

Voltage (V): Last measured voltage (positive is a relatively oxidizing potential at the working electrode).

Current (mA): Last measured current (positive is oxidizing at the working electrode.)

Real-time Graph: Plotted voltage vs. current.

V_i (V): The starting potential of the triangular waveform to be applied at the working electrode from Setup tab.

V_λ (V): Switching potential of the triangular waveform to be applied to the working electrode from Setup tab.

ΔV (mV): Voltage increments between adjacent data points within the waveform from Setup tab.

v (mV/sec): Scan Rate from Setup tab.

Current Cycle: Cycle currently being applied.

Number of Cycles: Number of cycles from Setup tab.

Final Resting Voltage (V) / Current (mA): The voltage or current which is applied at the end of the experiment form Setup tab.

ON/OFF: Feeback as to the state of the cell in question.

Pre CV Time (s): Pre-CV Delay Time from Setup tab.

Samples/Interval: Number of voltage/current samples acquired per voltage point from Setup tab.

Loop Rate: Number of milliseconds required to process one iteration of the data aquisition loop; this should stay below hundreds of milliseconds.

TotalSampGenerated: Total number of voltage points of the waveform being generated in

real-time. This resets for each cycle.

Intercycle Delay (ms)2: Intercycle Delay from the Setup tab.

AI Rate (samples/sec): Sampling rate of voltage and current measurements to the DAQ card.

AO Rate (samples/sec): Generation rate of voltage points from the DAQ card.

A.1.3   PStat X - CV-ED (A.2.3)

This program is an extensive modification of Evan's original program. The new version enables the application of an arbitrary waveform, allows more useful data acquisition parameters to be set, and has been subjected to the normal cleaning up and organization of code.

This program allows for pulsed, ramped, and cyclic waveforms to be applied at the working electrode. It is generally used for complex electrodepositions.

The program will automatically run when it is opened, but no information is sent to the potentiostat. There are two tabs at the top of the program, "Setup" and "Start Expt." The "Setup" tab is open first, and contains all of the initialization parameters required. The "Start Expt." tab is used to start the experiment, and has a virtual output window showing the real time current and voltage readings from the experiment if one is in progress.

The parameters for the experiment should first be input into the Setup tab. In addition to the normal, static parameters detailed below, the waveform to be applied must be built and the data acquisition scheme must be input. The waveform (voltage vs. time) is built by using the three inputs Start Potential, Potential, and Time as well as the Store button. When the Store button is pressed, the waveform is stored beginning at the Start Potential and taking a number of seconds equal to Time to get to Potential. When the Store button is pressed again, the next segment of the waveform is added, going from Last Potential to Potential over a number of seconds equal to the Time input. An arbitrary number of these segments can be stored. To create a step function, use Time = 0. To create a plateau, leave Potential unchanged between two points. The waveform in its current form is displayed in a fairly (but not absolutely) accurate graph above the inputs. Also there is a raptor.

The data aquisition parameters also deserve further explanation. There are two data aquisition rates - high and low. During the high rate, data is acquired at very high resolution, and during the low rate, it is acquired at low resolution or not at all. This prevents dozens of spreadsheets from being created over the course of a long experiment, while still getting all of the useful information. The use of the individual parameters is detailed in the Inputs section below. The number of excel spreadsheets that will be created by a particular data acquisition scheme is displayed as a bar at the bottom of the data aquisition section.

Once the parameters are correct, the power to the PStat box but NOT the cell should be turned on, and the Collect OCP button pressed. This will bring up a file save dialogue which will determine the name of the .xls sheet created to store the OCP data. The OCP collection will begin running after the file is created - if parameters are changed after OCP collection has started, they will NOT be used by the program.

Once the OCP has stabilized to the user's satisfaction (if the user cares) the experiment may be started by switching to the Start Expt. tab and clicking the Start button. This brings up another file creation dialog, this one to create a .xls sheet to hold the data generated during the experiement. BEFORE the file name is sent, the cell must be physically switched on, otherwise no voltage or current will be applied once the program starts. After the file name is sent, the experiment will run until it is aborted due to an error, aborted by a user clicking the Stop button, or the time specified in the Setup tab has elapsed. A popup detailing the reason that the experiment has stopped will appear once the experiment is over. If at any point the user wishes to artificially activate the high acquisition rate, the High Aquisition Rate button can be toggled. As long as it is active, data will be acquired at the high rate specified in the Setup tab. This may cause the amount of data generated to greatly exceed that predicted in the Setup tab, so use wisely.

Controls (Setup):

Potentiostat/Galvanostat Select: Toggle switch puts potentiostat into galvanostatic or potentiostatic mode.

Current Range Select: Toggle switch changes the potentiostat's current handling from 0-100 mA to 0-10 mA. 10 V is in all cases the highest voltage safely used.

Current Range (mA): Smaller ranges give higher resolution for current values obtained after analog to digital conversion.

Voltage Range (V): Smaller ranges give higher resolution for voltage values obtained after analog to digital conversion.

Overvoltage Limit (V): If the absolute value of the voltage ever exceeds this number, the VI will automatically abort the run.

Overcurrent Limit (mA): If the absolute value of the current ever exceeds this number, the VI will automatically abort the run.

Output Range (V or mA): Smaller ranges give higher resolution for the output voltage or current values obtained after digital to analogue conversion.

High Time (sec): The amount of time that the program will collect data at a high rate before cycling to the low rate.

High Rate (samples/sec): The number of samples per second that the program will collect

when recording data at its high rate.

Low Time (sec): The amount of time that the program will collect data at a low rate before switching back to the high rate of acquisition.

Low Rate (samples/sec): The number of samples per second that the program will collect when recording data at its low rate.

Start Potential: The voltage at which the applied waveform will start. When the wave cycles, the last potential acquired will jump abruptly to the Start Potential at the beginning of the next run, if it is not the same potential.

Potential: The next point on the Y (voltage) axis the waveform being built will acquire when the Store button is pressed.

Time: The distance on the X (time) axis that the waveform being built will travel in acquiring Potential after the Store button is pressed.

Store: When this button is pressed, the waveform to be passed to the potentiostat is updated to include the next point, determined by Potential and Time.

Step Size, ΔV (mV): Voltage increments between adjacent data points within the waveform; smaller increments denerate higher resolution output waveforms.

Scan Rate (mV/sec): Rate of change of voltage points in the waveform, that is, how quickly the voltage scans across the waveform.

Controls (Start Expt.):

Start: This button stops the collection of the OCP and opens the dialogue to save the data generated by the experiment. Once a filename is input for the spreadsheet, the experiment will start.

Stop: This button will immediately abort an experiment in progress.

High Acquisition Rate: When toggled, this button will force the program to acquire at the high acquisition rate until it is untoggled. This is so if something unusual starts happening in the experiment it can be recorded. Leaving this on has the potential to make a whole lot of extra data.

Samples/Interval: Number of voltage/current samples acquired per voltage point on the waveform. Shouldn't really be changed for this VI.

Outputs (Setup):

Elapsed Time (sec): The elapsed time of the open circuit potential measurement.

Open Circuit Potential (V): This is an averaged OCP calculated from a running average of the last few data points measured.

Real-time Chart: This is the main chart on the Setup tab. It outputs the last three points of the OCP voltage measurement, which is the voltage difference between the reference and working electrodes.

Number of Excel Sheets Filled: This bar shows how many Excel sheets will be filled by the data scheduled to be collected. An Excel sheet contains 65536 lines maximum. Note that use of the High Acquisition Rate button will exceed this number.

XY Graph: This is a plot of the waveform which will be applied during the experiment. As the waveform is updated,

Outputs (Start Expt.):

Voltage: The latest voltage point read by the program.

Current: The latest current point read by the program.

ON/OFF: This provides feedback as to the current state of the cell in question.

Elapsed Time (sec): The amount of time that has passed since the experiment was started.

Time Remaining (sec): Total Time - Elapsed Time.

Voltage Overload: This provides feedback if an experiement has been ended due to a voltage overload. If the lamp is illuminated, this is the reason for the end of the experiment.

Current Overload: This provides feedback if an experiement has been ended due to a current overload. If the lamp is illuminated, this is the reason for the end of the experiment.

ΔV (mV): Voltage increments between adjacent data points within the waveform from Setup tab.

v (mV/sec): Scan Rate from Setup tab.

Sample Rate: The current rate in samples/sec at which data points are being recorded to the output file.

Last Recorded Data: The time elapsed since the beginning of the experiment at which data was last recorded to the output file.

Current Range: Current Range from the Setup tab.

Final Resting Voltage (V): Final Resting Voltage from the Setup tab.

Real-Time Chart: Outputs the currently read current (top) and voltage (bottom) from the

experiment. This does not reflect the data which has actually been recorded.

AO Rate samples/sec: Generation rate of voltage or current points from the DAQ card.

A.1.4   PStat X - Resistance (A.2.4)

This program tracks the resulting current from a small applied voltage and calculates the resistance between the working electrode and the reference / counter electrode.

The program allows for a pre-experiment anodization (or cathodization...) step to prepare the sample being analyzed. This step can be tuned just as a normal potentiostatic or galvanostatic run. The program also allows the determination of resistance using either AC or DC measurement.

The program will start when it is opened, but no information is passed to the potentiostat. The anodization controls are in the upper left corner of the operations screen. Toggling the Advanced Controls button will open a large panel to further tune the anodization parameters. Anodization is not enabled by default.

The resistance acquistion controls are in the lower left hand corner. Setting the AC frequency dial to 0 will cause the program to operate in DC resistance mode.

The potentiostat box and cell should both be switched on before pressing the start button.

When the start button is pressed, the program will prompt the user for the desired file names for the anodization data (if any) and the resistance data. It will then run the anodization if requested. It will then start the resistance measurement after a 5 second countdown displayed on the screen, so that electrodes can be attached in a time-sensitive experiment. DC resistance measures the current resulting from an applied voltage and uses ohm's law to derive the resistance directly. AC resistance applies an oscillating voltage and measures the current at each voltage. The slope of a number of current versus voltage runs is calculated and reported as the resistance (again, straight from ohm's law).

Controls:

Anodization Duration (sec): The duration of the anodization step.

Anodization Toggle: Enables or disables the anodization step. Disabled by default.

Advanced Panel: Hides or reveals the advanced panel.

Anodization Current (mA): Only visible on advanced pannel. The current in mA (or potential in potentiostatic mode) for the anodization step.

Anod Potent. vs. Galvan.: Only visible on advanced pannel. Toggle switch puts potentiostat

into galvanostatic or potentiostatic mode for the anodization step.

Current Select: Only visible on advanced panel. Toggle switch changes the potentiostat's current handling from 0-100 mA to 0-10 mA for the anodization step. 10 V is in all cases the highest voltage safely used.

Anod. Current Min and *Anod. Current Max:* Only visible on advanced panel. Smaller ranges give higher resolution for current values obtained after analog to digital conversion. Only applied for the anodization step.

Anod. Voltage Min and *Anod. Voltage Max:* Only visible on advanced panel. Smaller ranges give higher resolution for voltage values obtained after analog to digital conversion. Only applied for the anodization step.

Overvoltage Limit (V): Only visible on advanced panel. If the absolute value of the voltage ever exceeds this number, the VI will automatically abort the run. Only applied for the anodization step.

Overcurrent Limit (mA): Only visible on advanced panel. If the absolute value of the current ever exceeds this number, the VI will automatically abort the run. Only applied for the anodization step.

Output Min and *Output Max:* Only visible on advanced panel. Smaller ranges give higher resolution for the output voltage or current values obtained after digital to analogue conversion. Only applied for the anodization step.

Anodization Sampling Time: Only visible on advanced panel. The length of time between the acquisition of individual voltage / current samples during the anodization step. Along with Anodization Duration, this directly determines the size of the data file created.

Postprocess Data: This toggle will average every 5 data points acquired in the measurement of DC resistance only.

Enable R Limit: The toggle will cause the resistance measurement to stop once the resistance is below the threshold set in ResistanceLimit.

ResistanceLimit (kOhms): This is the threshold below which the resistance measurement will stop if Enable R Limit is TRUE.

Resistance Duration (sec): This is the duration of the resistance data acquisition.

Target R kOhms: This is a softer version of the R Limit toggle. When the resistance first reaches this value, the time will be stored, but the resistance measurement will continue.

Frequency Hz (0 = DC): This dial is used to set the frequency of the AC measurement of resistance. If this input is set to 0, a DC resistance measurement will be performed.

Outputs:

Pot X ON: Indicates the state of the potentiostat in question.

Pot X OFF: Indicates the state of the potentiostat in question.

AC Graph: This is a feedback chart showing the waveform generated by changing the Frequency input dial.

Alumina Thickness (microns): Visible during anodizations and setup. The calculated thickness of alumina produced by a galvanostatic current of the amplitude specified for the duration elapsed.

Voltage (V): Visible during anodizations and setup. Last measured voltage during the anodization step (positive is a relatively oxidizing potential at the working electrode).

Current (mA): Visible during anodizations and setup. Last measured current during the anodization step (positive is oxidizing at the working electrode.)

Real-time Chart: Visible during anodizations and setup. Plot of measured voltage and current vs. time during the anodization step.

Elapsed Time (s): The amount of time that has passed since the anodization experiment was started.

Time Remaining: Total amount of time in the experiement - Elapsed Time.

Resistance Chart: Visible during resistance measurement only. This large window provides real-time feedback on the acquired resistance measurement.

Current versus Voltage Chart: Visible during AC resistance measurement only. This small window to the lower middle of the screen shows the current versus voltage for the measurement of the current point on the Resistance Chart. Linear output here indicates ohmic contacts.

Current and Voltage versus Time Chart: Visible during AC resistance measurement only. This small window to the lower right of the screen shows the voltage cycle overtop the resultant current cycle. It is essentially the Current versus Voltage Chart expanded over time. If the current and voltage signals are offset, it will be reflected in an oblong figure on the Current versus Voltage Chart.

Voltage Overload: This provides feedback if an experiement has been ended due to a voltage overload. If the lamp is illuminated, this is the reason for the end of the experiment.

Current Overload: This provides feedback if an experiement has been ended due to a current overload. If the lamp is illuminated, this is the reason for the end of the experiment.

A.1.5   PStat X - OCP (A.2.5)

This program has not been modified from the original version which Evan Hajime programmed, but in order to keep all of this information in one place, I will detail its operation here.

PStat X - OCP is used to find the open circuit potential of a solution. This involves essentially using the potentiostat as a voltammeter, and tracking the voltage between the working and reference electrode without any externally applied potential. Because this functionality is built into the other programs, this separate program is seldom used, and given that its operation is so similar to that of most of the other programs detailed here, I'll not describe it further.

A.2   LabView Code

This section will serve to document the LabView code I have made and modified as well as the original, undocumented code in order to aid future modification. I'll start out with a few general points on the organization of the programs.

Each computer, Hamachi and Fugu, is connected to three potentiostats. Hamachi is connected to A, B, and C, while Fugu is connected to D, E, and F. Each potentiostat connected to the same computer is uniquely addressed by the individual VI programs serving that potentiostat. In order to create a new program, each device instructions sub-VI must be directed towards the appropriate device. On Hamachi, potentiostat A is Dev1, potentiostat B is Dev2, and potentiostat C is Dev3. On Fugu, potentiostat D is Dev1, potentiostat E is Dev2, and potentiostat F is Dev3. In order to aid in the creation of new programs, most of the commands containing unique device-addressed inputs are condensed into separate and appropriately named sub-VIs, detailed below. In order to increase portability between the two computers, sub-VIs pointing to potentiostats D, E, and F on Fugu are labeled A, B, and C respectively.

Reference nodes are used extensively through all of the programs I have made and modified. These serve two functions. First, they allow the code to be written without extraneous wires, making it easier to understand and modify. Secondly, a reference node is checked against its source only when it is needed, not when the information is stored in the source. This allows the input to be changed after the program has been started. In a number of the original programs, changing inputs after the program had been run would result in values which seemed to be accepted by the program but which in reality were not being used, since the inputs would not be read a second time. The one downside to reference nodes is that they require more processing power than a simple wire connection. This is only a problem if they are used heavily in a time-sensitive loop or similar structure, but I've run into it once or twice and is worth keeping in mind.

A.2.1 PStat X Constant 01-20-11.vi

Inputs: None

Outputs:

OCP File: OCP data saved as an .xls spreadsheet in a user-created file.

Data output file: Current and voltage data versus time in the experiement saved as an .xls spreadsheet in a user-created file.

Dependencies: Cell X Galv-Potent Select.vi (A.2.6); Cell X Current Range.vi (A.2.7); Cell X Settings.vi (A.2.8); Turn Cell X ON.vi (A.2.9); Cell X Cleanup+Resting.vi (A.2.10); Turn Cell X OFF.vi (A.2.11); V-I Data Manipulation.vi (A.2.12); OCP Data Manipulation.vi (A.2.20)

This program has been modified extensively from its original version. It has been organized into a stable progression with determined temporal order using frame and loop structures and variable references.

In the beginning of Figure A.1, section A is the startup loop, which executes when the program starts. When the collect OCP button is pressed, the loop stops and the next frame is started.

B makes the Collect OCP button invisible. Simultaneously, C initializes the Potentostatic / Galvanostatic mode selection, D initializes the current range selection, and F brings up a dialogue for the user to input a filename for the OCP data. E generates the default name for this file as Constant (A) - [hours] - [minutes] - [date] - OCP.xls and passes it to the file creation dialogue. G manages sequencing so that H does not execute until all of the previous setup steps have fired. H starts the OCP collection task, referencing the potentiostat in question.

The OCP loop then fires. I collects data and sends it to the waveform output graph. J processes the data, splitting it into time and voltage, placing it into a 1x2 matrix, and sending it to the file created in F. K counts the loop's elapsed time, while the metronome makes sure it executes every 1000 milliseconds. L regulates stopping the loop, stopping it when the Start button (in the Start Expt. tab) is pressed. The Ready button in the lower right corner of the OCP loop does nothing, and will in fact reset after the loop refreshes in its one second loop.

When the loop is stopped, M stops the data aquisition task and frees the resources associated with it. N closes the file created in F and manipulates its data into a coherent spreadsheet. Once this is finished, O is supposed to apply the average voltage colleded during the OCP to keep the experiement in a neutral position. However, this can't happen because at this point the PStat cell is still off... so it just pretends. Finally, P creates the file for data acquisition, using the same string as F for the default, minus the OCP designation.

Figure A.1: Code diagram of PStat A - Constant - 01-20-11.vi; for other potentiostats, the sub-VIs referencing the appropriate device are used.

Figure A.2: Code diagram of PStat A - Constant - 01-20-11.vi; for other potentiostats, the sub-VIs referencing the appropriate device are used.

The next frame, in Figure A.2 initializes the instrument, and will execute as soon as the file collection dialogue is finished (again, regulated by the error wire). At this point, the cell should have been turned on by the user. First, Q turns the cell on. R applies any voltage offset appropriate to the potentiostat in question. The example program has no offset, and the offsets should be wired to the appropriate adders in order to use this functionality. S applies the Current Range selection and T applies the Potentiostat / Galvanostatic mode selection. Finally, U applies the settings referenced from the startup loop, initializing the instrument.

The next frame is the acquisition and application loop. V moniters the status of the current / potential application, waiting for it to finish. W reads the data from the acquisition task and passes it to X, which sends it to the output screen as well as parsing it into time, voltage, and current. Y then puts this data into a 1x4 matrix, and sends it to Z, which puts it into the file created at P. α moniters the absolute value of the current and voltage and sends a kill signal if either exeeds the tolerance input in the startup loop. β regulates the timing, sending a kill signal to the loop when the total time has been met. γ regulates the loop cycle to every 0.2 seconds. Finally, δ accepts signals stopping the acquisition loop, from the user hitting the Stop button, overcurrent, the normal timeout, or errors in data processing.

When the eperiment loop is finished executing, the cleanup frame is called. Simultaneously, ϵ cleans up all the tasks, freeing the memory used, and applies the resting voltage; ζ closes the file, then passes it to the data manipulation sub-VI for processing; and η turns off the cell. Once these have all completed, θ looks at the error thread and reports any errors it sees.

A.2.2 PStat X - CV - 01-20-11.vi

Inputs: None

Outputs:

OCP File: OCP data saved as an .xls spreadsheet in a user-created file.

Data output file: Current versus voltage data in the experiement saved as an .xls spreadsheet in a user-created file.

Dependencies: CV Cycle Generation.vi (A.2.15); Cell X Galv-Potent Select.vi (A.2.6); Cell X Current Range.vi (A.2.7); Cell X OCP Setup.vi (A.2.17); OCP Data Manipulation.vi (A.2.20); Cell X Apply Potential.vi (A.2.18); Cell X CV Cycle Setup.vi (A.2.22); Get Terminal Name with Device Prefix.vi (A.2.23); Turn Cell X ON.vi (A.2.9); Turn Cell X OFF.vi (A.2.11); CV Data Manipulation 2.vi (A.2.16);
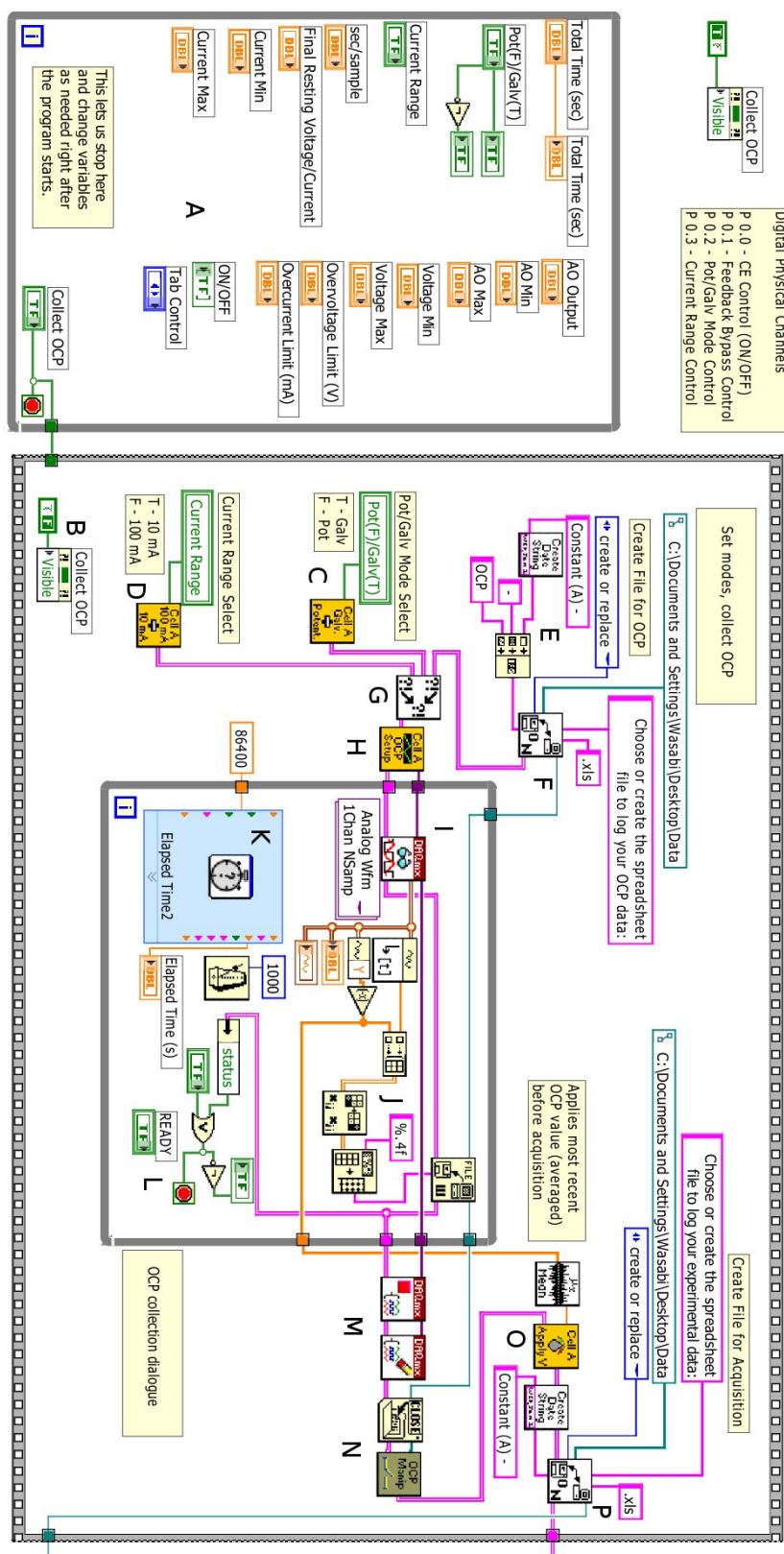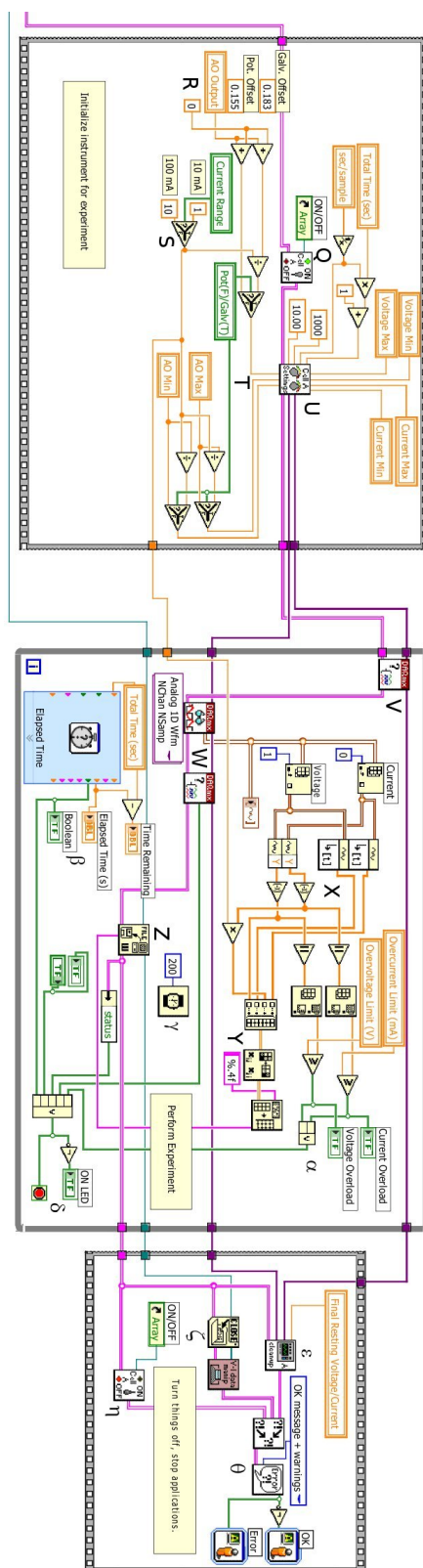
Figure A.3: Code diagram of PStat A - CV - 01-20-11.vi; for other potentiostats, the sub-VIs referencing the appropriate device are used.

Figure A.4: Code diagram of PStat A - CV - 01-20-11.vi; for other potentiostats, the sub-VIs referencing the appropriate device are used.
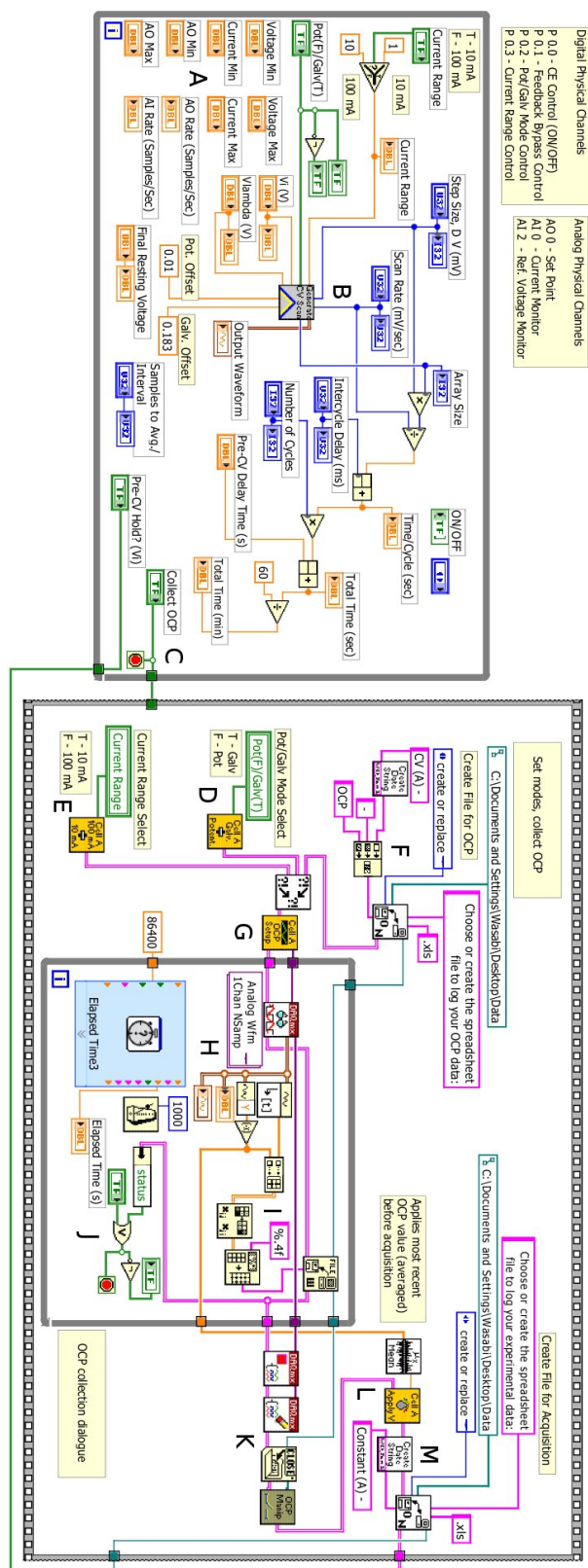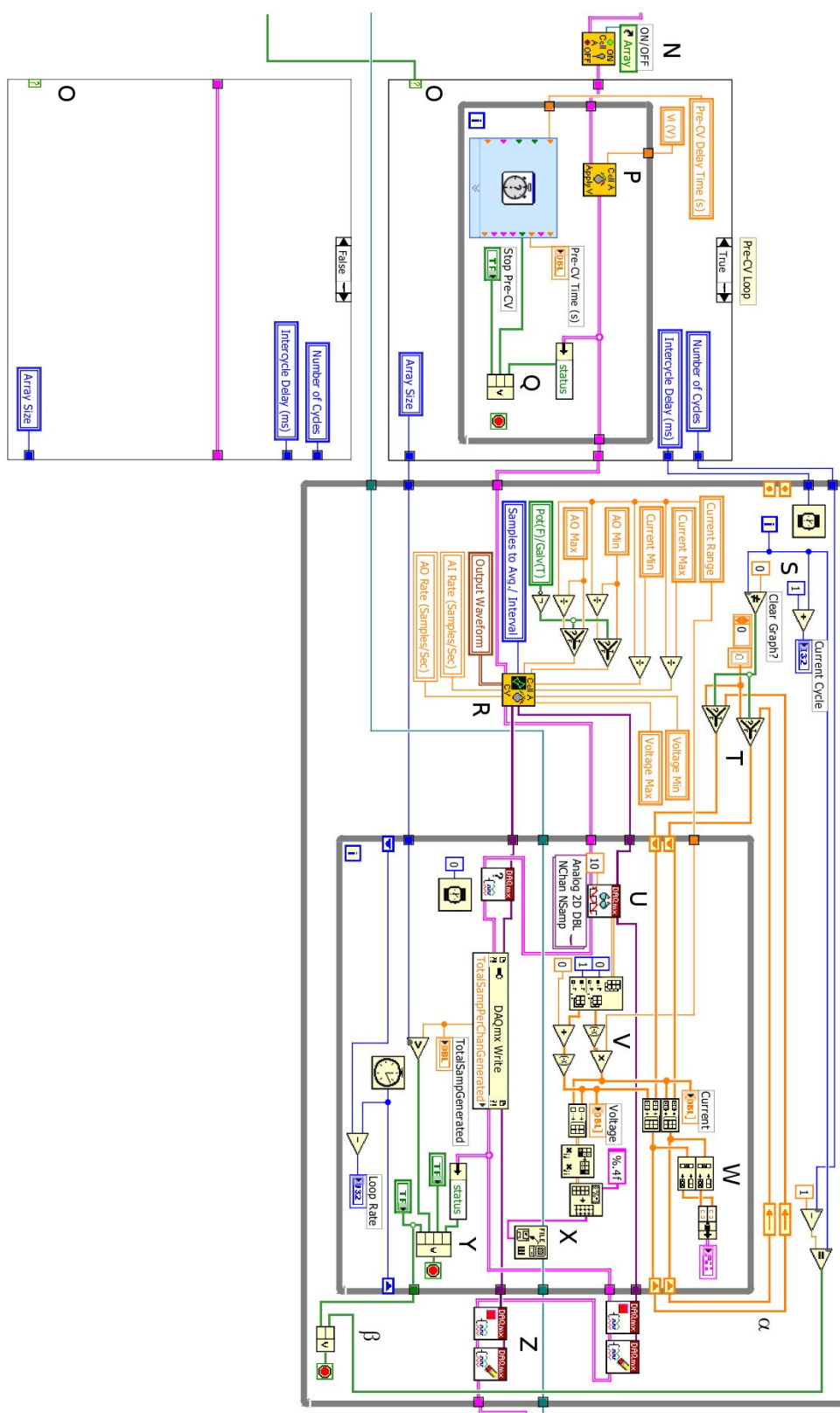
Figure A.5: Code diagram of PStat A - CV - 01-20-11.vi; for other potentiostats, the sub-VIs referencing the appropriate device are used.

This VI runs Cyclic Voltammetric experiments. While originally programmed by Evan Hajime, I have modified it extensively from its original version, condensing and clarifying circuitry and creating a number of functions to ease modification.

The VI is a large one, and has been split into multiple pages in this document to be more easily read. In Figure A.3, section A contains all of the user-defined inputs in the program. B inputs the appropriate variables into CV Cycle Generation 5.vi (**??**). This is a loop so that as information is updated by the user, the appropriate outputs are calculated and updated in concert. C controls stopping this loop - once the OCP is being collected, the CV waveform will no longer be updated.

D sets the Potentiostatic / Galvanostatic toggle and E sets the Current Range selected in A. F creates a file to save the 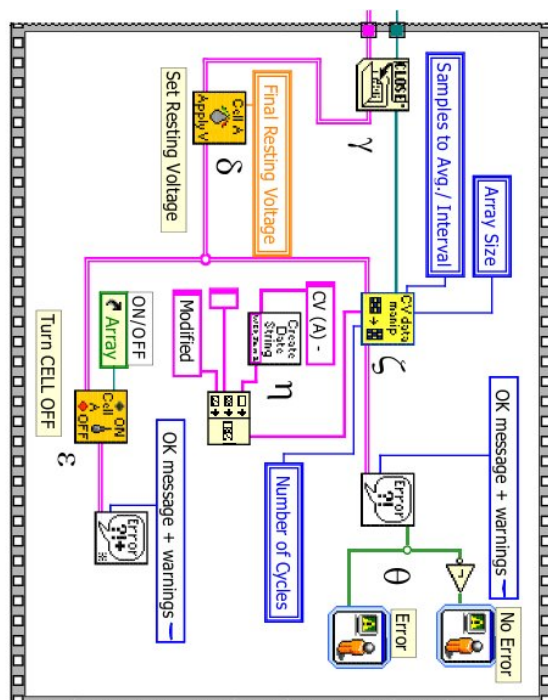OCP data to. G starts the OCP data collection task, and H loops the data collection, updaing the outputs on the screen. I saves this information to the file created in F. J regulates the loop - if a sub-VI throws an error or the Start button is pressed on the other tab, the OCP experiment is ended. At that point, K stops and clears the OCP data collection task, closes the file for writing, and sends the file to OCP Data Manipulation.vi (A.2.20) for formatting. L applies the averaged OCP to the working electrode (to keep the experiement stable) and M creates a file for recording the CV experiment data.

In Figure A.4, N accepts the error out from M and turns the cell on. O accepts the boolean

input from C, determined by the user-defined Pre CV Hold? (Vi) input. If this is TRUE, the pre-CV potential is applied for the requested amount of time. P Applies the potential of the V_i user defined input fo the amount of time specified by Pre-CV Delay Time (s). Q governs the ending of this loop, stopping it if an error is caught in P, if the Stop Pre-CV button is pressed, or if the time has ended. O, whether TRUE or FALSE, passes Number of Cycles, Intercycle Delay (ms), and Array Size to the CV loop.

The CV loop initializes the CV, inputing all the appropriate variables in R. S regulates the loop's cycling, keeping track of the number of CV cycles collected so far. T will clear the graph if this is the first cycle, also passing the graph information to the single-cycle loop in the center. I reads the data passed in by the read teask started in R, passing it to V, which separates it into voltage, current, and time, passing it to W, which displays current versus voltage on the graph, and X, which records the current and voltage into the file created in M. Y governs the execution of this loop, stopping it if the number of samples requested (the array size of the CV waveform) has been generated, if the Skip Cycle button is pressed, if the Stop All button is pressed, or if one of the functions generates an error. Z then ceans up the read and apply potential tasks started in R, so they can be re-started with the next iteration of the large loop. The loopbacks at α ensure that the CV data chart retains its data across the loops. Finally, β governs the large loop execution, halting if the Stop All button is pressed or if the number of loops requested has been reached.

In Figure A.5, γ closes the file created in M and modified by X. δ applies the resting voltage requested, and then ϵ turns the cell off while ζ passes the file to CV Data Manipulation 2.vi (A.2.16) along with the appropriate variables and the date string generated in η. Finally, θ checks for errors and reports an all-clear or whatever error is found.

A.2.3   PStat X - CV-ED - 01-20-11.vi

Inputs: None

Outputs:

OCP File: OCP data saved as an .xls spreadsheet in a user-created file.

Data output file: Current versus voltage data in the experiement saved as an .xls spreadsheet in a user-created file.

Dependencies: Cell X Galv-Potent Select.vi (A.2.6); Cell X Current Range.vi (A.2.7); Cell X OCP Setup.vi (A.2.17); OCP Data Manipulation.vi (A.2.20); Cell X Apply Potential.vi (A.2.18); Cell X CV-ED Counter.vi (A.2.19); Cell X CVED Setup.vi (A.2.21); Turn Cell X ON.vi (A.2.9); Turn Cell X OFF.vi (A.2.11)

The bones of this VI were programmed by Evan Hajime, but it has been extensively modified. The modifications allow for the application of an arbitrary waveform, the ability to change

Figure A.6: Code diagram of PStat A - CV-ED - 01-20-11.vi; for other potentiostats, the sub-VIs referencing the appropriate device are used.
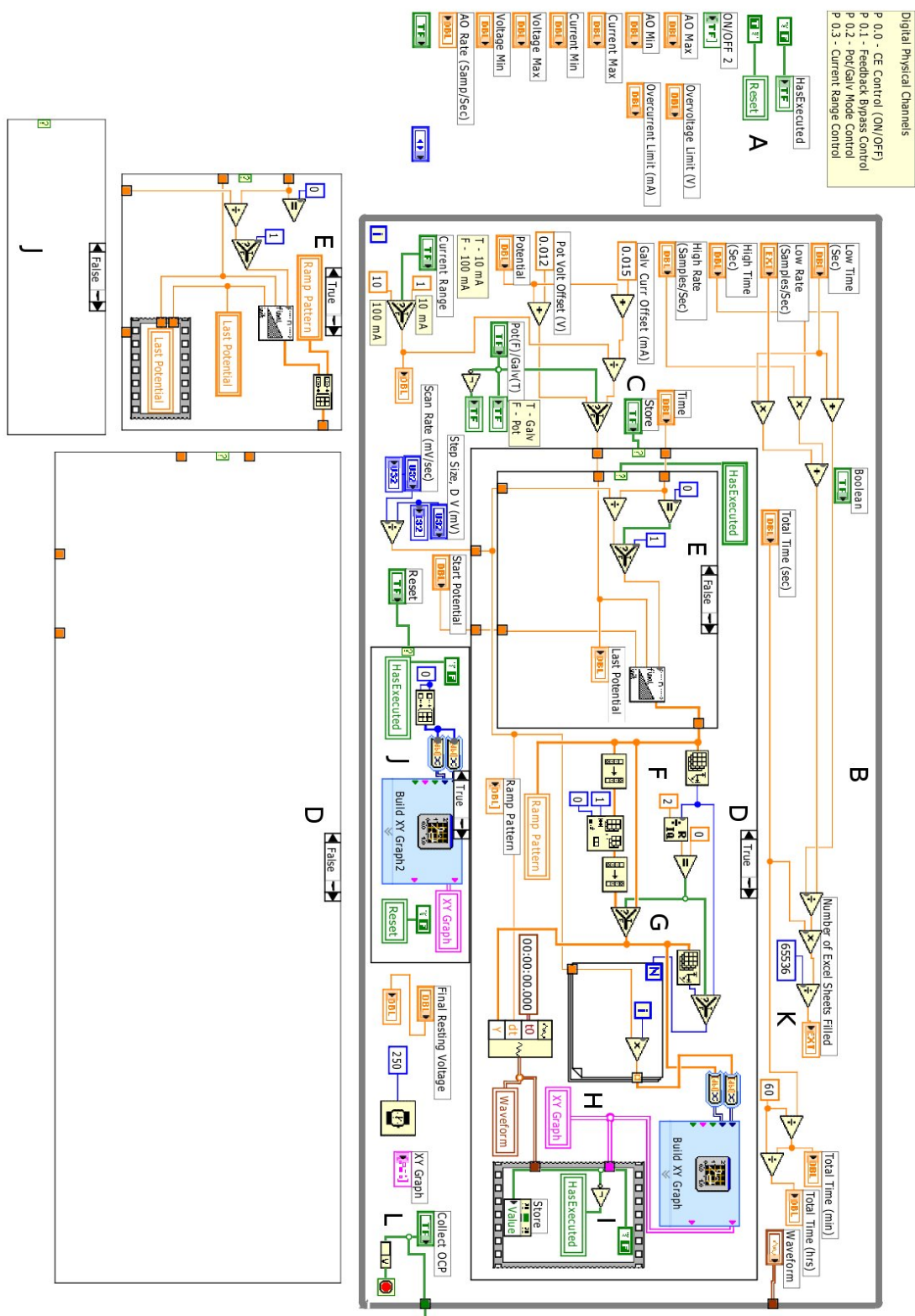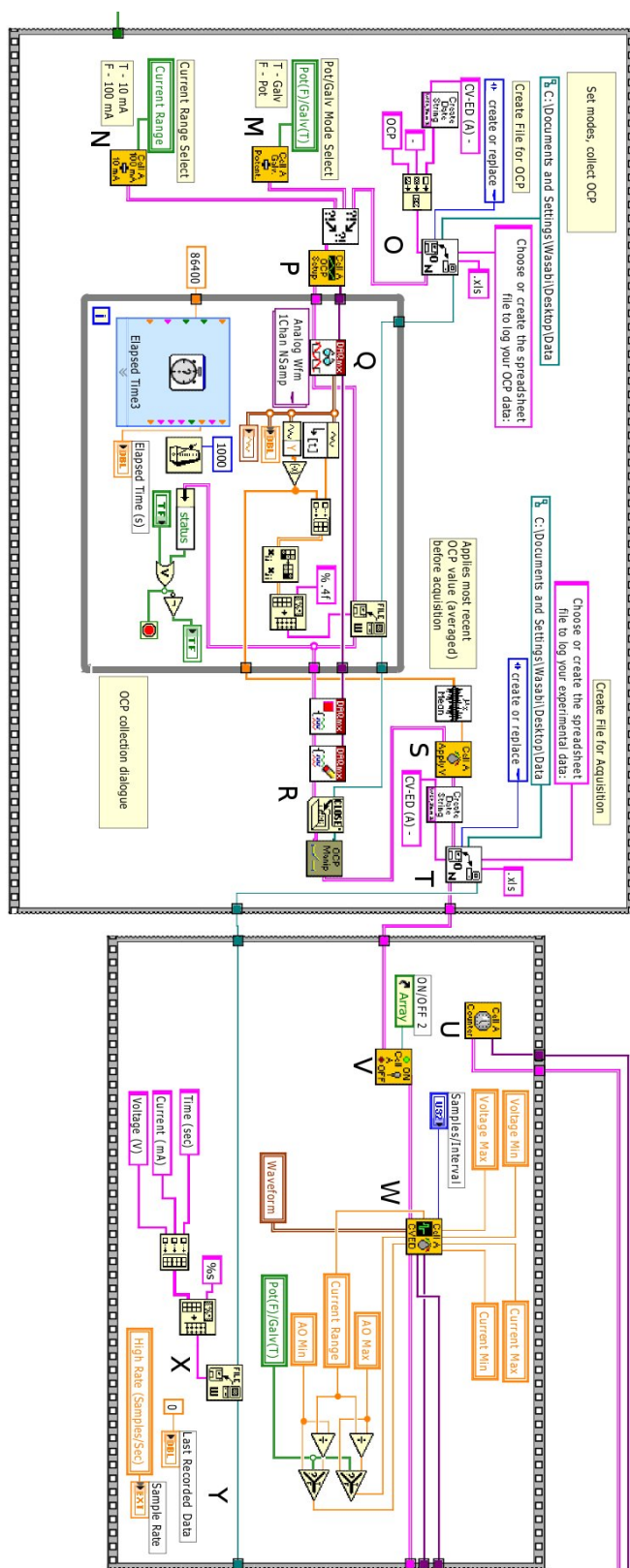
Figure A.7: Code diagram of PStat A - CV-ED - 01-20-11.vi; for other potentiostats, the sub-VIs referencing the appropriate device are used.

Figure A.8: Code diagram of PStat A - CV-ED - 01-20-11.vi; for other potentiostats, the sub-VIs referencing the appropriate device are used.

the data recording rate while still seeing the pulse patterns, more flexible high and low data record timing, and pre-caculation of storage space needed. Additionally, and as usual, the block diagram was cleaned up and compartmentalized into functions.

Figure A.6 shows the opening loop of the program. A is a collection of user inputs as well as the initializers for the loop, setting HasExecuted to FALSE and Reset to TRUE. B is the opening loop itself. This loop updates the calculated values, such as drawing the waveform to be applied as it is generated by the user. When Start Potential, Time, and Potential are filled out as detailed in the operation instructions (Pstat X - CV-ED), the Store button is pressed. At C, this sets frame D (which is checked every time B iterates) to TRUE. First, HasExecuted is checked in E. In both cases Potential is saved as Last Potential. If FALSE, a ramp from Start Potential to Potential over a number of points calculated from Time, Scan Rate, and Step Size is created. If TRUE, a ramp from Last Potential to Potential over a number of points calculated from Time, Scan Rate, and Step Size is created, then added to the previously existing Ramp Pattern. We want an even number of points in our array to make sure the loop at G executes correctly, so F makes sure that's the case, also sending the current pattern to be stored as Ramp Pattern. The loop at G makes a time line of the appropriate step size so that the graph has an X axis. H is where information gets sent where it should go - the waveform is generated, the XY graph displaying the created waveform is generated, and the HasExecuted bit is set to TRUE in I. The frame J handles resetting the graph by clearing it to 0's and setting HasExecuted back to FALSE. L will stop the initializeation loop if the Collect OCP button is pressed.

The OCP loop in Figure A.7 will fire once the initialization loop has finished. N sets current range, M sets galvanostatic or potentiostatic mode, and O creates the OCP data file. P starts the OCP data collection after the previous three have fired. Q is the OCP loop, cycling every second and storing the voltage data read in the file while updating the output chart. The loop will stop with an error or if the Start button is pushed. R stops the voltage collection task begun in P and sends the OCP data file to OCP Data Manipulation.vi (A.2.20) to be formatted. S applies the mean OCP voltage to the cell to keep the reaction stable. T creates the data file to store the data from the main experiment.

When the OCP cycle frame has executed, the setup frame starts. V turns on the instrument and U starts a counter to keep track of timing. W applies the user input settings and starts the data collection and current/voltage application tasks. X modifies the file created in T to have column headers. Y sets the Last Recorded Data to 0 (since there was none) and the Sample Rate to the High Rate to start with.

Figure A.8 starts with the main acquisition loop. Z rides on the data read task line, collecting the current and voltage data, while α regulates the voltage or current application. The data read task is set up to collect continuous samples, and β passes those continuous samples on to the output charts. γ moniters the output for overcurrent or overvoltage, and sends a kill signal and feedback if either is matched. δ is the heart of the data recording regulation. It only fires if the the amount of time determined by Sample Rate has passed. When it does fire, the Current, Voltage, and time since the experiment started are stored in the file created

by T and Last Recorded Data is set to Time, so that δ will not fire again until another appropriate amount of time has passed. The frame at ϵ governs the switching between the user-defined high and low sample rates. It will fire only if an amount of time determined by High Time or Low Time (user input variables) has passed. When it does fire, it sets the Sample Rate to Low Rate, then, if the sample rate should actually be the High Rate, it sets the Sample Rate to High Rate with the if frame at ζ. η governs the execution of the loop, stopping it at current or voltage overload, an error in any of the tasks, if the Stop button is pressed, or when the timing function sees that the time is over.

The last frame cleans everything up. θ stops the read task and ι stops the write task. κ stopps the counter task begun in U. The data file is closed in λ. The cell is turned off at μ, the resting voltage is applied at ν, and the errors (if any) are analyzed and feedback is given at ξ

A.2.4 PStat X - Resistance - 01-25-11.vi

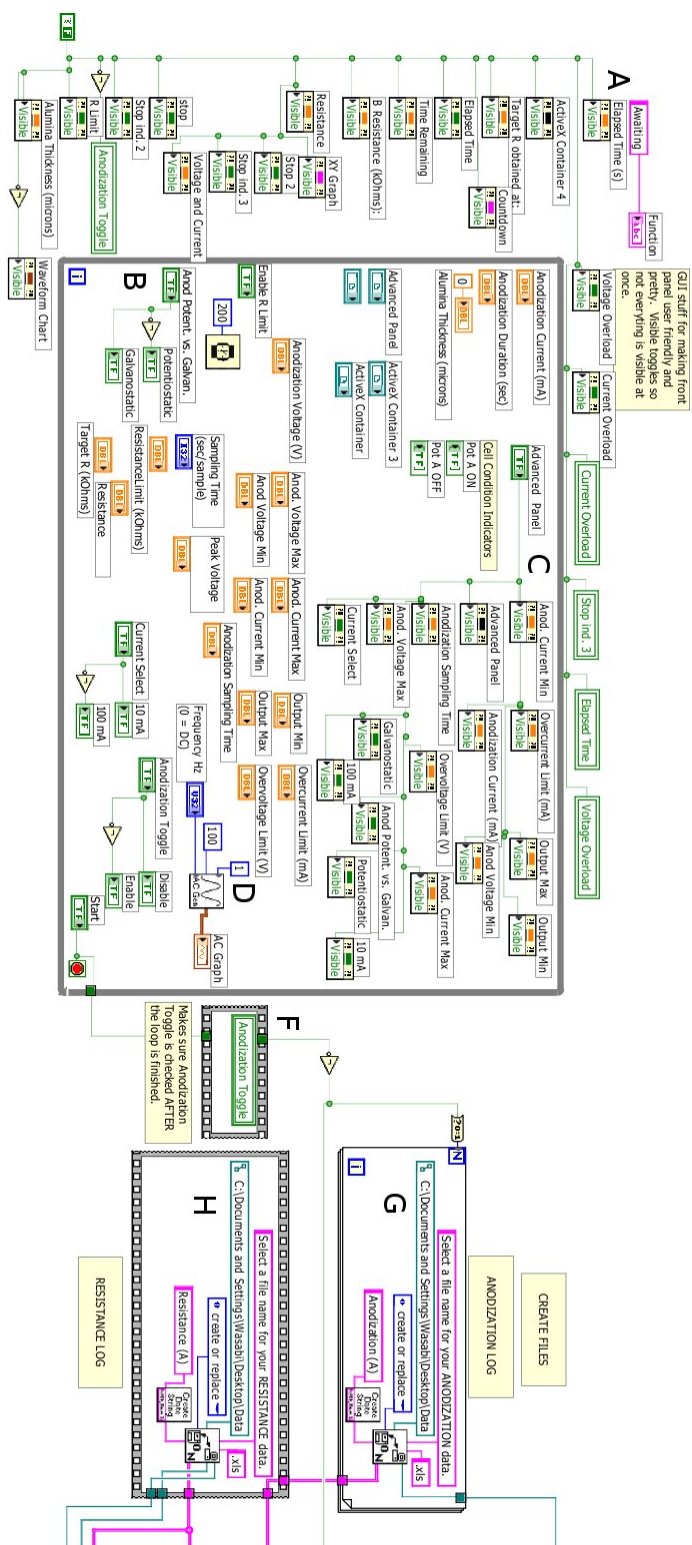**Inputs:** None

Outputs:

Anodization data output file: Current and voltage versus time data for an optional potentiostatic or galvanostatic experiment preceding the resistance acquisition, saved as an .xls spreadsheet in a user-created file.

Resistance data output file: Resistance versus time data along with some other useful metrics such as the R^2 of the resistance measurement (if AC resistance is used), saved as an .xls spreadsheet in a user-created file.

Raw resistance data output file: Unprocessed current and voltage versus time data from the resistance measurement (only an output of AC resistance acquisition).

Dependencies: AC Signal Gen.vi (A.2.24); Cell X Galv-Potent Select.vi (A.2.6); Cell X Current Range.vi (A.2.7); Cell X Apply Potential.vi (A.2.18); Cell X CV Cycle Setup.vi (A.2.22); Get Terminal Name with Device Prefix.vi (A.2.23); Turn Cell X ON.vi (A.2.9); Turn Cell X OFF.vi (A.2.11); Cell X Settings.vi (A.2.8); Cell X Cleanup+Resting.vi (A.2.10); Resistance Processing.vi (A.2.13)

This program was originally meant to allow for resistance over time measurements to track the dissolution of alumina in various solutions, but can be used to take resistance over time measurments of arbitrary systems.

Figure A.9: Code diagram of PStat A - Resistance - 01-25-11.vi; for other potentiostats, the sub-VIs referencing the appropriate device are used.

Figure A.10: Code diagram of PStat A - Resistance - 01-25-11.vi; for other potentiostats, the sub-VIs referencing the appropriate device are used.
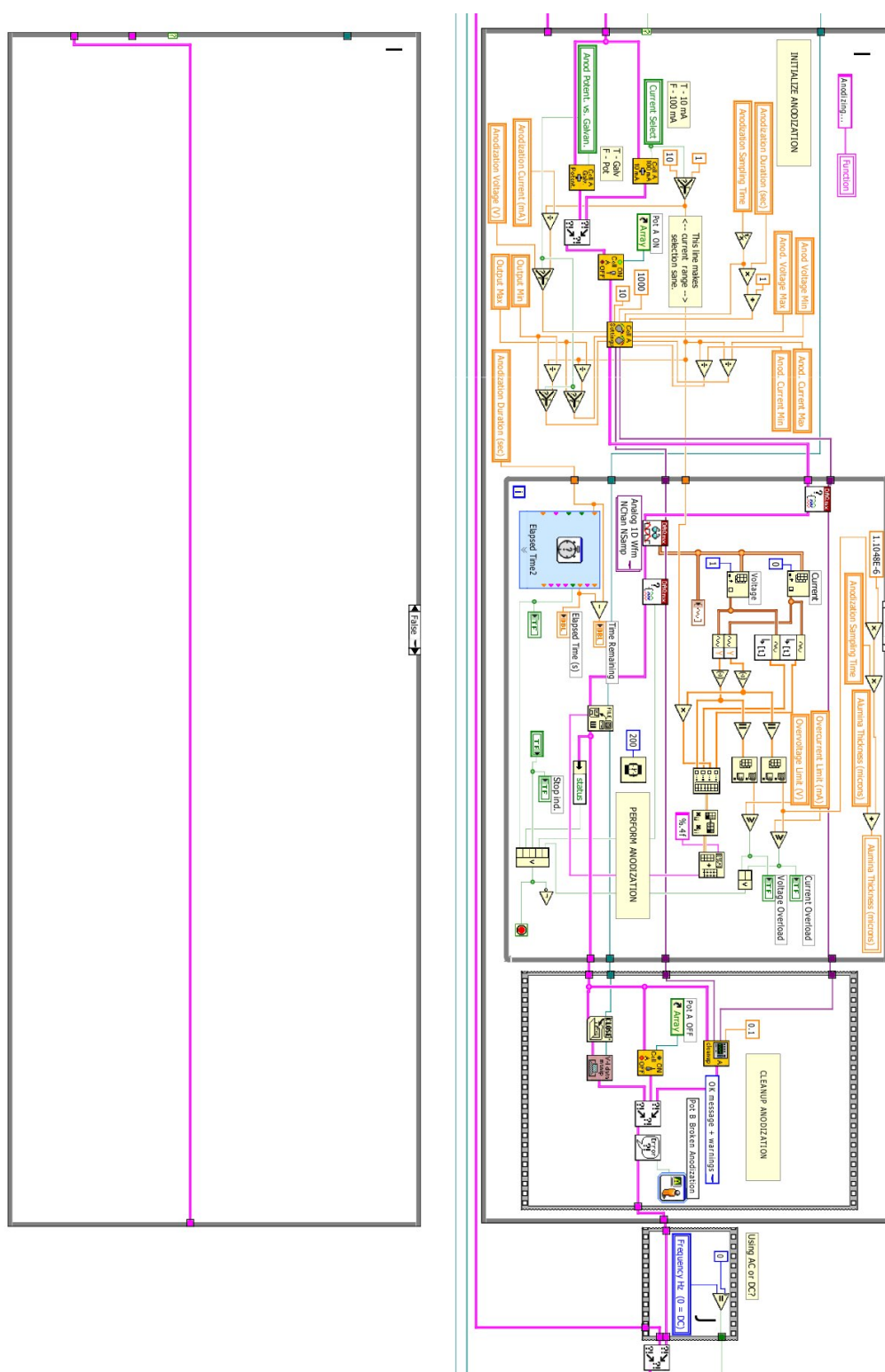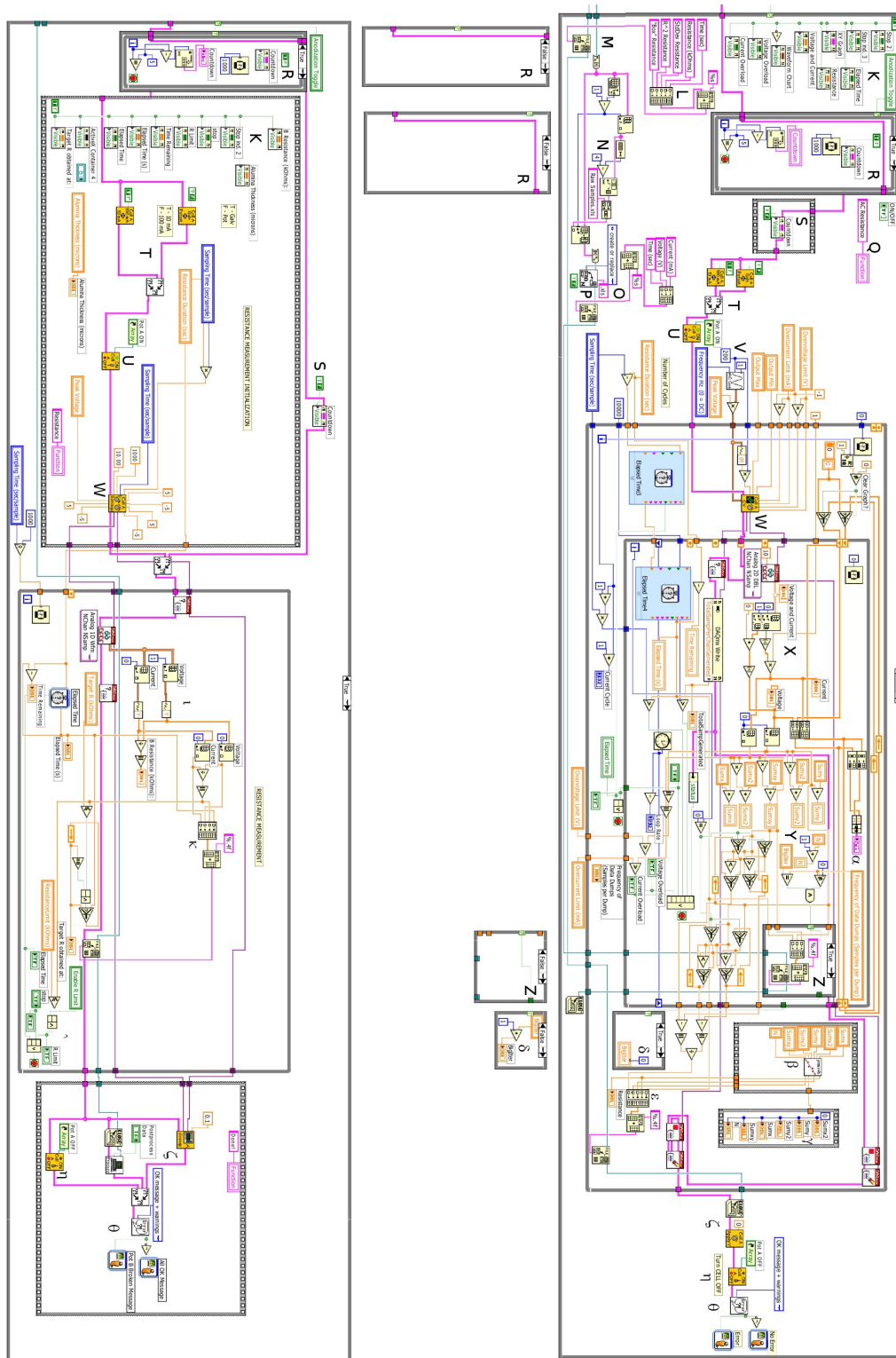
Figure A.11: Code diagram of PStat A - Resistance - 01-25-11.vi; for other potentiostats, the sub-VIs referencing the appropriate device are used.

Figure A.9 begins with the initialization of the interface in section A. This sets a series of visible nodes so that the appropriate inputs and outputs are displayed and the appropriate ones hidden. B is the setup loop, which updates regularly so that switches light the appropriate LED indicators and suchlike. C is the section handling the visiblity of the advanced anodization panel. D handles the generation of the waveform for the output graph based on the Frequency dial.

F is separate to make sure the yes/no anodization toggle is checked after the setup loop has finished cycling - that is, after the Start button is pressed.

G creates the file for the anodization step. H does the same for the resistance file.

Figure A.10 displays the andoization step. It's essentially just the same as the experiment initialization and execution steps of PStat X Constant 01-20-11.vi (A.2.1), so the reader is referred to that section for more detail. The main difference is that the frame I will cause this section only to execute if Anodization Toggle is TRUE. After I, J checks to see if we're doing DC or AC measurement.

Figure A.11 is the heart of the resistance measurement. The top frame is fired if the AC frequency is greater than 0. K Makes the resistance measurement instrument panel visible. L generates the header for the resistance data and passes it to M, which writes the data to the file created in H. N generates a filename based on the name provided in H, appending Raw Samples to the end and creates a new file in the same location of this name. O makes the header for the raw samples file, and P writes it to the file.

Q changes the function header on the output screen to read "AC Resistance." R creates a 5 second countdown delay before starting the resistance measurement, and S makes the countdown indicator invisible after it has reached 0. T then sets the instrument to potentiostatic control and 100 mA current, U turns the potentiostat on, and V generates the waveform of the frequency required using AC Signal Gen.vi (A.2.24).

W is the big iteration loop. W sets up the CV cycle using the input data. X collects the voltage and current data and sends it to the appropriate registers. Y calculates the summed quantities required for a linear regression, using local variables to change the registers without loopbacks. Z will write the current, voltage, and time to the Raw Samples file at a rate determined by the frequency of data dumps input. The current and voltage are monitored at α. Every time the large loop cycles (which is determined by the length of the inner cycle, set by Sampling Time) β will calculate the slope of the V/I curve using Linear Regression.vi (A.2.14). Once this is calculated, γ will reset all of the summed quantities to 0. δ keeps track of the number of big loop iterations have happened since the last time they satisfied the Frequency of Data Dumps condition, and will set them to 0 if a data dump has ocurred. The data calculated in δ is stored in the file created in H at ϵ, and the read and write tasks are stopped, to either be subsequently restarted at W or left stopped at the end of excution of the large loop once the time requested has run out or the stop experiment button is pressed.

At the end of the AC program frame, ζ applies a resting potential of 0, η shuts off the cell,

and θ analyzes the errors and gives feedback.

If the Frequency provided equals 0, the lower frame is fired. R generates the countdown and S will make it invisible when it's done. K sets the appropriate visibility. T sets up the cell and U turns it on. W applies the settings. The data is read in ι and the current, voltage, time, and calculated resistance (V/I) is formatted in κ and sent to the file created in H. The cleanup section is the same as that for AC resistance, save for the fact that the DC data file is processed by Resistance Processing.vi (A.2.13). If Postprocess Data is TRUE, Resistance Processing.vi will do a rolling average of every 5 data points; otherwise it merely puts headers on each column.

A.2.5   PStat X - OCP - 04-13-06.vi

Inputs: None

Outputs:

OCP File: OCP data saved as an .xls spreadsheet in a user-created file.

Dependencies: V-I Data Manipulation.vi (A.2.12)

This program was programmed by Evan Hajime and has been left unmodified. It logs the voltage/current versus time without any application of voltage or current to the potentiostat. During the operation of this program the cell should be OFF at the PStat module, essentially converting the potentiostat into a voltmeter/ammeter.

The code for this program, while not cleaned up or compartmentalized into functions, is the same as that for the OCP collection processes at the beginning of the other large VI's. Thus, I'll not detail it further here.

A.2.6   Cell X Galv-Potent Select.vi

Inputs:

error IN: Error. Optional. Used for event sequencing and error handling.

Boolean: Boolean. Will be used to control Galvanostatic vs. Potentiostatic mode selection. True is Galvanostatic, False is Potentiostatic.
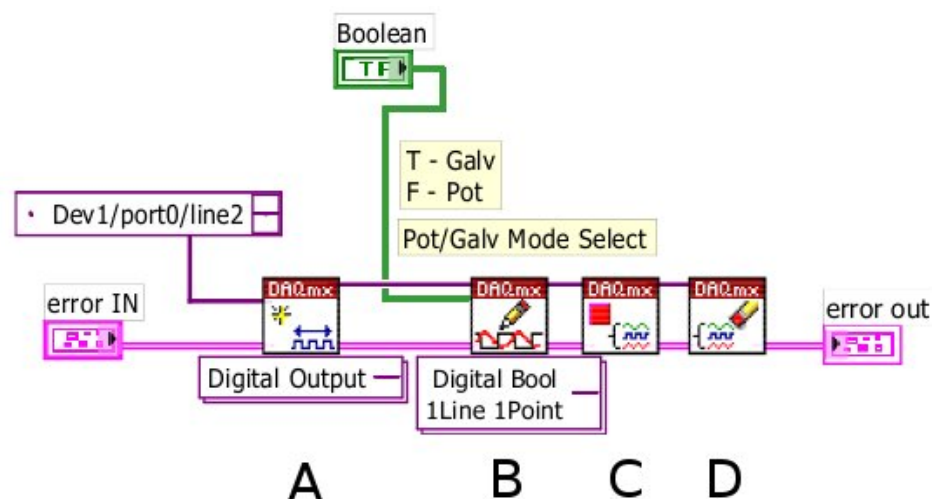
Outputs:

Figure A.12: Code diagram of Cell A Galv-Potent Select.vi; for other potentiostats, the Dev selection is altered.

error OUT: Error. Used for event sequencing and error handling.

Dependencies: None

This sub-VI sets the boolean node addressed port 0, line 2 (Hub Pin #49) on the potentiostat in question, changing the operation of that instrument to galvanostatic or potenitostatic.

In A, the port is addressed. In B, the information is written - TRUE indicates galvanostatic operation, FALSE indicates potentiostatic operation. In C then the write task is halted (we have no need of it once the information is written), and in D the write task is cleared, freeing the resources allocated to it. The error in and out allow for event sequencing and error handling.

A.2.7   Cell X Current Range.vi

Inputs:

error IN: Error. Optional. Used for event sequencing and error handling.

Boolean: Boolean. Will be used to control 10 mA vs 100 mA current range selection. True is 10 mA, False is 100 mA.
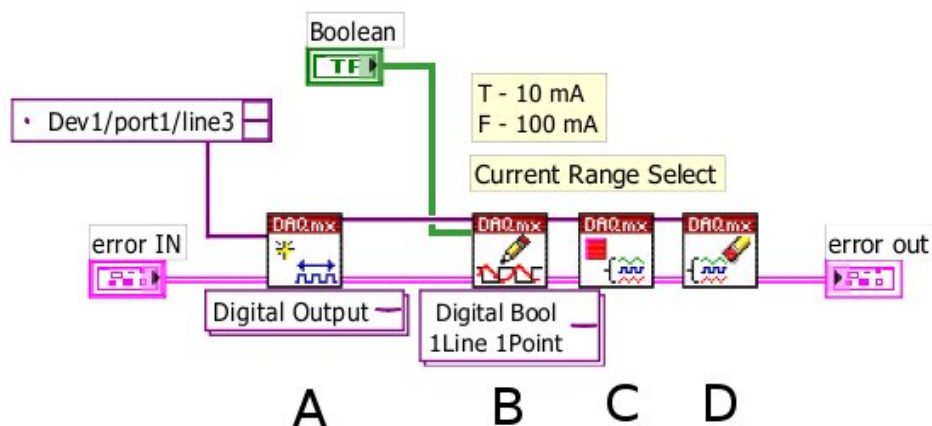
Outputs:

Figure A.13: Code diagram of Cell A Current Range.vi; for other potentiostats, the Dev selection is altered.

error OUT: Error. Used for event sequencing and error handling.

Dependencies: None

This sub-VI sets the boolean node addressed port 1, line 3 (Hub Pin #37) on the potentiostat in question, allowing the instrument to handle higher currents with lower precision or lower currents with higher precision.

In A, the port is addressed. In B, the information is written - TRUE indicates 10 mA operation, FALSE indicates 100mA operation. Note that Cell D has different wiring, and FALSE indcates 1mA operation. In C then the write task is halted (we have no need of it once the information is written), and in D the write task is cleared, freeing the resources allocated to it. The error in and out allow for event sequencing and error handling.

A.2.8   Cell X Settings.vi

Inputs:

error IN: Error. Used for event sequencing and error handling.

Current Max: Double Float. Sets the maximum expected current.

Current Min: Double Float. Sets the minimum expected current.

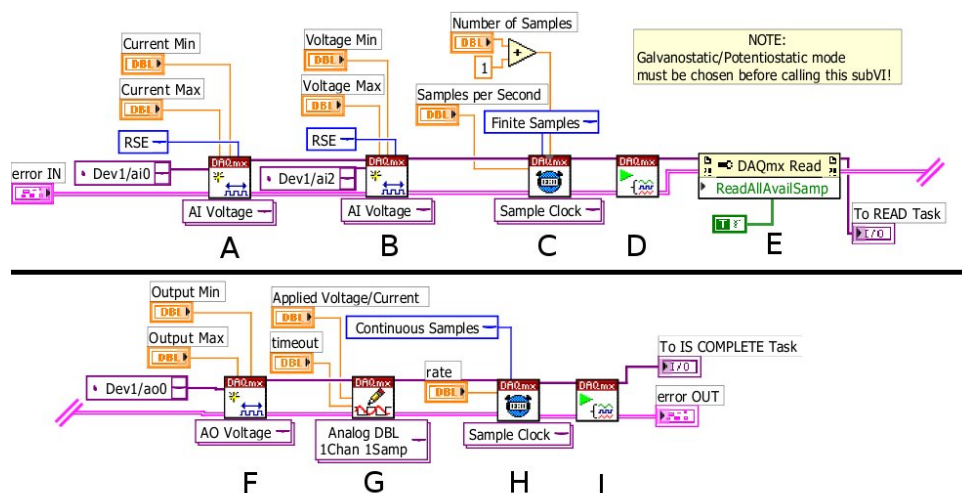*Voltage Max:* Double Float. Sets the maximum expected voltage.

Figure A.14: Code diagram of Cell A Settings.vi; for other potentiostats, the Dev selection is altered.

Voltage Min: Double Float. Sets the minimum expected voltage.

Number of Samples: Double Float. Sets the number of individual current/voltage readings to be collected.

Samples per Second: Double Float. Sets the number of samples collected each second.

Output Max: Double Float. Sets the maximum expected output of the voltage for galvanostatic or current for potentiostaic runs.

Output Min: Double Float. Sets the minimum expected output of the voltage for galvanostatic or current for potentiostaic runs.

Applied Voltage/Current: Double Float. Sets the constant voltage for potentiostatic or current for galvanostatic runs.

timeout: Double Float. 10.00 is a standard value.

rate: Double Float. Determines data rate. 1000 is a standard value.

Outputs:

error OUT: Error. Used for event sequencing and error handling.

to IS COMPLETE Task: Virtual Channel. Sets the applied voltage or current.

to READ Task: Virtual Channel. Regulates data aquisition and timing.
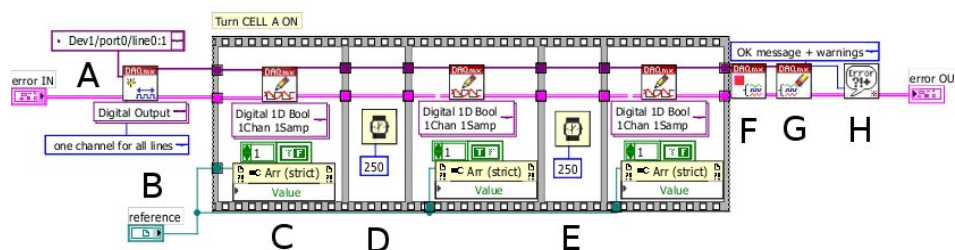
Dependencies: None

Figure A.15: Code diagram of Turn Cell A ON.vi; for other potentiostats, the Dev selection is altered.

This sub-VI interprets user-input parameters into a set of instructions for the potentiostat in question for the Constant program.

A and B create current and voltage read tasks at the appropriate pins (AI0: Hub Pin # 68 - Current Monitor and AI2: Hub Pin #65 - Reference Voltage Monitor). C sets up the sample clock to read a preset number of samples, D starts the task, and E forces it to read all samples out there. The error line continues past the break in the figure.

F sets up the applied current channel addressing AO0 (Hub Pin #22 - Set point), G writes the applied voltage / current to the channel, H sets up a sample clock for continuous samples (so the applied voltage / current is always applied), and finally I starts the task. The error in and out allow for event sequencing and error handling.

A.2.9 Turn Cell X ON.vi

Inputs:

Error IN: Error. Used for event sequencing and error handling.

Reference: Reference to indicator. Indicates boolean on/off value for the cell in question.

Outputs:

error OUT: Error. Used for event sequencing and error handling.

Dependencies: None

This sub-VI turns the appropriate cell on.

Part A creates an output channel addressing port 0, lines 0 to 1 (Hub Pins #52 - Counter

electrode control and #17 - Feedback bypass control). Part C sends "FALSE" to these two pins, opening both controls and thus initializing the instrument. At the same time, reference B is switched as an indicator. Since this write occasionally doesn't take the first time, the frame structure forces the program to wait 250 milliseconds (D), then sets the bits to TRUE, waits another 250 ms, then sets them FALSE again (E). F and G stops the I/O task and clears it (we'll recreate this channel in Turn Cell X OFF.vi). The error in and out allow for event sequencing and error handling, and H will give feedback if one of these operations experienced an error.

A.2.10 Cell X Cleanup+Resting.vi

Inputs:

error IN: Error. Used for event sequencing and error handling.

IS COMPLETE task in: Virtual Channel. Sets the applied voltage or current and sample aquisition.

READ task in: Virtual Channel. Regulates timing of aquisition.

Resting Potential: Double Float. Sets the potential which the potentiostat will acquire and hold until the experiment is turned off.

Outputs:

error OUT: Error. Used for event sequencing and error handling.

Dependencies: None

This sub-VI ends the acquisition tasks and sets a resting potential for the instrument to maintain until the user ends the program. First, the IS COMPLETE task governing sample acquisition is stopped and erased. A new similar task is created, addressing channel AO0 (Hub Pin #22 - Set point), applying the potential specified in Resting Potential, then sopping and erasing the write task. Finally, the READ task governing aquisition is stopped and erased. The error in and out allow for event sequencing and error handling.
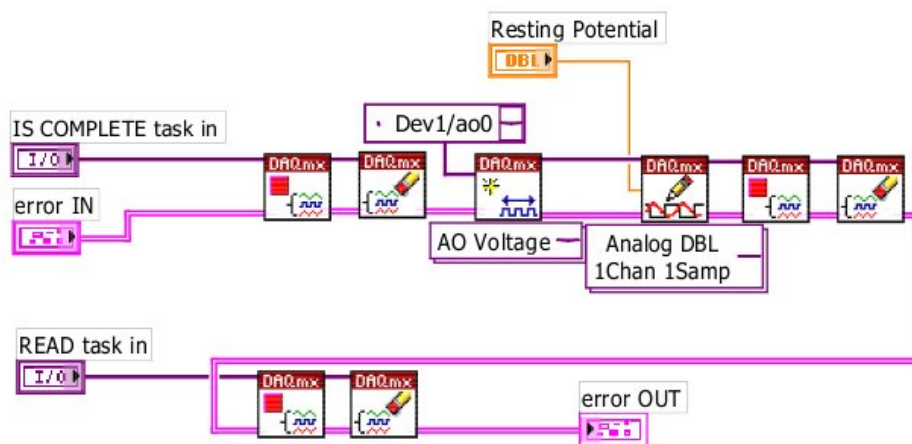
Figure A.16: Code diagram of Cell A Cleanup+Resting.vi; for other potentiostats, the Dev selection is altered.

A.2.11 Turn Cell X OFF.vi

Inputs:

error IN: Error. Used for event sequencing and error handling.

Reference: Reference to indicator. Indicates boolean on/off value for the cell in question.

Outputs:

error OUT: Error. Used for event sequencing and error handling.

Dependencies: None

This sub-VI turns the appropriate cell on.

A, which operates independently of the error sequence, changes the reference from true to false. Part B creates an output channel addressing port 0 lines 0 to 1 (Hub Pins #52 - Counter electrode control and # 17 - Feedback bypass control). Part C sends "TRUE" to these two pins, closing both controls and thus bringing the instrument down. D stops the I/O task and E clears it. The error in and out allow for event sequencing and error handling.
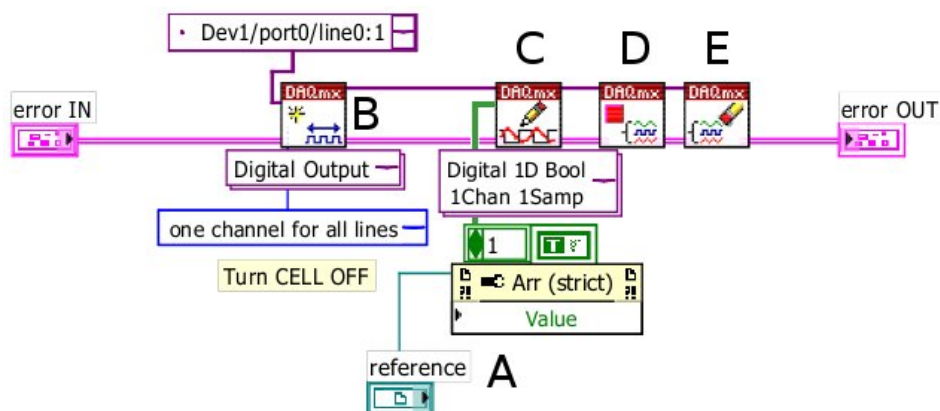
Figure A.17: Code diagram of Turn Cell A OFF.vi; for other potentiostats, the Dev selection is altered.

A.2.12 V-I Data Manipulation.vi

Inputs:

Error in (no error): Error. Used for event seqencing and error handling.

file path: File pointer. This is a file full of raw data to be altered.

Outputs:

error out: Error. Used for event sequencing and error handling.

Dependencies: None

This sub-VI is used to process the raw output from the data acquisition loop into a human-readable table.

A opens the file input. B reads the information from the file. C closes the file again, but the information has been read by the sub-VI and is sent to D, where it is truncated and rotated. The data is then parsed in E and the appropriate components are sent to the loop in F, which corrects the times, making them relative to zero rather than the absolute clock times recorded by the program. G places them back into the vertical format, and H inserts a header as the top line in the file. The file is reopened in I, tagged to automatically replace the previous file. J writes the information in the program to the file, and K finally closes it. The error in and out allow for event sequencing and error handling.

Figure A.18: Code diagram of V-I Data Manipulation.vi

A.2.13 Resistance Processing.vi

Inputs:

Boolean: Boolean. This input determines if the data is postprocessed or just formatted.

path: File Path. This input is the path of the file to be processed.

error IN: Error. Used for event seqencing and error handling.

Outputs:

error OUT: Error. Used for event sequencing and error handling.

Dependencies: None

This sub-VI is used to format the output of the DC resistance measurement in PStat X - Resistance 01-25-11.vi (A.2.4). If Boolean is TRUE, it will also average every 5 data points.

A examines Boolean and activates the appropriate frame. In the top frame, B opens the file specified in path for reading, C reads all of the data from it, and D closes it again. The data is converted to floats in E. I reopens the file for writing, J creates the header for the file, and K writes the header. The opened file is passed to the loop, which starts acting on the data. F will add the first five outputs in each column of the array passed by E, then divide them by 5 in G, convert them into a string in H, and finally write the line to the file in L. The loop will then iterate, so that data points 2, 3, 4, 5, and 6 are averaged and written as the
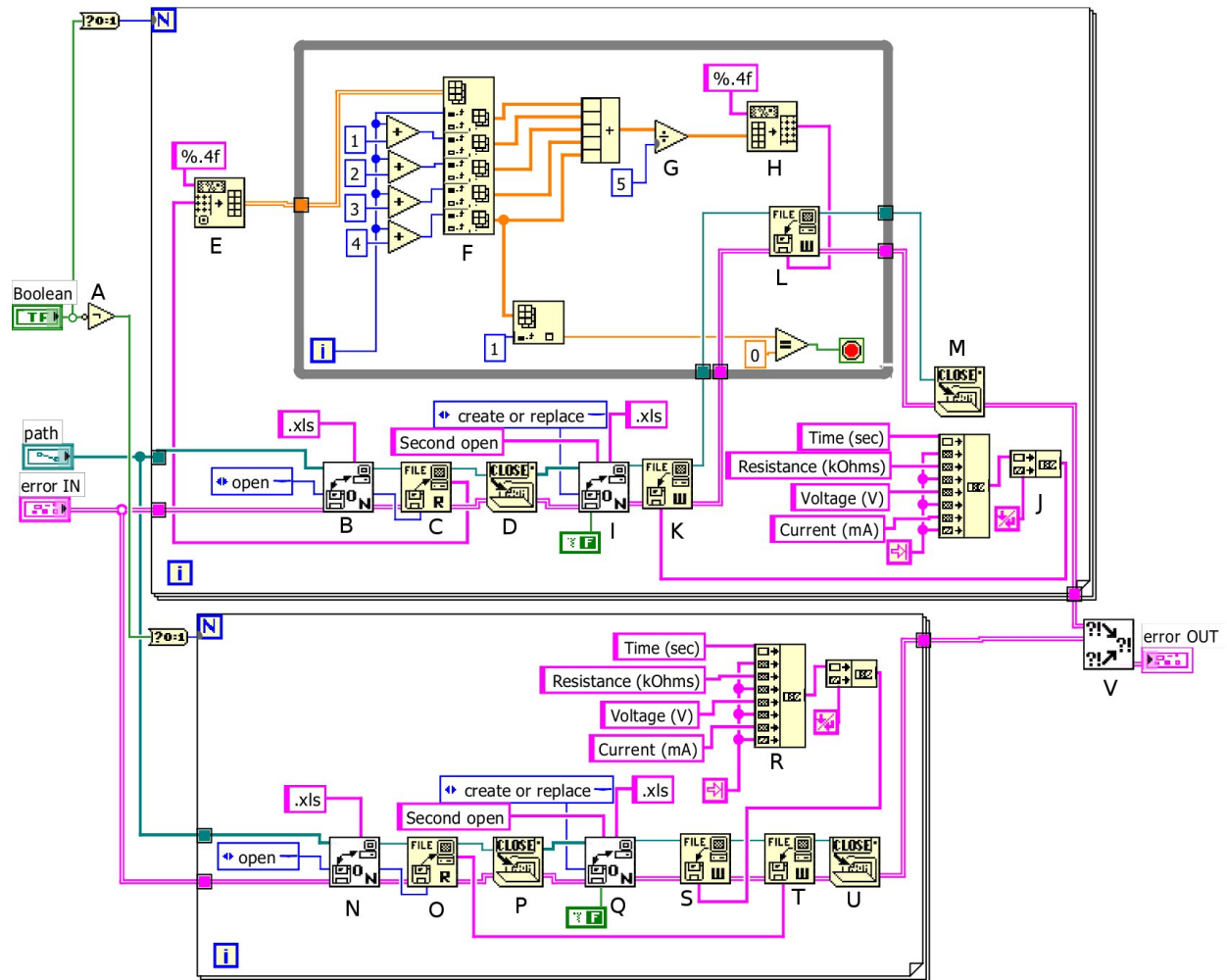
Figure A.19: Code diagram of Resistance Processing.vi

second line. The loop will continue executing until the last file point to be averaged has t = 0, which means it is the end of the data string. M will then close the file.

If Boolean is FALSE, N opens the file for reading, O reads the data, P closes the file, Q reopens the file to be overwritten, R creates the header , S puts the header in the newly open file, T rewrites the data read from the file in O, and U closes the file agian. V condenses the errors and gives the output. The error in and out allow for event sequencing and error handling.

A.2.14   Linear Regression.vi

Inputs:

Sum(X^2): The sum of the squares of every X value in the series.

Sum(X): The sume of every X value in the series.

N: The number of points in the series.

Sum(Y): The sum of every Y value in the series.

Sum(Y^2): The sum of the squares of every Y value in the series.

*Sum(X*Y):* The sum of the product of X and Y for every point in the series.

Outputs:

Slope: The slope of the best fit line, m.

Intercept: The intercept of the best fit line, b.

SD Regression: Standard deviation of the regression, s_y.

SD Slope: Standard deviation in the slope, s_m.

SD Intercept: Standard deviation in the intercept s_b.

R^2: R^2 measurement of fit.

Dependencies: None

This sub-VI calculates the parameters of the linear regression of a series of numbers. Rather
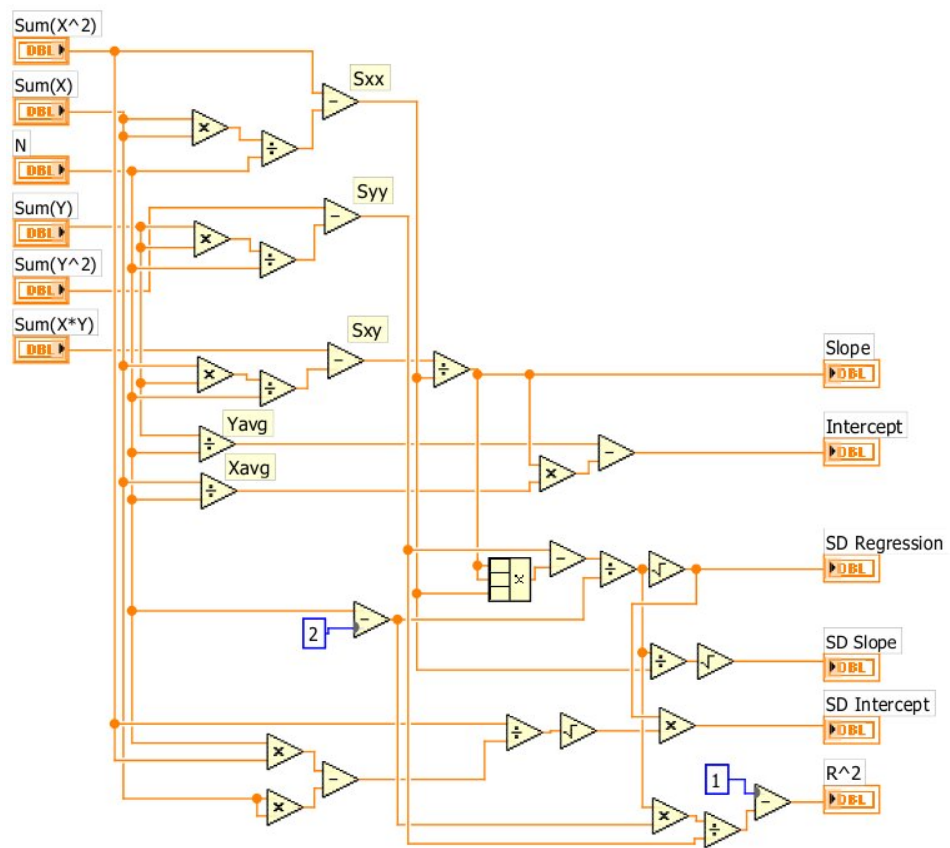
Figure A.20: Code diagram of Linear Regression.vi

than accepting the numbers as inputs it accepts the calculated information from the data series. This allows this sub-VI to calculate regressions on the fly, since in a loop these values can simply be updated with each iteration and passed to the sub-VI again.

The actual operation of the sub-VI uses the method of least squares for the regression. The points in the block diagram where the sub-VI is reflecting certain quantities in the standard least squares notation. The series of equations calculated by the sub-VI is shown below. Intermediate values such as S_{xx} are indicated by labels in the block diagram.

$$S_{xx} = \sum (x_i - \bar{x})^2 = \sum x_i^2 - \frac{(\sum x_i)^2}{N} \tag{A.1}$$

$$S_{yy} = \sum (y_i - \bar{y})^2 = \sum y_i^2 - \frac{(\sum y_i)^2}{N} \tag{A.2}$$

$$S_{xy} = \sum (x_i - \bar{x})(y_i - \bar{y}) = \sum x_i y_i - \frac{(\sum x_i \sum y_i)}{N} \tag{A.3}$$

$$m = \frac{S_{xy}}{S_{xx}} \tag{A.4}$$

$$b = \hat{y} - m\hat{x} \tag{A.5}$$

$$s_y = \sqrt{\frac{S_{yy} - m^2 S_{xx}}{N - 2}} \tag{A.6}$$

$$s_m = \frac{s_y}{\sqrt{S_{xx}}} \tag{A.7}$$

$$s_b = s_y \sqrt{\frac{\sum x_i^2}{N \sum x_i^2 - (\sum x_i)^2}} = s_y \sqrt{\frac{1}{N - (\sum x_i)^2 / \sum x_i^2}} \tag{A.8}$$

$$R^2 = 1 - \frac{\sum y_i^2 + \sum x_i^2 - 2 \sum x_i y_i}{S_{yy}} \tag{A.9}$$

The sub-VI then returns the appropriate calculated quantities.

A.2.15   CV Cycle Generation.vi

Inputs:

Current Range (1/10mA, 10/100mA): Double Float. For 10 mA current range, this should be 1, for 100 mA current range, this should be 10.

Vi (V): Double Float. The voltage (or current, for a galvanic CV) at which the CV cycle will start.

Vlambda (V): Double Float. The voltage (or current, for a galvanic CV) at which the cycle should turn around and begin tracking back to Vi.

Galv Curr Offset (mA): Double Float. The current offset for the instrument in question.

Pot Volt Offset (V): Double Float. The voltage offset for the instrument in question.

Pot(F)/Galv(T): Boolean. Selection for potentiostatic or galvanostatic mode - cyclic voltammetry should be carried out in potentiostatic mode, but this allows for cycling current if someone wants to for some reason.

Step Size, D V (mV): Unsigned Long. The size in mV of the steps between points in the waveform to be generated.

Scan Rate (mV/sec): Unsigned Long. The rate at which the voltage should be changed in the waveform to be generated.

Outputs:

Output Waveform: Waveform. This is the CV waveform to be passed to the instrument channel.

Array Size: Integer. This is the number of points in the waveform created.

Waveform Graph: Double Float Array. This is a 1D array of the voltage points generated.

Output Array: Double Float Array. This is identical to Waveform Graph. I don't know what this is doing here.

Dependencies: None

This sub VI was created by Evan Hajime, and has been modified by me only to clean up and condense the wiring so it is easier to see the function it performs.
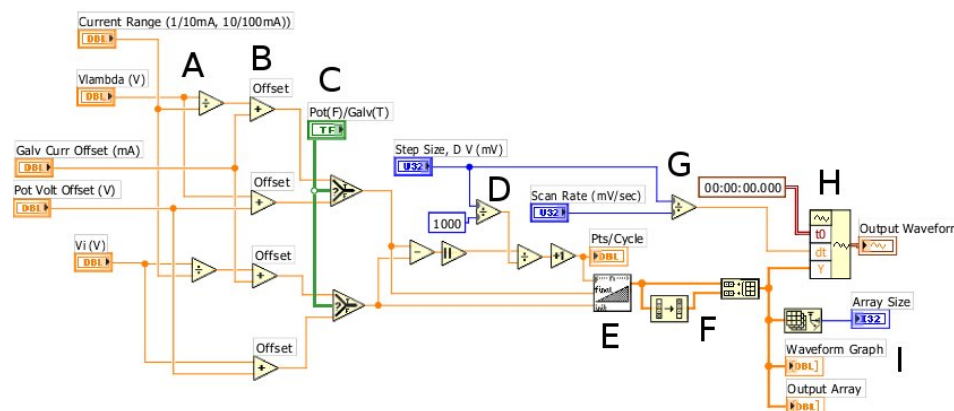
Figure A.21: Code diagram of CV Cycle Generation 5.vi

A corrects for current range alteration, B applies the appropriate offset, and C selects the correct value to use for potentiostatic or galvanostatic operation for both V_i and V_λ. D uses the step size requested to calculate the number of steps between the two chosen numbers. This gets passed to a stock sub-VI which creates an array of a requested number of evenly spaced points between two values. This array is copied, inverted, and tacked on the end of an unaltered array in F to create the cycle. In G, the scan rate and step size are used to figure out how much time should pass between each point, and both this and the voltage points are passed to a waveform creation VI in H, which makes a two column time vs. voltage plot and outputs it as a waveform. I outputs the voltage point array and the number of points in the array.

A.2.16   CV Data Manipulation 2.vi

Inputs:

file path: The file path specifying the file to be manipulated.

error IN: Error. Optional. Used for event sequencing and error handling.

default name: The default name of the file to be saved.

# of Cycles: The number of cycles in the cyclic voltammogram.

Array Size: The number of points in one cycle of the CV.

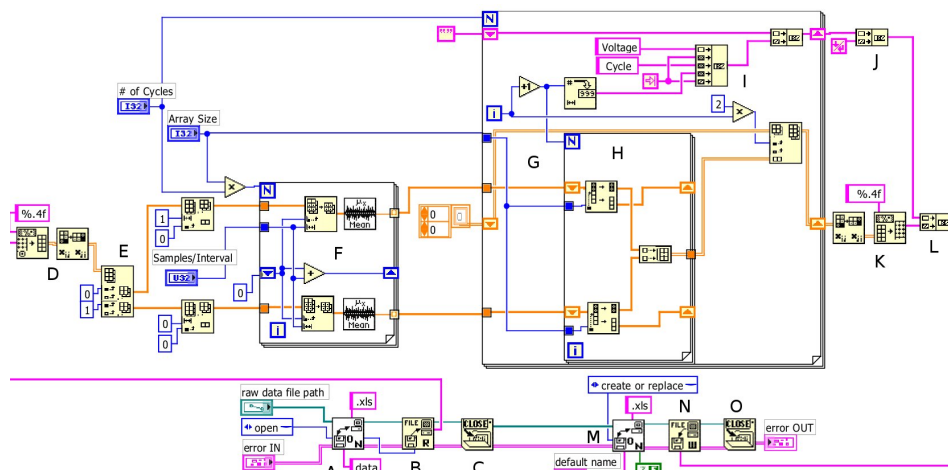*Samples/Interval:* The number of samples collected per second during the CV.

Figure A.22: Code diagram of CV Data Manipulation 2.vi.

Outputs:

error OUT: Error. Used for event sequencing and error handling.

Dependencies: None

This sub-VI was originally programmed by Evan Hajime - I have only cleaned up its flow slightly. It formats raw CV data into a multi-column tab deliminated spreadsheet.

A opens the file specified by the path for reading. B reads al of the data in the file, and C closes it again. The data is passed to D, which converts it from a string into a double float, then inverts it. At this point the data is an array consisting of one long string of voltage and one of current current.

E E separates the voltage and the current strings. F loops through every data point (the number = # of Cycles * Array Size) and averages the the range of samples specified in Samples / Interval, creating new averaged arrays of the same size for both current and voltage. G loops once for each cycle. Within G, H loops a number of times determined by the cycle being examined. Each time it loops, it cuts out one cycle's worth of points on both the current and voltage arrays. The last one written will be the points corresponding the the cycle in question. These two strings are also put together into a joint array, which is then passed on, where it it put into a larger array made up of vertically the double row arrays created by H. For each cycle of G, I creates a Voltage [tab] Cycle # [tab] heading and appends it to itself, so there will be a string of such headings, one for each cycle. J inserts a line feed at the end of the heading string, and K inverts the series of rows created by G into a series of columns, then converts back from double floats to strings. L puts the header on top of the array of strings. Meanwhile, M has opened the file again, this time for writing, and allows it to replace the previously created one. N writes to this file the data from L, and O closes the file again. The error in and out allow for event sequencing and error handling.
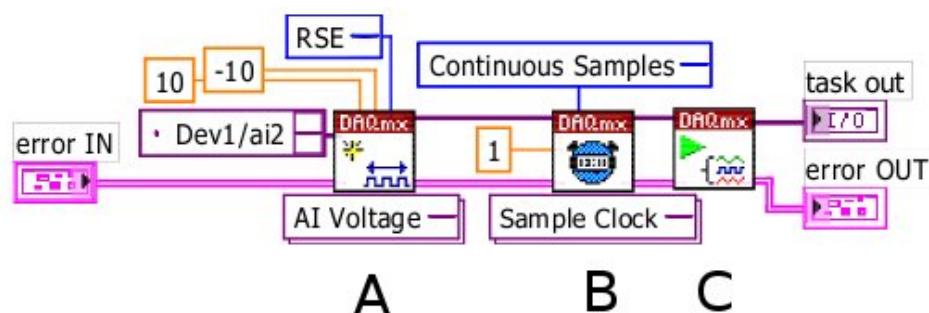
Figure A.23: Code diagram of Cell A OCP Setup.vi; for other potentiostats, the Dev selection is altered.

A.2.17   Cell X OCP Setup.vi

Inputs:

error IN: Error. Optional. Used for event sequencing and error handling.

Outputs:

error OUT: Error. Used for event sequencing and error handling.

task out: Task. This is the task created by the sub-VI.

Dependencies: None

This sub-VI is used to create the OCP data collection task. A creates the task, addressing AI2 (Hub Pin #65 - Reference Voltage Monitor). B sets it up to keep running continuously, collecting every second, and C starts the task. The error in and out allow for event sequencing and error handling.

A.2.18   Cell X Apply Potential.vi

Inputs:

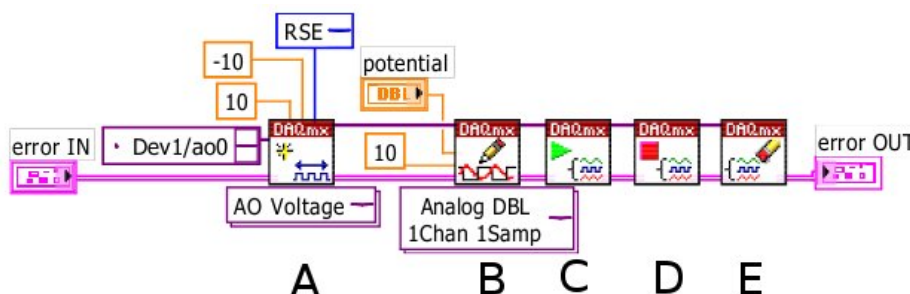*error IN:* Error. Optional. Used for event sequencing and error handling.

Figure A.24: Code diagram of Cell A Apply Potential.vi; for other potentiostats, the Dev selection is altered.

potential: Float. This is the potential to be applied.

Outputs:

error OUT: Error. Used for event sequencing and error handling.

Dependencies: None

This sub-VI is a self-encapsulated way to apply a continuous potential to the working electrode.

A addresses AO0 (Hub Pin #22 - Set point). B writes the potential to be applied to that pin, C executes the write task, D ends the write task (after it's been written), and E clears the task. The error in and out allow for event sequencing and error handling.

A.2.19   Cell X CV-ED Counter.vi

Inputs: None

Outputs:

error OUT: Error. Used for event sequencing and error handling.

Dependencies: None

This sub-VI is used to start a continuous clock running to be used for timing by Cell X CVED Setup.vi (A.2.21).

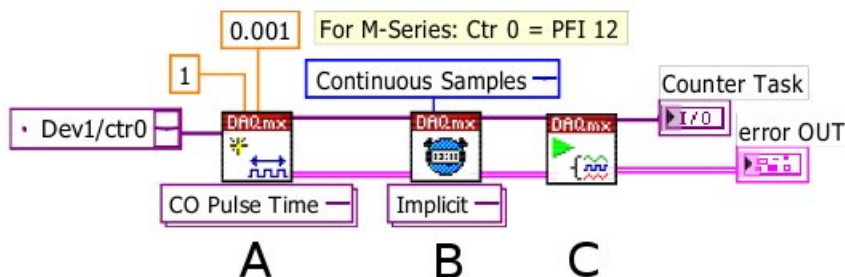A creates a pulse time virtual channel, referencing ctr 0 (PFI 12). B sets the timing to run

Figure A.25: Code diagram of Cell A CV-ED Counter.vi; for other potentiostats, the Dev selection is altered.

continuously, and C starts the task. The task is stopped in the cleanup phase of Cell X CV-ED 01-20-11.vi. The error out allows for event sequencing and error handling, specifically making sure that the channel is not stopped until it should be.

A.2.20   OCP Data Manipulation.vi

Inputs:

file path: The file path specifying the file to be manipulated.

error IN: Error. Optional. Used for event sequencing and error handling.

Outputs:

error OUT: Error. Used for event sequencing and error handling.

Dependencies: None

This sub-VI is used to change the data in an OCP collection file into a properly formatted .xls spreadsheet with column headers.

A opens the file specified by the file path for reading, B reads all of the data from it, and C closes it again. D changes the data from strings into numbers and transposes the data, E selects the row of time data and sends the first data point and the full array of time data to a loop (F) which subtracts the first point from each subsequent point, so that the time recorded is relative to the start of the program. G replaces the old time row in the original data with that produced by F and H transposes the data back into column form and re-converts it into strings. I generates the titles for the two columns, and J places these titles
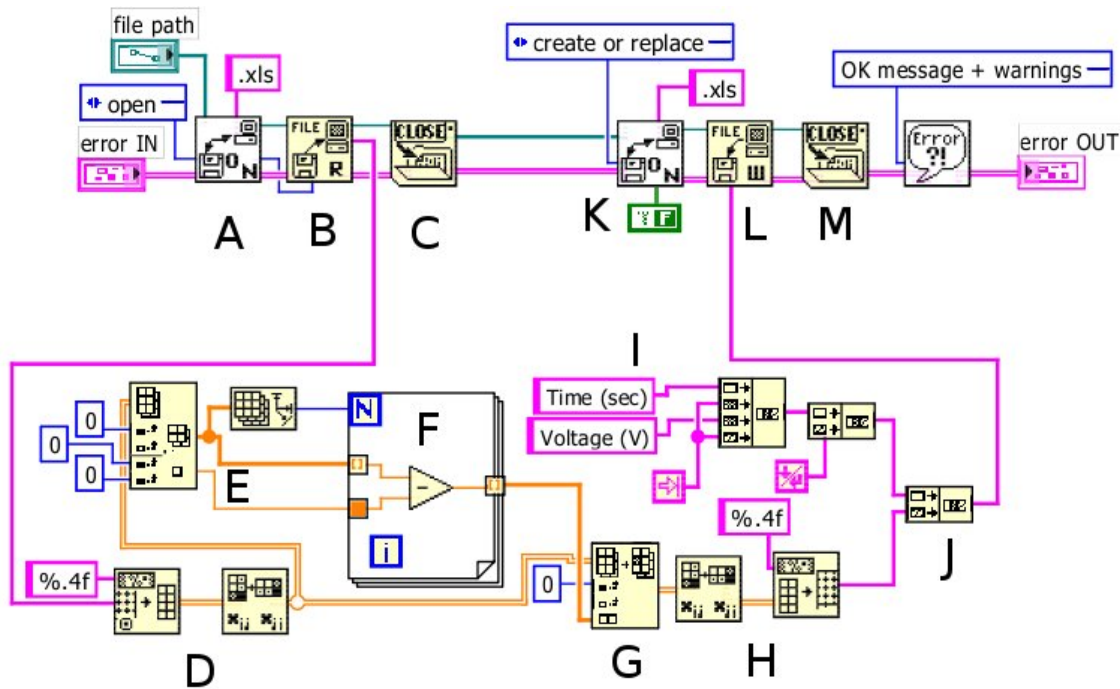
Figure A.26: Code diagram of OCP Data Manipulation.vi

as the top of the text data set. Meanwhile, K has re-opened the closed file for overwriting. L overwrites the file with the newly created data, and finally M closes the file again. The error in and out allow for event sequencing and error handling.

A.2.21 Cell X CVED Setup.vi

Inputs:

error IN: Error. Used for event sequencing and error handling.

Current Max: Double Float. Sets the maximum expected current.

Current Min: Double Float. Sets the minimum expected current.

Voltage Max: Double Float. Sets the maximum expected voltage.

Voltage Min: Double Float. Sets the minimum expected voltage.

Samples/Interval: Unsigned Long. Sets the number of samples to be collected per second.
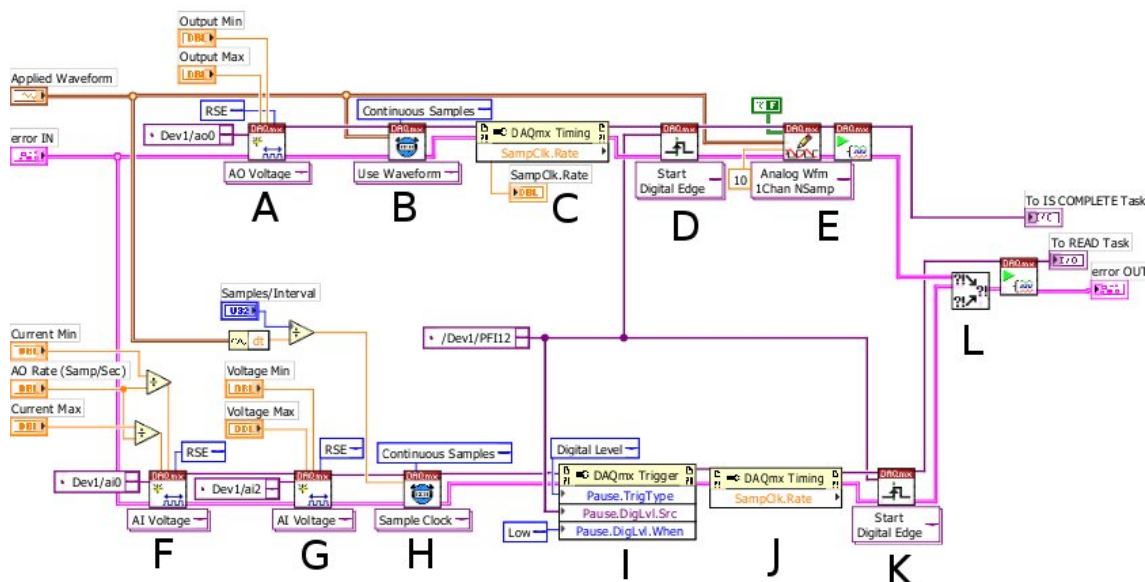
Figure A.27: Code diagram of Cell A CVED Setup.vi; for other potentiostats, the Dev selection is altered.

Output Max: Double Float. Sets the maximum expected output of the voltage for galvanostatic or current for potentiostaic runs.

Output Min: Double Float. Sets the minimum expected output of the voltage for galvanostatic or current for potentiostaic runs.

Applied Waveform: Waveform (signal vs. time). Sets the waveform which will be repeated during the electrodeposition.

AO Rate (Samp/Sec): Double Float. Sample rate for the acquisition task.

Outputs:

error OUT: Error. Used for event sequencing and error handling.

to IS COMPLETE Task: Virtual Channel. Sets the applied voltage or current.

to READ Task: Virtual Channel. Regulates data aquisition and timing.

Samp Clk. Rate: Double Float. Shows the sampling rate for the applied potential / current task.

Dependencies: None

This sub-VI sets up the virtual channels requied for waveform applicaton for electrodeposition.

A creates a channel referencing AO0 (Hub Pin #22 - Set point), B sets up a timing task using the timing from the waveform supplied, C gives feedback as to the sample rate, D sets the timing to be regulated by PFI12, which should have been started previously, using Cell X CV-ED Counter.vi (A.2.19). E writes the waveform to the channel, and E starts the task.

F and G create channels referencing AI0 (Hub Pin # 68 - Current Monitor) and AI2 (Hub Pin #65 - Reference Voltage Monitor). H sets up a timing task to run continuously using timing specified by the samples per interval. I sets the acquisition to respond to the digital pulse on PFI12 created by Cell X CV-ED Counter.vi (A.2.19) so the high/low rate acquisition works. J is unused, but serves the same purpose in this task as C. K sets the timing to be regulated yb PFI12. L condenses the errors into one output and finally starts the sample acquisition task, so that an error in the voltage application task will prevent starting the acquisition task.

A.2.22   Cell X CV Cycle Setup.vi

Inputs:

error IN: Error. Used for event sequencing and error handling.

Current Max: Double Float. Sets the maximum expected current.

Current Min: Double Float. Sets the minimum expected current.

Voltage Max: Double Float. Sets the maximum expected voltage.

Voltage Min: Double Float. Sets the minimum expected voltage.

Samples/Interval: Unsigned Long. Sets the number of samples to be collected per second.

AO Max: Double Float. Sets the maximum expected output of the voltage for galvanostatic or current for potentiostaic runs.

AO Min: Double Float. Sets the minimum expected output of the voltage for galvanostatic or current for potentiostaic runs.

Applied Waveform: Waveform (signal vs. time). Sets the waveform which will be applied for the CV.

Outputs:

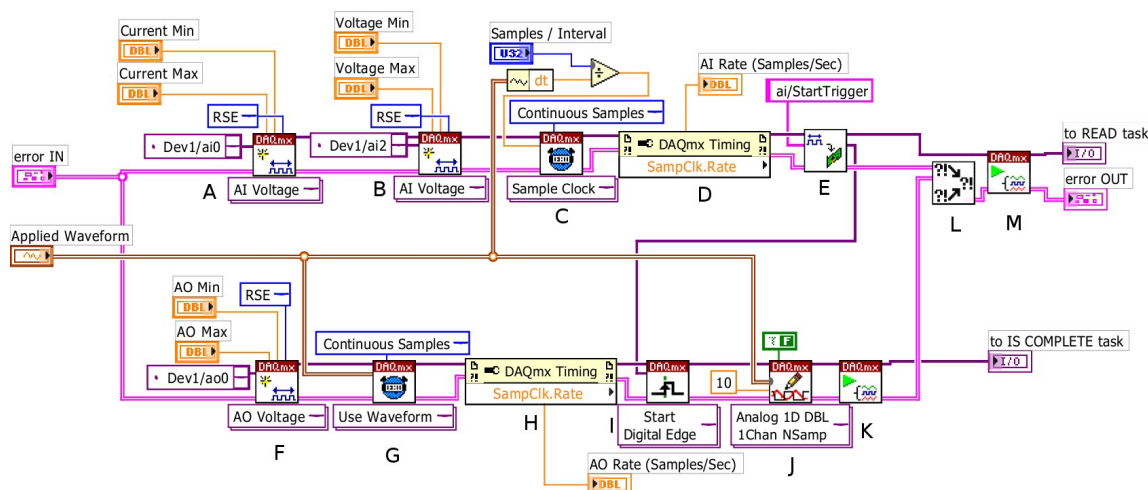*error OUT:* Error. Used for event sequencing and error handling.

Figure A.28: Code diagram of Cell A CV Cycle Setup.vi; for other potentiostats, the Dev selection is altered.

to IS COMPLETE Task: Virtual Channel. Sets the applied voltage or current.

to READ Task: Virtual Channel. Regulates data aquisition and timing.

AI Rate (Samples/Sec): Double Float. Sample rate for the read task.

AO Rate (Samples/Sec): Double Float. Sample rate for the voltage application task.

Dependencies: Get Terminal Name with Device Prefix.vi (A.2.23)

This sub-VI sets up the instrument for each CV cycle.

A and B create channels referencing AI0 (Hub Pin # 68 - Current Monitor) and AI2 (Hub Pin #65 - Reference Voltage Monitor). C sets up a timing task to run continuously using timing specified by the samples per interval. D reads the sample rate and outputs it. E is a call to Get Terminal Name with Device Prefix.vi (A.2.23) to do exactly what it says on the tin.

F creates a channel referencing AO0 (Hub Pin #22 - Set point), G sets up a timing task using the timing from the waveform supplied, H gives feedback as to the sample rate, I sets the timing to be regulated by the terminal from the first series supplied by E. J writes the waveform to the channel, and K starts the task. L gathers the errors and makes sure that the voltage application task has started before starting the acquisition task with K.
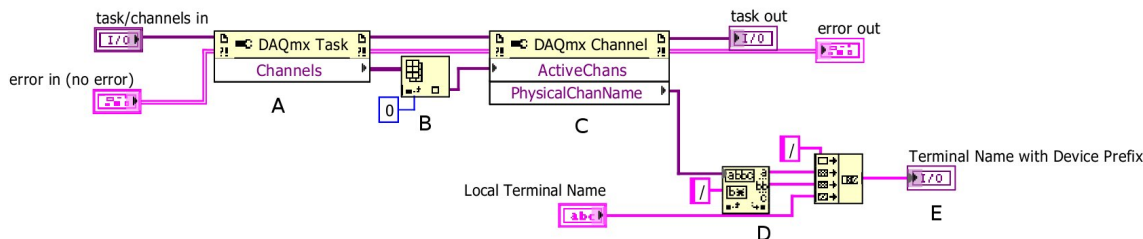
Figure A.29: Code diagram of Get Terminal Name with Device Prefix.vi

A.2.23 Get Terminal Name with Device Prefix.vi

Inputs:

error in (no error): Error. Used for event sequencing and error handling.

task/channels in: Virtual Channel. This is the channel from which we want to get the terminal name.

Local Terminal Name: String. The name of the terminal we want e.g. "ai/StartTrigger".

Outputs:

error out: Error. Used for event sequencing and error handling.

task out: Virtual Channel. The first task we sent in leaves here.

Terminal Name with Device Prefix: Virtual Channel. What we're trying to get.

Dependencies: None.

This sub-VI was orignially programmed by Evan Hajime and has been left unchanged. It is used to get a physical channel from the data acquisition channels to serve as the timing regulator for the voltage application in Cell X CV Cycle Setup.vi A.2.22

A opens up the virtual channel into a bundle of physical channels. B selects the first of these channels. C gets the name of that channel and passes it to D, which converts it to a string, puts slashes around i, and appends the Local Terminal Name supplied. This is then output as a Virtual Channel.

A.2.24   AC Signal Gen.vi

Inputs:

frequency: Double Float. The frequency in hz of the waveform to be created. If 0 is sent, the function will output a flat graph.

points: Unsigned Long. The number of points per wave for the output waveform.

Amplitude: Double Float. The amplitude of the final waveform.

Outputs:

Waveform Graph: Value Versus Time Array. The output waveform.

Dependencies: None

A fires if the frequency input is not equal to 0, so we want to generate a waveform. Waves by default is 1 (this can be changed inside the funciton if needed.) The math displayed in the TRUE selection boils down to creating a series of points (of a number equal to points*frequency + 1). Each point has a value equal to Amplitude*sin((point number/number of points)*2π), calculated in loop B. C puts these in a vs. T matrix, making a waveform one second long.

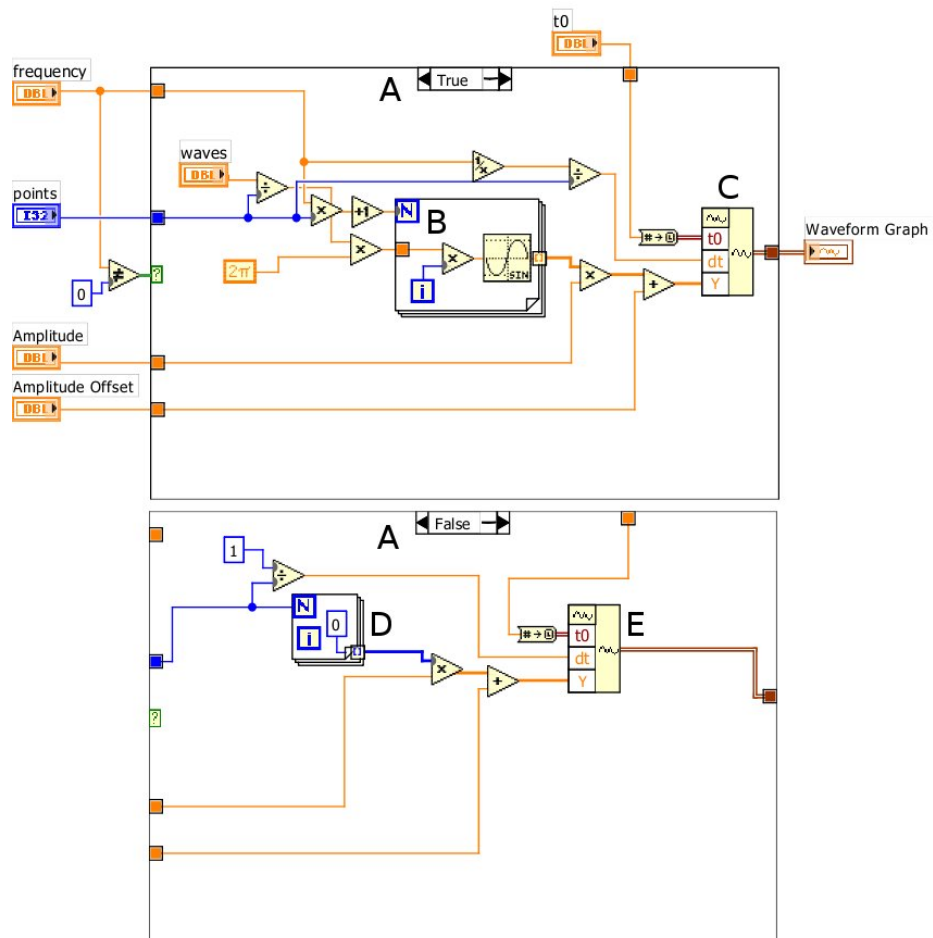If A is FALSE, we generate a flat waveform. D creates a number of points equal to points, sets them equal to zero, and creates a one second line.

Figure A.30: Code diagram of AC Signal Gen.vi